RMIT UNIVERSITY

Thermal-mechanical response modelling and thermal damage prediction of soft tissues during thermal ablation

A thesis submitted in fulfilment of the requirements for the degree of Doctor of Philosophy

Xin Li

MEng (Hefei University of Technology)

School of Engineering

College of Science, Engineering and Health

RMIT University

02/10/2017

Acknowledgements

Firstly, I would like to thank my senior supervisor Associate Professor Yongmin Zhong and second supervisor Professor Reza Nakhaie Jazar from RMIT University for their guidance, support and advice during my candidate. I have learned a great amount of research methods and skills from them that I would like to practice in my future work.

Secondly, I acknowledge the support I have received for my research through the provision of an Australian Government Research Program Scholarship.

Last but not the least, I give my great thanks to my parents for their support during my study years, and the infinite love and affection from my husband and my lovely daughter.

Declaration

I certify that except where due acknowledgement has been made, the work is that of the author alone; the work has not been submitted previously, in whole or in part, to qualify for any other academic award; the content of the thesis is the result of work which has been carried out since the official commencement date of the approved research program; any editorial work, paid or unpaid, carried out by a third party is acknowledged; and, ethics procedures and guidelines have been followed.

Xin Li

02/10/2017

Publications

1) X. Li, Y. Zhong, R. Jazar, and A. Subic, "Thermal-mechanical deformation modelling of soft tissues for thermal ablation," *Bio-medical materials and engineering,* vol. 24, pp. 2299-2310, 2014.

2) X. Li, Y. Zhong, A. Subic, R. Jazar, J. Smith, and C. Gu, "Prediction of tissue thermal damage," *Technology and Health Care,* vol. 24, pp. S625-S629, 2016.

3) X. Li, Y. Zhong, J. Smith, and C. Gu, "Non-Fourier based thermal-mechanical tissue damage prediction for thermal ablation," *Bioengineered,* vol. 8, pp. 71-77, 2017.

4) X. Li, Y. Zhong, and C. Gu, "Heating analysis of soft tissue at finite deformation during thermal ablation," Journal of Mechanics in Medicine and Biology, Accepted, 2017.

Table of Contents

Table of Figures

Table of Tables

Table of Equations

Nomenclature

Ω Thermal damage

q Heat flow rate

A Frequency factor

ΔE Activation energy

R Universal gas constant

C Concentration of molecules

N Crosslink density

K Boltzmann constant

T Temperature at time t, also denoted as θ

E Lagrangian strain tensor

S Second Piola-Kirchhoff stress tensor

ψ Helmholtz free energy per unit mass

u Specific internal energy per unit mass

η Specific entropy

F Material deformation gradient

$\mathbf{F}_e$ Elastic deformation gradient

$\mathbf{F}_\theta$ Thermal deformation gradient

ς Stretch ratio

Ψ_e Strain energy per unit volume

λ , μ Lame parameters

$\boldsymbol{\varepsilon}$ Infinitesimal strain

$\boldsymbol{\sigma}$ Cauchy stress

E Young's modulus

ν Poisson's ratio

α Linear coefficient of thermal expansion

k Bulk modulus

δ_{ij} Kronecker's symbol

$\boldsymbol{u}$ Displacement vector

Q_{ext} External heating source

Q_{met} Metabolic heat generation

Q_{blo} Blood perfusion

ρ Density

C Specific heat

C_b Specific heat of blood

ω_b Blood perfusion

ρ_b Density of blood

T_b Temperature of blood vessel

$\boldsymbol{b}$ Specific body force

$\boldsymbol{F}_{int}$ Internal force

$\boldsymbol{F}_{ext}$ External force

$\boldsymbol{M}$ Global mass matrix

$\boldsymbol{C}$ Global damping matrix

ζ Damping coefficient

$\underline{\boldsymbol{u}}$ Combined temperature and displacement vector

$\boldsymbol{K}$ Stiffness matrix

Δt Time step

$\Delta \boldsymbol{G}_{TS-N}$ Energy barrier between native and transition state

$\Delta \boldsymbol{G}_{TS-D}$ Energy barrier between denatured and transition state

E_T Thermally induced strain energy

$\acute{E}_{TM}$ Thermally and mechanically induced strain energy

V_{mol} Molar volume

τ_p Characteristic time

N_l Shape function

$N_,$ Weighting factor

$\boldsymbol{\epsilon}$ Green-Lagrange strain vector

$\boldsymbol{s}$ Second Piola-Kirchhoff stress vector

$\mathbf{C}$ Right Cauchy–Green tensor

$\boldsymbol{B}$ Strain displacement matrix

$\boldsymbol{D}$ Material stiffness matrix

Ψ_e^{fiber} Stored energy of collagen fibre bundles

R' Symmetry group of a material

$\mathbf{Q}$ Orthogonal transformation

$\boldsymbol{l}_i$ Selected fibre bundle direction

$\mathbf{L}_i$ Structural tensor of $\boldsymbol{l}_i$

$\boldsymbol{a}_{0i}$ Preferred fibre bundle direction in the reference configuration

k_1, k_2 Positive material constants

Abstract

During thermal ablation, target soft tissue responses both thermally and mechanically simultaneously. However, current thermal ablation treatment mainly relies on the quantitative temperature indication to evaluate tissue behaviours and control the delivered thermal energy, which is ineffective and inaccurate. Based on these, our research study focuses on: bioheat transfer theory, linear and nonlinear elasticity of soft tissues at varied temperatures, as well as thermal damage prediction theory, and the whole program was developed in Netbeans IDE 8.1. The main contributions of our research work lie in the following aspects:

Firstly, considering a situation where soft tissue's mechanical deformation during thermal ablation is only caused by thermal loading, it is reasonable to assume that the generated strain value is within the linear range of stress-strain relationship characterisation which is also thermal stable (nearly temperature independent). Therefore, we propose our first model by integrating the heating process with thermally-induced mechanical deformations of soft tissues for simulation and analysis of the thermal ablation process. This method combines classical Fourier based bioheat transfer and constitutive elastic mechanics derived from the method of multiplicative decomposition of thermal mechanical deformation gradient, as well as non-rigid motion dynamics. The 3D governing equations are discretised spatially using finite difference scheme and temporally using implicit time integration scheme and the obtained linear system of equations are subsequently solved using a Gauss-Seidel iterative solver. Simulation implement based on proposed method can serve as a visible assistance for relevant surgeons on analysing soft tissue's behaviours from both

thermal and mechanical deformation fields rather than from just determined temperature distribution.

Secondly, we present a method to characterize soft tissue thermal damage by taking into account of thermal mechanical interactions during thermal ablation, concerning stored energy by both thermal and mechanical effects can affect the energy barrier for macromolecular transitions, leading to further or the reverse damage to treated biological tissues. To do this, traditional tissue damage model of Arrhenius integration is improved by including the thermally and mechanically induced strain energy term. Simulations and comparison analysis based on different types of soft tissues are also performed to study its influences. Our findings may provide more reliable guidelines for relevant surgeons to control the tissue damage zone during thermal ablation practice.

Thirdly, thermal relaxation time used to describe heating process in homogeneous substance is usually referred to as the characteristic time in non-homogeneous biological materials, which is needed to accumulate enough energy to transfer to the nearest point. Such non-Fourier thermal behaviour has also been experimentally observed in biological tissues. Our second model is presented by integrating non-Fourier bioheat transfer and constitutive elastic mechanics derived from the method of multiplicative decomposition of thermal mechanical deformation gradient, as well as non-rigid motion of dynamics to predict and analyse thermal distribution, thermal-induced mechanical deformation and tissue damage under purely thermal loads. The simulation performances are compared between two numerical methods: Finite Difference Method and Finite Element Method, from perspectives of accuracy and

computing efficiency, and also against available existed experimental data and other commercialized analysis tools.

Finally, our research moves on to nonlinear range characterization of tissue deformation under combined thermal and mechanical loads. Basically, the contribution of our proposed nonlinear thermal mechanical model is by extending the finite strain framework of Neo-Hookean energy function to the heating process of soft tissues during thermal ablation. Meanwhile, our nonlinear thermal mechanical model also considers the effect of collagen fibre bundles as embedded in many biological tissues. Separating free energy density modelling into isotropic and anisotropic parts, it is assumed that the anisotropy is due to the collagen fibre bundles behaviour, while the ground substance, behaves in an isotropic manner can be modelled using selected nonlinear biomaterial model. The necessary ingredients for the finite element method implementation including: weak form and time integration are also included in this chapter.

Keywords: Thermal ablation, soft tissue, non-Fourier bioheat transfer, thermal mechanical deformation, anisotropic nonlinear, tissue damage.

1   Introduction

As energy based medical practice for treating cancerous tissues, thermal ablation technology offers several advantages over traditional surgical resections, such as lower morbidity, shorter hospitalization times and the ability to treat poor surgical candidates. The understanding of soft tissues' responses during thermal ablation process is important for better pre-operation treatment planning purpose. To analyse such responses, we have to study the heat transfer pattern within biological tissues as well as corresponding tissue deformations.

In terms of tissue deformations, the choosing of proper stress-strain relationship for analysis of soft tissue properties under thermal and mechanical loads depends on resultant strain range [1-3]. In reality, subject to purely thermal loads during thermal ablation, for example, using a needle like heating device to treat cancerous tissues inside human organs, thermal induced strain level is usually within the linear regime characterization of stress-strain relationship. Therefore, linear thermoelasticity would be a proper selection for analysing thermal mechanical interactions during such a process. However, only few related studies can be found in this field and they were mainly focused on the research of skin burns. Among these studies, Xu et al. treated the human skin as a kind of composite material, laminate, where heat-induced mechanical response (thermal stress) was calculated based on related theories [3-5]. Shen et al. reported a numerical model to predict the linear thermoelastic deformation of skin tissue at high temperature [6, 7]. Lozano et al. analyzed the radio frequency heating of cutaneous and subcutaneous tissues, including their linear thermoelastic response [8]. However, these methods are either based on commercialized analysis tools [3-5] [8] or

lack accounting for irregular tissue geometry and time domain analysis [6, 7], which are practically not suitable for real life thermal ablation simulation purpose. Furthermore, in most of these models, the damage prediction part is always ignored [3-5, 8] or not distinguished very well due to thermal variation or external mechanical stimuli [7]. However, in our research, both purely thermal, and combined thermal and mechanical loadings are introduced.

The difference of our research also lies in the aspect that, the method of multiplicative decomposition of thermal mechanical deformation gradient will be used for formulating corresponding constitutive theories in the thermodynamic framework. Multiplicative decomposition of thermal mechanical deformation gradient, which was first proposed by Stojanovic et al. [9], but received far less attention, especially in the biomechanics community. In fact, such a method appears to be more simple and suitable for being incorporated with temperature dependent thermal and mechanical properties. . One objective of the present study is to further elaborate on this topic and compare the results with the ones obtained by using classical theory of thermoelasticity [10] [11], thereby making an extension application of such method with direct incorporation of the experimental data regarding the temperature dependence material properties.

In fact, current research has shown that during thermal mechanical interaction, tissue endures thermal stress and deformation due to temperature variation [3, 12]. It indicates that biological materials can be further damaged by corresponding thermal induced mechanical deformation [6, 7, 13]. Numerous studies suggest that the mechanism of thermal ablation is related to macromolecular transitions in cells and tissues. Of these transitions, proteins denature predominantly between 40-80 °C, and

are acting as the most important macromolecular group to be affected by thermal ablation [14]. In fact, as with any denaturant where proteins unfold under force, both thermally and mechanically induced tissue deformations can affect the energy barrier to unfolding protein molecules from a relative native state to a transition state [7, 15] which may further or reverse damaging the biological body. Therefore, an alternative method to predict tissue thermal damage by taking into accounts of both thermal and mechanical effects of soft tissues will be further studied in our research.

Moving to nonlinear regime characterisation of stress-strain relationship caused by introducing external mechanical force during thermal ablation process, e.g., using an indenter style heating source to cure skin disease [16], the strain range may easily extend to cover the nonlinear portion of characterisation. Therefore, the nonlinear stress strain relationship would be a better choice for analysing soft tissues' responses during such thermal ablation process. However, there has been very limited research focusing on the extension of existed nonlinear biomaterial models to account for thermal effects, especially for analysing thermal ablation under both thermal and mechanical loads. To the best knowledge of the author, the mostly related research is done by McBride et al. [17], who have proposed an isotropic nonlinear thermal mechanical tissue model that account for combined thermal and mechanical stimuli, but this model appears lacking fundamental investigations of the constitutive relations. Considering a more general situation as in our research, the thermal-mechanical response of soft tissues under thermal and mechanical loads will be described using a nonlinear thermal mechanical model which also accounts for the effect of collagen fibre bundles that are embedded in most biological materials. Separating free energy density modelling into isotropic and anisotropic parts, it is usually assumed that anisotropy is

due to the collagen fibre bundles behaviour [18], while the ground substance behaving in an isotropic manner can be modelled using available nonlinear biomaterial models. The difference of our research also lies in the fact that, the method of multiplicative decomposition of thermal mechanical deformation gradient will be used for formulating of corresponding constitutive theories in the thermodynamic framework.

In terms of heat transfer pattern in soft tissues, both Fourier [19-22] and non-Fourier [23, 24] bioheat transfer theories will be studied in our research, although the controversy of non-Fourier bioheat transfer is still in the air [25]. While also taking consideration of thermal mechanical influence and performing tissue damage prediction, our self-developed simulation programs will be established using two numerical discretisation methods, i.e., Finite Difference Method (FDM) and Finite Element Method (FEM), to account for both regular and irregular tissue geometries. In addition, computation performance of established programs based on different numerical methods will also be studied. Specifically, a condensation method will be applied in the established non-Fourier based thermal mechanical model using FEM, while the total Lagrangian explicit dynamics will be chosen for discretising the established nonlinear thermal mechanical model to allow for maximized computation efficiency.

1.1 Objectives

Based on the description in the above section, research gaps are discovered in the area of thermal ablation simulation, that is, the thermally and mechanically induced soft tissue responses and their potential effects on thermal damage prediction during modelling and analysis of thermal ablation process.

Based on these gaps, our research objectives can be described as the following:

1) To model how thermally induced mechanical deformation is performed during thermal ablation under purely thermal and combined thermal and mechanical loads.

2) To investigate the effect of thermally and mechanically induced tissue deformation on tissue damage prediction.

3) To distinguish the performance of Fourier and non-Fourier law based bioheat transfer theories on estimating soft tissue's thermal and mechanical behaviours and damage.

4) To discretise and solve established mathematical models using suitable numerical methods and algorithms but also having the potential of realizing real time simulation.

5) To identify the influence of using linear and nonlinear stress-strain relationship on predicting soft tissue's thermal and mechanical responses.

6) To validate the obtained simulation results against commercialised software tools and/or experimental data in literatures.

1.2   Thesis structure

For the remaining parts of this thesis, a brief outline of each chapter is given as follows:

In Chapter 2, a background and literature review is provided in related fields.

In Chapter 3, it provides an approach for formulating the constitutive theory in the thermodynamic framework using the method of multiplicative decomposition of thermal mechanical deformation gradient.

In Chapter 4, it presents a model using FDM numerical method for prediction and analysis of temperature distribution and thermally induced mechanical deformation during thermal ablation under purely thermal load.

In Chapter 5, the combined impact of temperature and mechanical responses on thermal damage prediction is included in a presented damage prediction model extended from traditional chemical reaction rate model. Comparison simulations are also performed to identify the influence of thermal mechanical interaction on tissue damage prediction.

In Chapter 6, the presented model aims at capturing the non-Fourier bioheat transfer in this process. The established model using FEM numerical method is compared with FDM method from perspectives of accuracy and computing efficiency, and also against other commercialized software tools and experimental data in literatures.

In Chapter 7, it presents a model focusing on nonlinear range characterization of tissue response under combined thermal and mechanical loads during thermal ablation. Meanwhile, it also accounts for the complex microstructure of soft tissues by incorporating the critical role of collagen fibre bundles via an anisotropic constitutive model.

In Chapter 8, key contributions of the thesis are summarised and recommendations for future work are also provided.

2 Literature review

2.1 Background

Thermal ablation is an energy-based minimally invasive thermal therapy. It uses extreme temperature either high or low, for treatment of many tumour types, particularly unresectable tumours like hepatics, neoplasm in kidney, breast and lungs. The procedure uses energy sources, such as radiofrequency [26], laser [27], focused ultrasound and microwaves [28, 29], to generate thermal injury to cells within the tumour. But on implementing this treatment, current surgical procedure always comes with two main problems, namely, 1) inadequate intra-procedural monitoring modalities; 2) non-optimized power supply. These shortcomings make it difficult to control the precise formation of final coagulation zones, that is, to affect a volume sufficient to cover the entire tumour after treatment. Unsuccessful treatment cases shows that, excessive heating causes complications such as burns to neighbouring safety tissues, while insufficient heating increases the change of tumours recurrence from areas that have not been fully cauterized [30]. To overcome these difficulties, considerable research efforts have been dedicated to modelling and analysis of this treatment process. Building upon corresponding mathematical and numerical models, visualized computer pre-operation simulation system is becoming a more and more reliable tool for relevant surgeons to design better medical treatments and also for training purpose. Integrating such a system into existed surgical navigation or image-tracing module, it can also help surgeons with real time monitoring of tissue damage in an intra-operation manner. Taking the thermal treatment of liver tumour for example,

the concept of pre-operation simulation and intra-operation guiding is as illustrated in Figure 1.
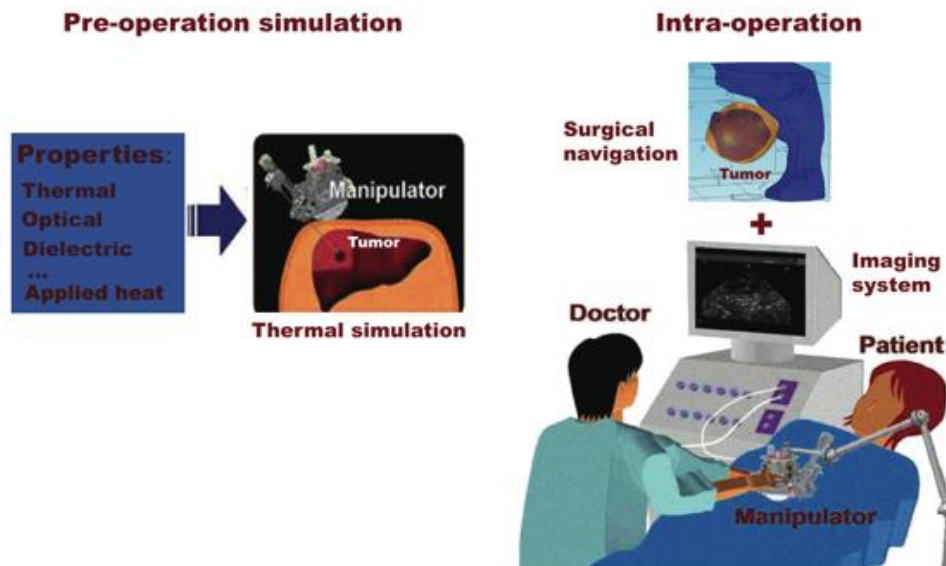
Figure 1: Pre-operation simulation of thermal ablation and intra-operation

2.2 Mechanism of thermal ablation

In particular, to introduce a high temperature based thermal ablation treatment, the fundamental mechanism of this heating therapy has to be investigated substantially. From a biological point of view, applying heat to human tissue, disturbs tissue microenvironment and damage cell at membrane and subcellular levels [31]. As shown in Figure 2, the affected area can be divided into three zones: central zone, transitional zone and normal surrounding zone. Within the central zone, tissue undergoes coagulative necrosis which is irreversible; in a transitional zone, there is also heat-induced injury but it is reversible; and the normal surrounding tissue is unaffected by thermal ablation. Featuring denaturation of proteins as the primary pattern, coagulative necrosis is also regarded as the target damage state within treated tissue.

As a current understanding [32], at temperatures around 40-45 °C, irreversible tissue damage occurs only after prolonged exposure. At temperatures above 60 °C, the time required to achieve irreversible damage decreases rapidly. In clinical application, variety of thermal techniques has been used to obtain such coagulative necrosis. Taking two most commonly used techniques for example: radio frequency ablation (RF) and microwave ablation (MW), RF ablation generates resistive heat that rising tissue temperature between 60 °C to 100 °C, by using electromagnetic field in hundreds of kilohertz to a few megahertz, while MW works at electromagnetic field between hundreds of megahertz to approximately ten gigahertz which can force the polar molecules (mainly water) to realign within this electric field. Therefore, under such condition, relatively higher tissue temperature can be achieved by MW technique compared to RF technique [33-36].
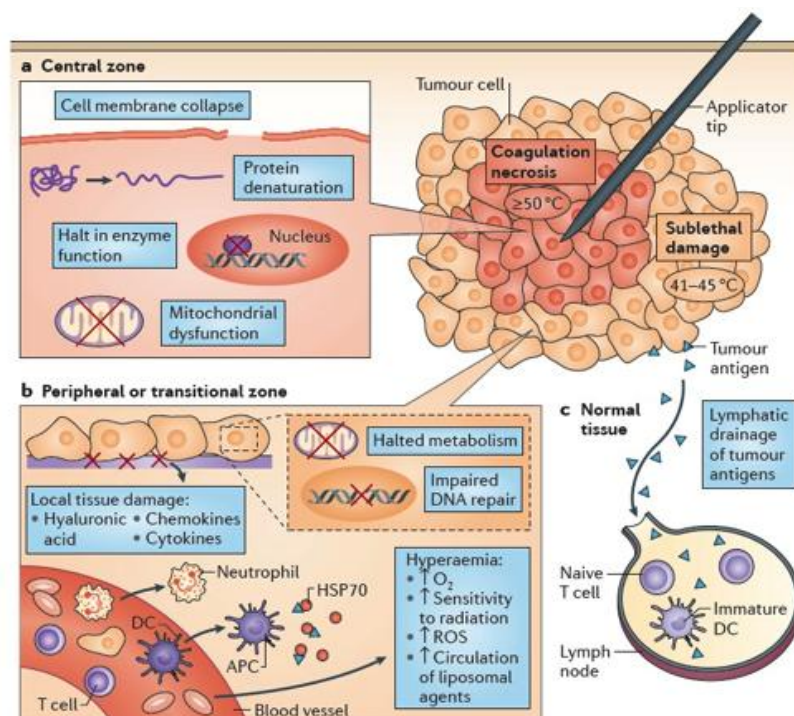
Figure 2: Mechanism of thermal ablation (Chu et al. [31])

2.3 Thermal and mechanical properties of soft tissues

In terms of composition, soft tissues are structurally complex, appears as hydrated composites of cells and extracellular matrix or ground substance. To characterize the behaviours of soft tissues under thermal and mechanical loads, variety of phenomenological properties can be applied which are obtained from a large number of physical experiments. These phenomenological properties include, elasticity [37-39], viscosity [39-41], thermal conductivity, heat capacity, heat diffusivity, et al. [1, 42, 43]. In general, when undergoing large deformation under purely mechanical stimuli, most soft tissues exhibit nonlinear elasticity. Meanwhile, such nonlinear stress-strain relationship also exhibits strain rate dependency [1, 3].

As in a wide variety of soft tissues, collagen and elastin fibres are the primary components of extracellular matrix and are acting as the main support of external physical loads. Based on a "quasi-static" loading to obtain mechanical data, i.e., conditions under which the tissue is deformed at very slow strain rates, e.g., the order of 6%/min. A typical tensile test of pig ear skin sample measured at a series of temperature is as shown in Figure 3 [3]. As described, these curves can be divided into three behaviour regimes, similar division can also be found in [2]. Firstly, $\varepsilon < 5\%$ the low strain portion (Stage A), where the curves almost overlap indicating that the modulus of tissue (tangent line) is thermally stable. This can be explained by referring to right image of Figure 3, where collagen fibres are in relaxed conditions and appear wavy, and elastin fibres are mainly responsible for the stretching mechanism. Secondly, $5\% < \varepsilon < 70\%$ the nonlinear region (Stage B), where nonlinear strain-stress relationship is observed, in this region, the elastin fibres effect is becoming ignorable from this stage, but the crimped collagen fibres gradually elongate and tend to line up

with the loading direction. Thirdly, 70% < ε < 80% the high strain linear region (Stage C), in this stage of high tensile stresses, crimped patterns disappear and the collagen fibres become straighter primarily aligned with one another in the direction of stretching. After a certain point, when the ultimate tensile strength is reached, a rupture may happen.
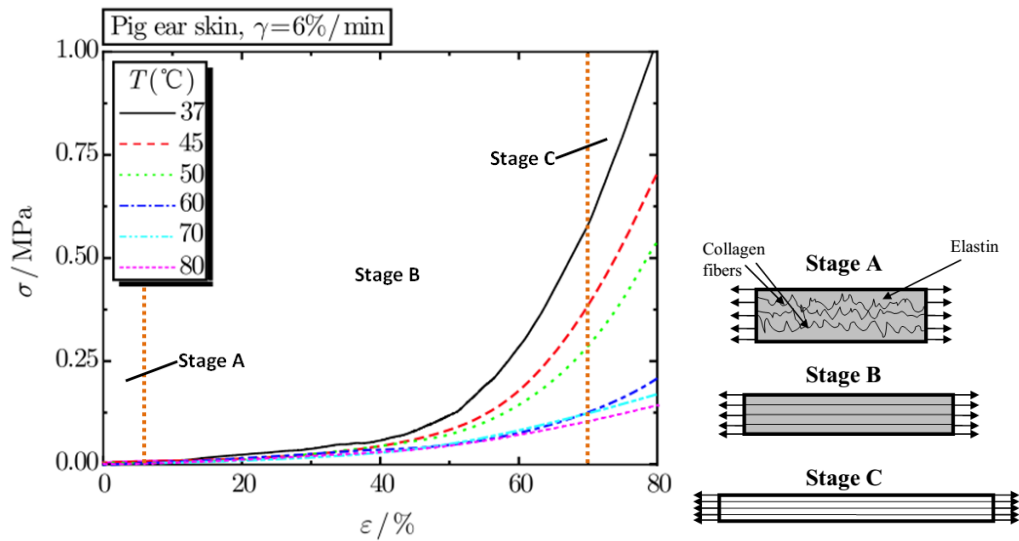
Figure 3: Stress-strain relation of uniaxial tensile tests under different temperatures (Xu et al. [3])

2.4   Bioheat transfer models

Different from other engineering materials, soft tissues also feature blood circulation, metabolic function, and so on. Therefore, to analyse heat transfer within it, these factors need to be considered. Based on the classical Fourier's law of heat transfer, a large number of research efforts have been exerted on to build corresponding tissue-thermal energy interaction models. Among them, the most well known one is Pennes' bioheat transfer equation [44]. Up to now, most of the thermal medical applications are based on this famous model. The following gives the different improvement directions based on Pennes' model in existed research works.

11

- Regarding the blood perfusion term in Pennes' equation, extensive studies have been conducted, which led to several new bioheat models. Among these models, Wulff [45] proposed using a directional convection term to model the blood flow contribution rather than the scalar perfusion term. Chen and Holmes [46] revealed that thermal equilibrium between blood and tissue is achieved mostly in medium sized blood vessels, and they established a tissue sub-continuum model that includes terms like directionality and convective heat transfer effects.

- Another important feature attracted attention in bioheat transfer modelling is the heat transfer due to juxtaposed artery-vein pairs during the counter flow. Mitchell and Myers [47] proposed a bioheat model describing the counter-current heat exchange between arteries and veins of the limbs, and with environment for the extremity of an animal. Weinbaum et al. [48, 49] presented a detailed three-layer theoretical model for tissue-vessel thermal interaction due to counter-current blood flow.

- Other research attentions were paid to the heat conduction term. Considering the Fourier's law based heat conduction as used in all continuum models, it assumes infinite speed of heat propagation in target material. In other words, a local change in temperature causes perturbation in the temperature at all points in the medium instantaneously, no matter how far the points are located. Although, Fourier's law is applicable in many real life problems, it gives erroneous results with materials with non-homogenous inner structure as in the case of soft tissues. From a theoretical viewpoint, Xu et al. [24] demonstrated that non-Fourier feature may play an important role in thermal behaviour of skin tissue in different cases with varied thermal relaxation times.

Such non-Fourier thermal behaviour in biological tissue has also been experimentally observed in literatures. Among these studies, Mitra et al. [50] have observed the temperature jumps within processed meat for different simulation conditions. Specially, for short-pulsed and continuous wave laser irradiation, Banerjee et al. [23] demonstrated that non-Fourier heat conduction equation is a better approximation than the traditional Fourier heat conduction formulation compared with measured temperature profiles in different materials such as processed meat samples and tissue phantoms. Wakeni [51] applied a generalized thermal model which is represented through the non-classical heat conduction parameter that is related to the characteristic speed of thermal wave in biological tissue. Chen [52] presented the ballistic-diffusive heat-conduction equations that are applicable to transient heat conduction at scales when the mean free path is comparable to the system size and when the time is comparable to the carrier relaxation time. Anderson et al. proposed a C- and F-processes model with the assumption of the simultaneous coexistence of Fourier-type fast processes that have infinite speed of propagation and Cattaneo-type slow processes that have finite speed of propagation [53].

2.5 Thermal damage models

2.5.1 Critical thermal load approach

In terms of predicting thermal damage within heated tissue, the critical thermal load approach was often used during earlier times to quantify thermal damage in tissue, as expressed in the form of Eq. 2-1. It assumes that the total damage was a function of only total cumulative thermal dosage so that equal doses produced equal injury.

$$\Gamma = \int_0^t \mathbf{q}\, dt$$

where Γ is measure of thermal damage, $\mathbf{q}$ is the heat flux.

However, this method cannot explain the fact that a large amount of energy delivered over an extended period may produce no damage to the target tissue, but the same dose delivered within an extremely short duration may destroy the tissue.

2.5.2 Arrhenius model

Nowadays, the most widely applied damage model is Arrhenius model [28, 54-57], which indicates that a standard damage degree can be produced by progressively decreasing temperatures as the heating duration is logarithmically increased. The model form is as shown in Eq. 2-2, where the tissue damage Ω is related to the rate of protein denaturation and exposure time t at a given absolute temperature T. To define the concept of protein denaturation rate, it is assumed that tissue molecules absorbing an amount of energy reaching the activation energy ΔE are followed by decomposition of the molecules (protein denaturation) at a rate determined by A.

$$\Omega = A \int_0^t \exp\left(-\frac{\Delta E}{RT}\right) dt = \ln\left(\frac{C(0)}{C(t)}\right)$$

where A is a material parameter (frequency factor of decomposition of the molecules or damage rate factor); ΔE is the activation energy; R is the universal gas constant. Eq. 2-2 indicates that a reaction proceeds faster with larger values of A and smaller values of ΔE. The constants A and ΔE *are* usually obtained experimentally, for certain types of

14

soft tissues, their measured values are as listed in Table 1. Also from the right side of Eq. 2-2, when used to model thermal damage, the physical significance of the damage parameter, Ω, is that it is the natural log of the ratio of the original concentration of undamaged molecules, $C(0)$, to those remaining undamaged molecules at the conclusion of heating, $C(t)$.

According to Eq. 2-2, a damage integral of Ω = 1, corresponds to a 63% percent probability of cell death at a specific point. A damage integral of Ω = 4.6, corresponds to 99% percent probability of cell death at a point in the model [20]. The significance of Ω = 1 has been reported as the point at which tissue coagulation first occurs [58]. Therefore, in many researches it is usually used as the threshold of determining target tissue damage state.

Table 1: Arrhenius' constants for different tissues

Tissue	$A(\text{s}^{-1})$	ΔE (J/mol)	Reference
Retina	1.0×10^{44}	2.9×10^5	[59]
Skin	3.1×10^{98}	6.3×10^5	[60]
Liver	1.0×10^{70}	4.0×10^5	[61]

2.5.3 Thermal mechanical damage model

Focusing on the rate of protein denaturation as expressed in Eq. 2-2, Shen et al. [7] claimed that thermally induced tissue deformations can lower the energy barrier of protein denaturation by contribution of stored energy E_T. Their proposed thermal mechanical tissue damage model is in the following form,

$$\Omega = A \int_0^t exp\left(-\frac{\Delta E - E_T}{RT}\right) dt$$

where E_T is the stored strain energy by thermal loading, which is further represented by Eq. 2-4, where V_{mol} stands for the molar volume of target tissue.

$$E_T = \frac{1}{2} V_{mol} \sigma_{ij} \varepsilon_{ij}$$

The above strain and stress $\boldsymbol{\sigma}$ and $\boldsymbol{\varepsilon}$ are represented in the following forms of linear thermoelasticity [6, 7], with $\boldsymbol{\tau}$ and $\boldsymbol{\gamma}$ defined as engineering stress and strain.

$$\begin{bmatrix} \sigma_{xx} \\ \sigma_{yy} \\ \sigma_{zz} \\ \tau_{xy} \\ \tau_{yz} \\ \tau_{xz} \end{bmatrix} = \begin{bmatrix} 2\mu + \lambda & \lambda & \lambda & 0 & 0 & 0 \\ \lambda & 2\mu + \lambda & \lambda & 0 & 0 & 0 \\ \lambda & \lambda & 2\mu + \lambda & 0 & 0 & 0 \\ 0 & 0 & 0 & \mu & 0 & 0 \\ 0 & 0 & 0 & 0 & \mu & 0 \\ 0 & 0 & 0 & 0 & 0 & \mu \end{bmatrix} \begin{bmatrix} \varepsilon_{xx} \\ \varepsilon_{yy} \\ \varepsilon_{zz} \\ \gamma_{xy} \\ \gamma_{yz} \\ \gamma_{xz} \end{bmatrix} - [\theta - \theta_0] \begin{bmatrix} \beta \\ \beta \\ \beta \\ 0 \\ 0 \\ 0 \end{bmatrix}$$

with,

$$2\mu = \frac{E}{1+v}, \lambda = \frac{vE}{(1+v)(1-2v)}, \beta = \frac{\alpha E}{1-2v}$$

here $(\theta - \theta_0)$ temperature difference with respect to initial temperature is θ_0, E is the Young's modulus, v is the Poisson's ratio, and α is the constant linear coefficient of thermal expansion.

However, such an influence of thermal mechanical deformation is not distinguished very well from separated thermal and mechanical effects, because it only considers the situation due to thermal variation while the external mechanical stimuli is ignored. In fact, in practical application of thermal therapy, the movement of operation tool/device for delivering heat is usually not easy to avoid. In some applications, such external

mechanical loading is even designed to come with thermal loading, for instance, an indenter heating of skin tissue to cure its disease [16]. To account for such situation, our research will cover both purely thermal and combined thermal and mechanical loading; and the combined thermal and mechanical effects on tissue damage prediction will be further studied.

Further, considering the lack of fundamental investigations of constitutive relations in the work of Shen et al. in [6, 7], the method of multiplicative decomposition of thermal mechanical deformation gradient will be used for formulating of corresponding constitutive theories in the thermodynamic framework. Firstly proposed by Stojanovic et al. [9] but received far less attention, especially in the biomechanics community, the use of multiplicative decomposition of thermal mechanical deformation gradient appears more suitable of being incorporated with temperature dependent thermal and mechanical properties that obtained from physical experiments.

2.6 Characterization of the nonlinear behaviour of soft tissues

2.6.1 Nonlinear constitutive models

Soft biological tissues are usually taken to be hyperelastic when undergo large deformations. The existing constitutive models to predict the non-linear behaviour of biomaterials can be generally divided into two main categories. One is phenomenological models, includes but not limited to the Mooney-Rivlin [62, 63], Ogden [64], Yeoh [65] and Gent [66] hyperelastic models. Basically, these models are just fittings to experimental data. The other ones are molecularly inspired models, such as the Neo-Hookean [67-69], eight-chain Arruda-Boyce [70] and Bergstrom-Boyce [71] hyperelastic models. In this category of models, the model parameters are calculated by

means of statistical mechanics of biomaterials, while the mechanical properties are resulted from molecular structure of biomaterials. One reason for the attractiveness of these entropic elasticity models is that they reproduce the experimentally-observed response of soft biological tissue in uniaxial tension. However, it should be pointed out that it is not clear whether the highly bonded and hierarchical structure of collagen allows degrees of freedom for all states to be sampled in an entropy-dominated regime. Alternatively, some energetic elasticity models were also proposed to model the stiffening behaviour by the uncoiling of crimps [72].

2.6.2 Anisotropic feature of fibre bundles reinforced soft tissues

For many collagen fibre bundles reinforced soft tissue, it also has an anisotropic nature due to the collagen fibre bundles behaviour [18]. The effect of collagen fibre bundles orientations on the behaviour of soft tissue rests in the tortuosity and bending stiffness of embedded collagen fibre bundles [73]. According to the specific functions of different soft tissues, collagen fibre bundles are oriented in different directions. For example, artery tissue has fibre bundles arranged in the axial-circumferential polar plane to limit inflectional and axial deformation. This anisotropic arrangement can be as complex as orthotropic. Treating soft tissues as composites composed of a ground substance reinforced with stiffer collagen fibre bundles, while the ground substance, behaves in an isotropic manner, so the strain energy densities modelling of anisotropic soft tissues are usually separated into isotropic and anisotropic parts [74, 75].

2.7 Simulation parameters

2.7.1 Thermal parameters

In physical experiments, the thermal parameters of soft tissues have been measured mostly at constant temperature. For instance, the measured value for specific heat capacity in skin tissue at 37℃ is 3578-4000 J/(kg · K) [76] and 3510 J/(kg · K) in dog liver [77]. Thermal conductivity of human liver measured at 37℃ is 0.512 W/(m · K) [76] and 0.513-0.564 W/(m · K) for human kidney [78]. In some other physical experiments, standard values of thermal parameters for tissue like phantoms have also been reported. For example, the specific heat capacities of the different pH phantoms (4.3-4.7) are between 3481-3952 J/(kg · K) and the thermal conductivity are between 0.53-0.69 W/(m · K) [79].

2.7.2 Temperature dependent thermal parameters

In other researches, temperature dependent thermal properties have been studied. Among these studies, temperature dependent thermal conductivity of sheep collagen and cow liver in vitro was measured in temperature range from 25 ℃ to 90 ℃ [80]. For a similar temperature range of 25 ℃ to 83.5 ℃, temperature dependent specific heat was measured in bovine liver in vitro [81]. Particularly, Guntur et al. [42] has plotted curves of these two key thermal parameters measured in ex vivo porcine liver being heated from 20 ℃ to 90 ℃ and then naturally cooled down to 20 ℃. As shown in Figure 4, plots of specific heat capacity and thermal conductivity versus temperature are both asymmetric quasi-parabolic curves. Each curve is concave downward with minima at about 30 ℃ to 40 ℃, where the maximum decrease of corresponding parameter is less than 15% of the initial value at 20 ℃, and then it rises as much as 45% from the

minima. On the other hand, during the natural cooling period, both of two thermal parameters change very little with temperature.
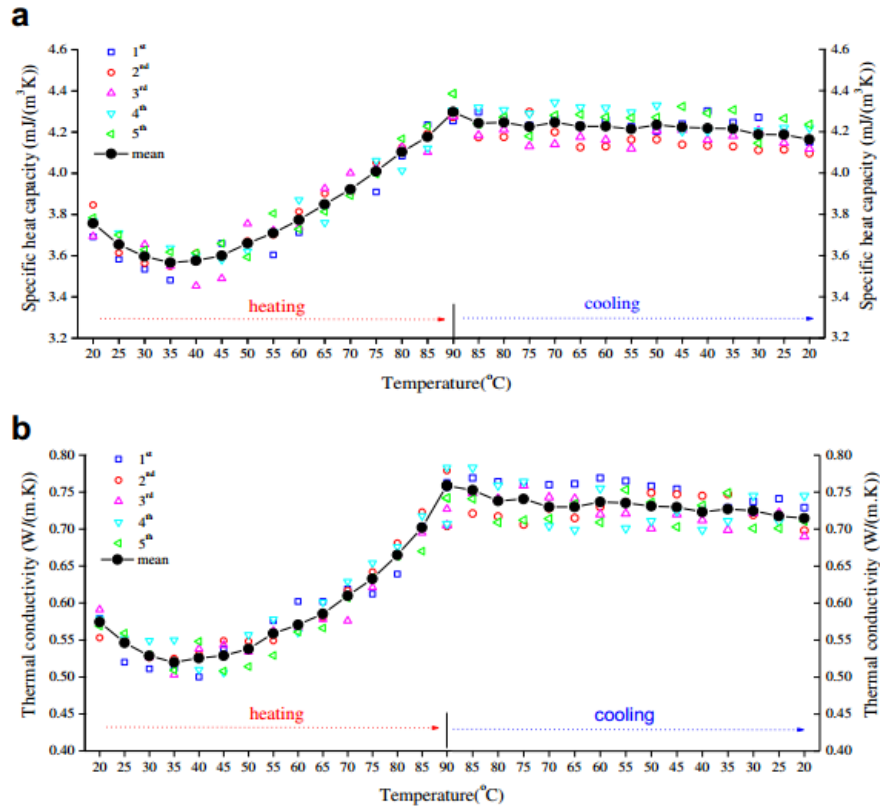
Figure 4: Thermal parameters of liver tissue vs. temperature (a) Specific heat capacity (b) Thermal conductivity (Guntur et al. [42])

2.7.3   Mechanical parameters

As the main constitute of most soft tissues, mechanical properties of collagen fibres have already been studied extensively, and it is shown that they are mostly with Young's modulus from about 100 MPa [82] to even 1 GPa [83]. However, the constitutive response of tissues can't be explained solely in terms of the constitutive properties of an individual collagen fiber. It has been shown that the Young's modulus of skin tissue is only in the order of 1 MPa at low strains [3]. For another tissue type,

the Young's modulus of liver tissue used in literature for simulation of its mechanical response under linear assumption are reported to be 102 MPa in [84], 10.2 MPa in [85] and 1.1 MPa in [86]. While in other research works, e.g. in [87], the Young's modulus is set to be 3000 Pa to describe a "very" soft kind of tissues (such as the brain, kidney et al.). For another key mechanical property, the Poisson ratio represents the degree to which a material expands laterally as it is strained (compressed) axially. And it is observed that most soft tissues are with a Poisson ratio in the range of $0.3 < v < 0.5$ [88].

2.7.4   Temperature dependent mechanical parameters

As mentioned above, for a typical type of soft tissue dominated by collagen fibres, the stress strain curve can be divided into three parts: the initial linear region, the second nonlinear region and the third linear region. Quantifying the Young's modulus using a linear fit of the first part of stress strain curves, significant decrease in Young's modulus for skin specimens is observed after thermal treatment at increasing temperatures, as shown in the work of [89]. It also demonstrates that, only slight decrease in Young's modulus is observed at thermal treatment of 70 °C than that at 60 °C (see Figure 5), which indicates a severe thermal damage happens above 60 °C for target tissue.
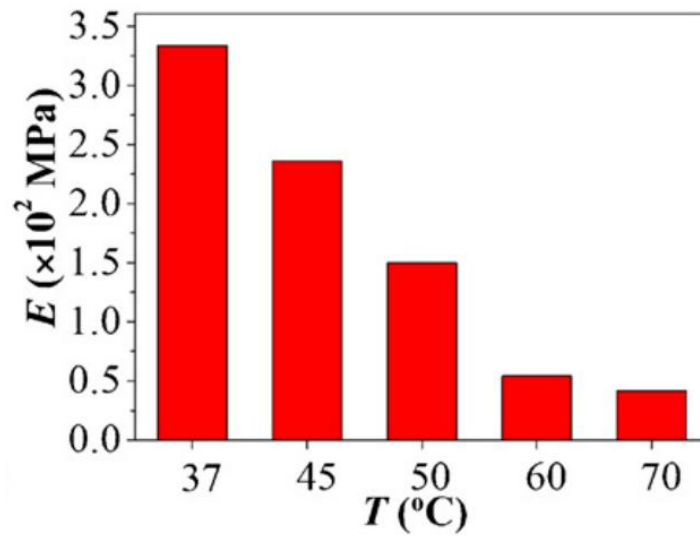
Figure 5: Changes in Young's modulus at different temperatures (Lin et al. [89])

Moving to the nonlinear part characterisation of soft tissue's stress strain behaviour, in a phenomenological theory based model the constitutive parameters are dictated only by the functional form considered, while in a molecular theory based model the parameters are introduced on the basis of the modelled phenomena and consequently are related ex ante to physical quantities. For instance, the Neo-Hookean model comes out of the molecular theory, in which the rubber-like material is regarded as a three-dimensional network of long-chain molecules that are cross-linked at a few points [67-69]. The elementary molecular theory of networks is based on the postulate that the elastic free energy of a network is equal to the sum of the elastic free energies of the individual molecular chains. In this framework the key constitutive parameter μ is determined by micromechanics parameters, which is temperature dependent and can be expressed as: $\mu = NKT$, where N the crosslink density, K is the Boltzmann constant and T is the temperature. More elaborate models could also be used to determine the temperature dependency of biomaterials' mechanical properties, e.g. as done by

Mlyniec et al. [90], but it is not the objective of the present study as well as the temperature dependent thermal properties.

2.8   Numerical modelling methods

As we can see, independent pre-operation simulator and the surgery navigation module incorporated within the image tracing system has a higher requirement on accuracy as well as the ability of performing real time simulation. Taking these into mind, both computing accuracy and speed would be very concerned while programming our established models into computer. Comparing the commonly used numerical methods, such as Finite Difference Method (FDM), Finite Element Method (FEM) and Mass Spring Model (MS), continuum constitutive theory based FDM method owns its application maturity and simplicity, but it only serves regular meshes; while FEM is a reachable method for dealing with irregular geometry. In general, both FDM and FEM methods have higher computation accuracy than MS [91-93], while discrete theory based MS model features the appealing computing efficiency that the other two methods cannot compare with. Considering the computing accuracy is the priority in our research, continuum constitutive theory based FDM and FEM methods would be more suitable compared with the discrete theory based MS model.

Among the research effort of applying continuum constitutive theory based discretisation methods: FDM and FEM, various mathematical and computer-based simulation models have been developed for pre-operation thermal ablation planning purpose according to different types of heating sources. Prakash et al. [28, 94] have established a 3D acoustic bio-thermal model based on commercialized FEM tool COMSOL, where both acoustic energy distributions and transient temperature profiles

in tissue during heating were investigated. For radio frequency heating sources, Watanabe et al. [95, 96] have used two-dimensional FEM to simulate temperature distribution in the target organ and subsequently generate the size and shape of coagulation zone based on the dimensions of the tumour. Hills [97] has realized the simulation of bioheat transfer during radio frequency ablation to a real time manner by Graphics Processing Unit (GPU) accelerated FEM. In terms of microwave ablation, Rattanadecho et al. [85, 98] reported an axisymmetric FEM to study heat transfer and blood flow, coupled with electromagnetic wave propagation in liver tissue. Wu et al. [99] have used the GPU accelerated explicit Finite Difference Time Domain (FDTD) codes to calculate the SAR and the temperature distribution. Basically, all the above models only focus on the temperature distribution to determine an optimize thermal dose, while neglecting or underestimating the accompanied phenomenon of thermal-mechanical deformation of target tissue, as well as its insight on making the above decisions.

The only few related studies on thermal-mechanical interaction of soft tissue are found in the area of skin burns. Among these study, Xu et al. treated the human skin as a kind of composite material, laminate, where heat-induced mechanical response was calculated based on related theories and FEM formulations [3-5]. Shen et al. reported a quasi-static numerical model based on FDM to predict the linear thermoelastic deformation of skin tissue at high temperature [6, 7]. Lozano et al. analysed the radio frequency heating of cutaneous and subcutaneous tissues, including their linear thermoelastic response based on commercialized FEM tool [8]. McBride et al. [17] have proposed an isotropic nonlinear thermal mechanical tissue model that account for combined thermal and mechanical stimuli by applying FEM formulation. Other research works that shed light on our particular research purpose is the research area

of classical and non-classical thermomechanical theoretical and numerical modelling [100]. Besides, Zhou et al. [101] proposed a new C- and F-processes model based on generalized thermoelastic theory that readily encompasses the classical and non-classical dynamic thermoelasticity theories. However, these methods either base on commercialized analysis tools [3-5] [8] [17] or lack accounting for irregular tissue geometry and time domain analysis [6, 7], which are practically not suitable for real time simulation purpose.

2.9   Time integration methods

Explicit time integration methods are commonly used in real time simulation of soft tissue responses under thermal or mechanical loads. Basically, in an explicit method, the update of field data at current iteration is only relied on information of known field data at previous iterations. Therefore, no simultaneous linear equations need to be solved, which required costly computation effort upon solving the inversion of coefficient matrix. But the stability of explicit integration scheme is conditional confined by Courant Friedrichs Lewy (CFL) condition [102]. On the other hand, implicit time integration method can be made unconditionally stable, because the update of field data is relying on both current and previous iterations. However, depending on the complexity of produced simultaneous linear system, which is governed by the dimensions of problem, discretisation strategy as well as the altering of target material properties, the implicit integration scheme may be computational expensive to realise interactive simulation [102]. For instance, in a typical interactive simulation system of soft tissue, it requires a minimum update rate of 15-20 frames/second to realize real-time performance [103]. Therefore, if the solving of single iteration using implicit integration scheme is within this time limit, it would be a better choice to use implicit

method than explicit method since simple explicit method is usually highly dissipative. Otherwise, explicit method would be the proper choice.

2.10 Numerical solvers

After standard discretisations of partial differential equations as for most engineering problems, typically a sparse linear system of equations would be obtained, denoted as $Bx = b$. To solve these linear algebraic equations, two types of numerical solvers are normally used, namely direct methods and iterative methods. Direct methods such as Gaussian Elimination and LU-Factorization Method are not appropriate for solving large number of equations in a system, particularly when the coefficient matrix is sparse. In contrast, iterative methods give the best possible solution for the problems with sparse matrices efficiently. Iterative methods include Jacobi Method, Gauss Seidel Method, Conjugate gradient Method, GMRES Method, Multigrid Method et al. Comparing these methods as done in [104], for the same sparse linear system within the same tolerance factor, Jacobi method takes longer time (more iterations) to converge as compared to other methods, while Gauss Seidel Method and GMRES method are promoted more efficient on solving the linear systems of equations. Based on iterative methods, using preconditioning techniques can also accelerate the solution of a system of linear equations, e.g. with ILUT preconditioner [7]. Another alternative for accelerating solving speed is by applying a projected variation to accelerate convergence [105]. Compared with other iterative methods, which require a large number of iterations until convergence of the solution, that is, looking at the frequency spectrum of the residual reveals that high frequencies in the solution are damped out very quickly by the relaxation, Multigrid Method based on the idea of solving the residual equation at a coarser grid to achieve improved convergence [106]. For the

sake of simplicity during implementation, a Gauss-Seidel iterative solver would be developed and incorporated into the chosen numerical methods (FDM, FEM) for solving obtained linear system of equations in our research, and a specified margin of error must be addressed for some satisfactory level of convergence.

3 Multiplicative decomposition of thermal mechanical deformation

Basically, the method of multiplicative decomposition of thermal mechanical deformation gradient is based on the introduction of an intermediate configuration, which is obtained by a conceptual isothermal distressing of the current deformed material configuration to zero stress. The total thermal mechanical deformation gradient is then decomposed into the product of purely thermal and elastic parts.

In contrast to the decomposition of elastoplastic deformation gradient in the phenomenological finite strain plasticity [107-109], the decomposition of the thermal mechanical gradient, which was first proposed by Stojanovic et al. [9], received far less attention, especially in the biomechanics community. However, as an optional approach for formulating of the constitutive theory in the thermodynamic framework, the use of multiplicative decomposition of thermal mechanical deformation gradient appears more suitable of being incorporated with temperature dependent thermal and mechanical properties that obtained from physical experiments.

Based on the multiplicative decomposition of thermal mechanical deformation gradient method, the following sections give the fundamentals during the formulation of constitutive theories of biomaterial responses. Further formulations under thermally induced mechanical deformations and finite mechanical deformations as occurs under purely thermal and combined thermal and mechanical loadings during thermal ablation, will be described in subsequent chapters.

3.1 Constitutive equation

If $\mathbf{q}_0$ is the heat flow rate in the initial configuration, $\boldsymbol{\nabla}_0$ is the gradient operator with respect to initial coordinates, ρ_0 and ρ are the density of initial and deformed configurations, u is the internal energy. The principle of energy conservation (first law of thermodynamics) is applied as,

$$\dot{u} = \frac{1}{\rho_0}\left(\mathbf{S}\!:\!\dot{\mathbf{E}} - \boldsymbol{\nabla}_0 \cdot \mathbf{q}_0\right)$$

<div align="right">Eq. 3-1</div>

where the second Piola-Kirchhof stress tensor $\mathbf{S}$ is introduced in the term $\mathbf{S}\!:\!\dot{\mathbf{E}}$, which is a work conjugate to Green-Lagrange strain tensor $\mathbf{E}$.

Since the rate of the specific entropy η is due to heat flow only, θ is current temperature, so that,

$$\theta\dot{\eta} = -\frac{1}{\rho_0}\boldsymbol{\nabla}_0 \cdot \mathbf{q}_0$$

<div align="right">Eq. 3-2</div>

Recalling Helmholtz free energy per unit mass, $\psi = u - \theta\eta$, and combining it with Eq. 3-1 and Eq. 3-2 , the rate of Helmholtz free energy can be written as,

$$\dot{\psi} = \frac{1}{\rho_0}\mathbf{S}\!:\!\dot{\mathbf{E}} - \eta\dot{\theta}$$

<div align="right">Eq. 3-3</div>

The above expression also shows that $\psi = \psi(\mathbf{E}, \theta)$ is the function to determine stress $\mathbf{S}$ and entropy η, therefore we have,

$$\dot{\psi} = \frac{\partial \psi}{\partial \mathbf{E}} : \dot{\mathbf{E}} + \frac{\partial \psi}{\partial \theta} \dot{\theta}$$

Comparing Eq. 3-3 with Eq. 3-4, we also have [110],

$$\mathbf{S} = \frac{\partial (\rho_0 \psi)}{\partial \mathbf{E}}$$
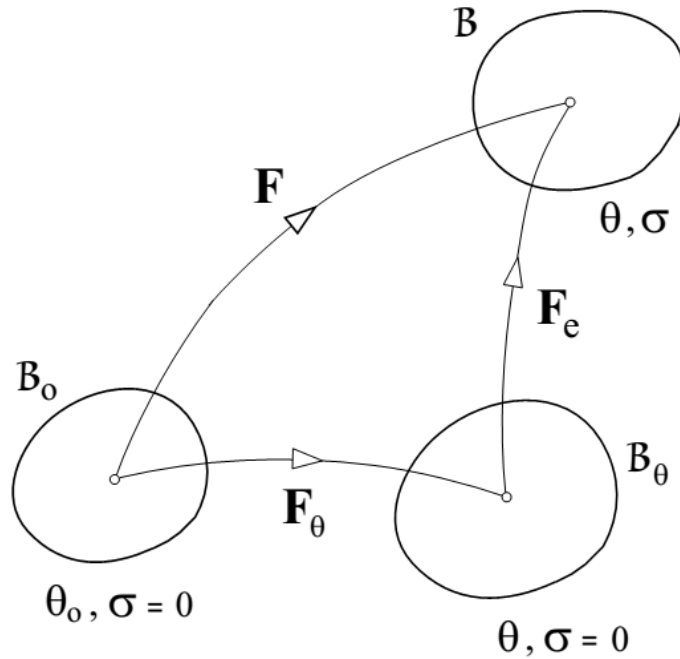
Figure 6: The decomposition of deformation gradient

Let $\mathcal{B}_0$ be the initial configuration of reference sample with zero stress, $\mathcal{B}$ is defined as the current configuration after thermal mechanical deformation. The configuration $\mathcal{B}_\theta$ denotes an intermediate state which is obtained from $\mathcal{B}$ by isothermal elastic de-stressing to zero stress. $\mathbf{F}$ is a material deformation gradient mapping $\mathcal{B}_0$ to $\mathcal{B}$, $\mathbf{F}_\theta$ denotes mapping from $\mathcal{B}_0$ to $\mathcal{B}_\theta$, $\mathbf{F}_e$ is the elastic deformation gradient mapping $\mathcal{B}_\theta$ to

$\pmb{B}$. The total thermal mechanical deformation gradient can be decomposed into the elastic and thermal parts as [111],

$$\mathbf{F} = \mathbf{F}_e \cdot \mathbf{F}_\theta$$

Meanwhile, rewrite the strain tensor in Lagrangian form, so that,

$$\mathbf{E}_e = \frac{1}{2}\left(\mathbf{F}_e^{\mathrm{T}} \cdot \mathbf{F}_e - \mathbf{I}\right), \quad \mathbf{E}_\theta = \frac{1}{2}\left(\mathbf{F}_\theta^{\mathrm{T}} \cdot \mathbf{F}_\theta - \mathbf{I}\right)$$

$$\mathbf{E} = \frac{1}{2}\left(\mathbf{F}^{\mathrm{T}}\mathbf{F} - \mathbf{I}\right) = \frac{1}{2}\left(\mathbf{F}_\theta^{\mathrm{T}}\mathbf{F}_e^{\mathrm{T}}\mathbf{F}_e\mathbf{F}_\theta - \mathbf{I}\right) = \mathbf{F}_\theta^{\mathrm{T}}\mathbf{E}_e\mathbf{F}_\theta + \mathbf{E}_\theta$$

$$\mathbf{E}_e = \mathbf{F}_\theta^{-\mathrm{T}}(\mathbf{E} - \mathbf{E}_\theta)\mathbf{F}_\theta^{-1}$$

$$\dot{\mathbf{E}}_e = \mathbf{F}_\theta^{-\mathrm{T}}\dot{\mathbf{E}}\mathbf{F}_\theta^{-1} + \dot{\mathbf{F}}_\theta^{-\mathrm{T}}\mathbf{E}\mathbf{F}_\theta^{-1} + \mathbf{F}_\theta^{-\mathrm{T}}\mathbf{E}\dot{\mathbf{F}}_\theta^{-1} - \mathbf{F}_\theta^{-\mathrm{T}}\dot{\mathbf{E}}_\theta\mathbf{F}_\theta^{-1} - \dot{\mathbf{F}}_\theta^{-\mathrm{T}}\mathbf{E}_\theta\mathbf{F}_\theta^{-1} - \mathbf{F}_\theta^{-\mathrm{T}}\mathbf{E}_\theta\dot{\mathbf{F}}_\theta^{-1}$$

Helmholtz free energy equation can be reformed into,

$$\psi = \psi_e(\mathbf{E}_e, \theta) + \psi_\theta(\theta)$$

And the time rate of the above equation is,

$$\dot{\psi} = \frac{\partial \psi_e}{\partial \mathbf{E}_e} : \dot{\mathbf{E}}_e + \frac{\partial \psi_e}{\partial \theta}\dot{\theta} + \frac{d\psi_\theta}{d\theta}\dot{\theta}$$

Substituting Eq. 3-10 into Eq. 3-12, yields,

$$\dot{\psi} = \frac{\partial \psi_e}{\partial \mathbf{E}_e} : \left(\mathbf{F}_\theta^{-T} \dot{\mathbf{E}} \mathbf{F}_\theta^{-1} \right)$$

$$+ \frac{\partial \psi_e}{\partial \mathbf{E}_e} : \left(\dot{\mathbf{F}}_\theta^{-T} \mathbf{E} \mathbf{F}_\theta^{-1} + \mathbf{F}_\theta^{-T} \mathbf{E} \dot{\mathbf{F}}_\theta^{-1} - \mathbf{F}_\theta^{-T} \dot{\mathbf{E}}_\theta \mathbf{F}_\theta^{-1} - \dot{\mathbf{F}}_\theta^{-T} \mathbf{E}_\theta \mathbf{F}_\theta^{-1} \right.$$

$$\left. - \mathbf{F}_\theta^{-T} \mathbf{E}_\theta \dot{\mathbf{F}}_\theta^{-1} \right) + \frac{\partial \psi_e}{\partial \theta} \dot{\theta} + \frac{d\psi_\theta}{d\theta} \dot{\theta}$$

<div align="right">Eq. 3-13</div>

Considering the second term on the right side of Eq. 3-13 can be written as a function of $\dot{\theta}$, therefore, comparing Eq. 3-13 with Eq. 3-4, the stress **S** can be expressed as,

$$\mathbf{S} = \rho_0 \mathbf{F}_\theta^{-1} \cdot \frac{\partial \psi_e}{\partial \mathbf{E}_e} \cdot \mathbf{F}_\theta^{-T}$$

<div align="right">Eq. 3-14</div>

The density of reference configuration $\mathcal{B}_0$ and $\mathcal{B}_\theta$ has such relationship as $\rho_0 = (det\mathbf{F}_\theta)\rho_\theta$, Substituting it into the above equation, so that,

$$\mathbf{S} = (det\mathbf{F}_\theta)\mathbf{F}_\theta^{-1} \cdot \frac{\partial(\rho_\theta \psi_e)}{\partial \mathbf{E}_e} \cdot \mathbf{F}_\theta^{-T} = (det\mathbf{F}_\theta)\mathbf{F}_\theta^{-1} \cdot \mathbf{S}_e \cdot \mathbf{F}_\theta^{-T}$$

<div align="right">Eq. 3-15</div>

3.2 Heat transfer

Since function $\psi = \psi(\mathbf{E}, \theta)$ is function for determining the stress *S* and entropy η, by comparing Eq. 3-3 with Eq. 3-4, we can also derive,

$$\eta = -\frac{\partial \psi}{\partial \theta}$$

<div align="right">Eq. 3-16</div>

Suppose heat conduction in soft tissues is governed by Fourier's law, we have heat flow expressed as,

$$\mathbf{q}_0 = -\mathbf{k}_0(\mathbf{F}, \theta) \cdot \mathbf{\nabla}_0 \theta$$

Substituting Eq. 3-17 into Eq. 3-2, we get [112],

$$\theta \dot{\eta} = \frac{1}{\rho_0} \left[\mathbf{k}_0 : (\mathbf{\nabla}_0 \otimes \mathbf{\nabla}_0) \theta + \frac{\partial \mathbf{k}_0}{\partial \theta} : (\mathbf{\nabla}_0 \theta \otimes \mathbf{\nabla}_0 \theta) \right]$$

Recalling Eq. 3-16 and Eq. 3-4, one also has,

$$\theta \dot{\eta} = -\theta \left(\frac{\partial \left(\frac{\partial \psi}{\partial \mathbf{E}} : \dot{\mathbf{E}} + \frac{\partial \psi}{\partial \theta} \dot{\theta} \right)}{\partial \theta} \right) = -\theta \left(\frac{\partial^2 \psi}{\partial \mathbf{E} \partial \theta} : \dot{\mathbf{E}} + \frac{\partial^2 \psi}{\partial \theta^2} \dot{\theta} \right)$$

Comparing Eq. 3-18 and Eq. 3-19, one can derives that,

$$-\theta \left(\frac{\partial^2 \psi}{\partial \mathbf{E} \partial \theta} : \dot{\mathbf{E}} + \frac{\partial^2 \psi}{\partial \theta^2} \dot{\theta} \right) = \frac{1}{\rho_0} \left[\mathbf{k}_0 : (\mathbf{\nabla}_0 \otimes \mathbf{\nabla}_0) \theta + \frac{\partial \mathbf{k}_0}{\partial \theta} : (\mathbf{\nabla}_0 \theta \otimes \mathbf{\nabla}_0 \theta) \right]$$

Introducing C to stand for specific heat,

$$C = \theta \frac{\partial \eta}{\partial \theta} = -\theta \frac{\partial^2 \psi}{\partial \theta^2}$$

Using Eq. 3-21 and Eq. 3-5 to rewrite Eq. 3-20, yields,

$$C\dot{\theta} = \frac{1}{\rho_0} \left[\mathbf{k}_0 : (\mathbf{\nabla}_0 \otimes \mathbf{\nabla}_0) \theta + \frac{\partial \mathbf{k}_0}{\partial \theta} : (\mathbf{\nabla}_0 \theta \otimes \mathbf{\nabla}_0 \theta) \right] + \frac{1}{\rho_0} \theta \frac{\partial \mathbf{S}}{\partial \theta} : \dot{\mathbf{E}}$$

4 Fourier based thermal mechanical model using FDM

Focusing on the modelling and analysis of thermal mechanical responses during thermal ablation with purely thermal loading, in this section, soft tissue is treated as thermoelastic continuum media for a macroscopic level of modelling. Based on the multiplicative decomposition of thermal mechanical deformation gradient method, Chapter 3 gives the formulation of corresponding constitutive model and heat transfer equations. In this Chapter, the next step of formulation is focused on the features of target soft tissues by assuming that the tissue body is: 1) a type of elastically and thermally isotropic material; 2) heat transfer within it abbeys the Fourier's law model; and 3) it also has metabolic heat generation and embedded blood vessel perfusion. Combining the formulated constitutive and heat transfer equations with law of non-rigid mechanics of motion, the governing equations are then solved spatially by numerical method FDM and temporally by implicit time scheme.

4.1 Governing equations

4.1.1 Isotropic linear material under thermal loads

Following the deviation of constitutive equations in Chapter 3, in the following section, the considerations are now restricted to elastically and thermally isotropic biomaterials. Assuming $\varsigma(\theta)$ is the stretch ratio, the deformation gradient caused by thermal load can be expressed as,

$$\mathbf{F}_\theta = \varsigma(\theta)\mathbf{I}$$

<div align="right">Eq. 4-1</div>

Substituting Eq. 4-1 back into Eq. 3-7 and Eq. 3-14, we have,

34

$$\mathbf{E}_e = \frac{1}{\varsigma^2(\theta)}(\mathbf{E} - \mathbf{E}_\theta), \ \ \mathbf{E}_\theta = \frac{1}{2}(\varsigma^2(\theta) - 1)\mathbf{I}$$

$$\mathbf{S} = \frac{\rho_0}{\varsigma^2(\theta)}\frac{\partial \psi_e}{\partial \mathbf{E}_e}$$

Also, the relationship between ρ_0 and ρ_θ can be expressed as,

$$\rho_0 = (det\mathbf{F}_\theta)\rho_\theta = \varsigma^3(\theta)\rho_\theta$$

Therefore, we can rewrite Eq. 4-3 into the following two equations,

$$\mathbf{S} = \varsigma(\theta)\mathbf{S}_e, \ \mathbf{S}_e = \rho_\theta \frac{\partial \psi_e}{\partial \mathbf{E}_e}$$

Assuming $\alpha(\theta)$ to be the coefficient of thermal expansion at temperature θ [113],

$$\varsigma(\theta) = exp\left[\int_{\theta_0}^{\theta} \alpha(\theta)\,d\theta\right]$$

Focusing on the limit of the first linear region (section 2.3), Delingette et al. [114] admitted that it is reasonable to consider that a material is linear elastic when strains are less than 5%. While other researchers, e.g., Liu et al. [115] indicated that the linear region is only valid for strains less than 0.2%. Considering the small strain caused by purely thermal loading in the case of thermal ablation, the following free energy of isotropic linear soft tissues is assumed to estimate its determined linear strain stress relationship, in the form of,

$$\rho_\theta \psi_e = \frac{1}{2}\lambda(\theta)(tr\mathbf{E}_e)^2 + \mu(\theta)\mathbf{E}_e : \mathbf{E}_e$$

where $\lambda(\theta)$ and $\mu(\theta)$ are temperature dependent Lame parameters. Since $\mathbf{S}_e = \rho_\theta \frac{\partial \psi_e}{\partial \mathbf{E}_e}$ from Eq. 4-5, substituting Eq. 4-7 into it, yields,

$$\mathbf{S}_e = \lambda(\theta)(tr\mathbf{E}_e)I + 2\mu(\theta)\mathbf{E}_e$$

Substituting Eq. 4-2 and Eq. 4-8 into $\mathbf{S} = \varsigma(\theta)\mathbf{S}_e$ of Eq. 4-5,

$$\mathbf{S} = \frac{1}{\varsigma(\theta)}(\lambda(\theta)(tr\mathbf{E})I + 2\mu(\theta)\mathbf{E}) - \frac{3}{2}\left(\varsigma(\theta) - \frac{1}{\varsigma(\theta)}\right)k(\theta)I$$

here, bulk modulus $k(\theta) = \lambda(\theta) + 2\mu(\theta)/3$.

If we adopt the following approximation for Eq. 4-6,

$$\varsigma(\theta) = 1 + a(\theta - \theta_0)$$

The expression of Eq. 4-9 can be simplified as,

$$\mathbf{S} = \lambda(\theta)(tr\mathbf{E})I + 2\mu(\theta)\mathbf{E} - 3\alpha k(\theta)(\theta - \theta_0)\mathbf{I}$$

By assuming Lame parameters λ and μ to be constants at various temperatures, $\mathbf{E}$ and $\mathbf{S}$ as the infinitesimal strain and the Cauchy stress, the stress can be represented in strain as in the following,

$$\sigma_{xx} = 2\mu\varepsilon_{xx} + \lambda\left(\varepsilon_{xx} + \varepsilon_{yy} + \varepsilon_{zz}\right) - 3ka(\theta - \theta_0)$$

$$\sigma_{yy} = 2\mu\varepsilon_{yy} + \lambda\left(\varepsilon_{xx} + \varepsilon_{yy} + \varepsilon_{zz}\right) - 3ka(\theta - \theta_0)$$

$$\sigma_{zz} = 2\mu\varepsilon_{zz} + \lambda\left(\varepsilon_{xx} + \varepsilon_{yy} + \varepsilon_{zz}\right) - 3ka(\theta - \theta_0)$$

$$\tau_{xy} = 2\mu\varepsilon_{xy}, \quad \tau_{yz} = 2\mu\varepsilon_{yz}, \quad \tau_{xz} = 2\mu\varepsilon_{xz}$$

Eq. 4-12

Where $\boldsymbol{\varepsilon}$ is the infinitesimal strain, $\boldsymbol{\sigma}$ is the Cauchy stress, $(\theta - \theta_0)$ is temperature difference with respect to initial temperature θ_0, E is the Young's modulus, v is the Poisson's ratio, and a is the constant linear coefficient of thermal expansion, with,

$$2\mu = \frac{E}{1+v}, \lambda = \frac{vE}{(1+v)(1-2v)}, \beta = 3ka = \frac{\alpha E}{1-2v} = \alpha(3\lambda + 2\mu)$$

Eq. 4-13

The strain $\boldsymbol{\varepsilon}$ can be further described by the displacement vector $\left(u_x, u_y, u_z\right)$ using Cauchy's infinitesimal strain at small deformation as,

$$\varepsilon_{xx} = \frac{\partial u_x}{\partial x}, \quad \varepsilon_{yy} = \frac{\partial u_y}{\partial y}, \quad \varepsilon_{zz} = \frac{\partial u_z}{\partial z}$$

$$2\varepsilon_{xy} = \frac{\partial u_x}{\partial y} + \frac{\partial u_y}{\partial x}, \quad 2\varepsilon_{yz} = \frac{\partial u_y}{\partial z} + \frac{\partial u_z}{\partial y}, \quad 2\varepsilon_{xz} = \frac{\partial u_x}{\partial z} + \frac{\partial u_z}{\partial x}$$

Eq. 4-14

Rewrite the constitutive strain-stress equations of Eq. 4-12 using Eq. 4-14,

$$\sigma_{ij} = \mu\left(u_{i,j} + u_{j,i}\right) + \lambda u_{k,k}\delta_{ij} - \beta(\theta - \theta_0)\delta_{ij}$$

Eq. 4-15

here, δ_{ij} is the Kronecker's symbol defined as,

$$\delta_{ij} = \begin{cases} 1 & for \ i = j \ , \\ 0 & for \ i \neq j \ , \end{cases}$$

<div align="right">Eq. 4-16</div>

4.1.2   Fourier bioheat transfer

Different from other continuum domain when subjected to thermal energy, soft tissue also features metabolic heat generation, blood perfusion, etc. Among related studies, Mitchell et al. [116] observed that the metabolic heat generation Q_{met} is a function of current tissue temperature and initial body temperature, given by,

$$Q_{met} = \ 0.17 \ \times \ 2^{(T-T_0)/10}$$

<div align="right">Eq. 4-17</div>

While in other researcher's work [19, 95], it is often assumed to be constant value distributed throughout the affected tissue body.

Using the term Q_{blo} to represent the heat removal produced by the flow of blood, one typical way is as shown in the following expression [117], whose effect is assumed homogeneously distributed along the tissue domain.

$$Q_{blo} = C_b \omega_b \rho_b (T_b - T)$$

<div align="right">Eq. 4-18</div>

where T_b stands for the arterial blood temperature which is taken as constant. The term also contains the density of blood ρ_b, the blood perfusion coefficient ω_b and the specific heat of blood C_b.

Besides, Q_{ext} is also designed to represent heat supply per unit volume within target tissue, e.g. for continuous point pattern heating sources, it can be expressed in the form [118],

$$Q_{ext} = P(t)\delta(x - x_0)\delta(y - y_0)\delta(z - z_0)$$

where $P(t)$ is the applied heat power per unit volume at time t on heating points, and δ equals 1 at location of heating points.

To estimate transient temperature field within heated soft tissues, here the Fourier's law of heat transfer equation is applied as derived in section 3.2, therefore Eq. 3-22 becomes,

$$\rho_0 C\dot{\theta} = \mathbf{k}_0 : (\mathbf{\nabla}_0 \otimes \mathbf{\nabla}_0)\theta + \frac{\partial \mathbf{k}_0}{\partial \theta} : (\mathbf{\nabla}_0 \theta \otimes \mathbf{\nabla}_0 \theta) + \theta \frac{\partial \mathbf{S}}{\partial \theta} : \dot{\mathbf{E}} + Q_{ext} + Q_{met} + Q_{blo}$$

Assuming density ρ_0, conductivity tensor $\mathbf{k}_0$ and specific heat tensor C to be constants, and $\mathbf{k}_0$ having the same values in all directions, then the second term on the right-hand side of Eq. 4-20 can be omitted. Incorporating with the assumption in Eq. 4-11, Eq. 4-12 and Eq. 4-14, and using $\boldsymbol{u}$ to denote the displacement vector, we have,

$$\frac{\partial \mathbf{S}}{\partial \theta} : \dot{\mathbf{E}} = -\beta \mathbf{\nabla} \cdot \dot{\boldsymbol{u}}$$

Then, the bioheat transfer equation can be described by a partial differential equation of the second order as followed,

$$\rho C\dot{T} + \beta T \mathbf{\nabla} \cdot \dot{\boldsymbol{u}} = k\mathbf{\nabla}^2 T + C_b \omega_b \rho_b (T_b - T) + Q_{met} + Q_{ext}$$

where T represents temperature at time t, which is also denoted as θ in the above deviations. The term $\beta T \mathbf{\nabla} \cdot \dot{\boldsymbol{u}}$ accounts for the mechanical energy involved in the

coupled process. In the present study the constant temperature T_0 is used to approximate current temperature T.

4.1.3 Non-rigid mechanics of motion

Appling the law of the non-rigid mechanics of motion, which can be written as,

$$\rho \ddot{u}_i = \sigma_{ij,j} + \rho b_i + F_i^{ext}$$

And substituting Eq. 4-15 into the above equation, one can derive the following,

$$\rho \ddot{u}_i = \left(\mu\left(u_{i,j} + u_{j,i}\right) + \lambda u_{k,k}\delta_{ij} - \beta(T - T_0)\delta_{ij}\right)_{,j} + \rho b_i + F_i^{ext}$$

Or,

$$\rho \ddot{\boldsymbol{u}} = \mu \boldsymbol{\nabla}^2 \boldsymbol{u} + (\lambda + \mu)\boldsymbol{\nabla} div\boldsymbol{u} - \beta \boldsymbol{\nabla}(T - T_0) + \rho \boldsymbol{b} + \boldsymbol{F}_{ext}$$

where $\boldsymbol{b}$ is the specific body force, $\boldsymbol{F}_{ext}$ is the external force.

Rewriting it in a three dimensional Cartesian coordinates, one has,

$$\frac{E}{2(1+v)}\left(\frac{\partial^2 u_x}{\partial x^2} + \frac{\partial^2 u_x}{\partial y^2} + \frac{\partial^2 u_x}{\partial z^2}\right) + \frac{E}{2(1+v)(1-2v)}\frac{\partial}{\partial x}\left(\frac{\partial u_x}{\partial x} + \frac{\partial u_y}{\partial y} + \frac{\partial u_z}{\partial z}\right)$$

$$- \frac{E\alpha}{1-2v}\frac{\partial(T - T_0)}{\partial x} + \rho b_x + F_x^{ext} = \rho \ddot{u}_x$$

$$\frac{E}{2(1+v)}\left(\frac{\partial^2 u_y}{\partial x^2} + \frac{\partial^2 u_y}{\partial y^2} + \frac{\partial^2 u_y}{\partial z^2}\right) + \frac{E}{2(1+v)(1-2v)}\frac{\partial}{\partial y}\left(\frac{\partial u_x}{\partial x} + \frac{\partial u_y}{\partial y} + \frac{\partial u_z}{\partial z}\right)$$

$$-\frac{E\alpha}{1-2v}\frac{\partial(T-T_0)}{\partial y} + \rho b_y + F_y^{ext} = \rho \ddot{u}_y$$

$$\frac{E}{2(1+v)}\left(\frac{\partial^2 u_z}{\partial x^2} + \frac{\partial^2 u_z}{\partial y^2} + \frac{\partial^2 u_z}{\partial z^2}\right) + \frac{E}{2(1+v)(1-2v)}\frac{\partial}{\partial z}\left(\frac{\partial u_x}{\partial x} + \frac{\partial u_y}{\partial y} + \frac{\partial u_z}{\partial z}\right)$$

$$-\frac{E\alpha}{1-2v}\frac{\partial(T-T_0)}{\partial z} + \rho b_z + F_z^{ext} = \rho \ddot{u}_z$$

<div align="right">Eq. 4-26</div>

4.2 Time integration

To maintain the stability of established simulation system under some large time steps, the implicit time integration scheme is adopted in this chapter to approximate the time derivatives involved in the governing equations where Δt is assumed to be constant,

$$\ddot{\boldsymbol{u}}^{t+\Delta t} = \frac{\dot{\boldsymbol{u}}^{t+\Delta t} - \dot{\boldsymbol{u}}^t}{\Delta t} = \frac{\frac{\boldsymbol{u}^{t+\Delta t} - \boldsymbol{u}^t}{\Delta t} - \frac{\boldsymbol{u}^t - \boldsymbol{u}^{t-\Delta t}}{\Delta t}}{\Delta t}$$

<div align="right">Eq. 4-27</div>

$$\dot{T}^{t+\Delta t} = \frac{T^{t+\Delta t} - T^t}{\Delta t}$$

<div align="right">Eq. 4-28</div>

Substituting Eq. 4-27 and Eq. 4-28 into Eq. 4-22 and Eq. 4-26, the following section gives further discretisation of the governing equations in space domain.

4.3 The finite difference method

In this section, for dealing with regular mesh volume, numerical method FDM is firstly selected to discretise the governing equations because of its maturity and efficiency in

dealing with regular volume meshes, as well as its flexibility on solving our principle equations without changing the mesh type.

For a cubic volume mesh, firstly the discretised bioheat conduction equation at point (i,j,k) can be described by referring to its neighbouring points (see Figure 7), as shown in Eq. 4-29 where Δx, Δy and Δz denote element length in three coordinate directions
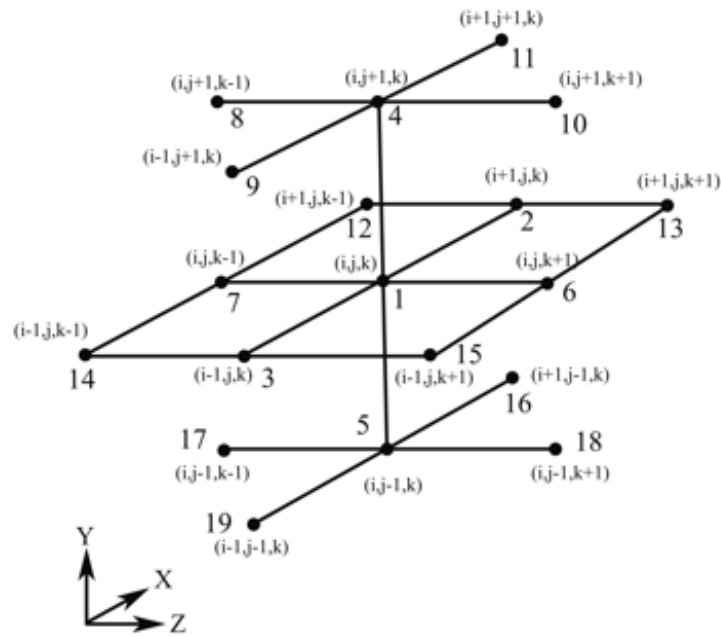
Figure 7: A cubic grid

$$\frac{\partial T}{\partial t}_{t+\Delta t} = \frac{T_{i,j,k,t+\Delta t} - T_{i,j,k,t}}{\Delta t} \quad , \quad \frac{\partial^2 T}{\partial x^2}_{t+\Delta t} = \frac{T_{i+1,j,k,t+\Delta t} + T_{i-1,j,k,t+\Delta t} - 2T_{i,j,k,t+\Delta t}}{\Delta x_i{}^2}$$

$$\frac{\partial^2 T}{\partial y^2}_{t+\Delta t} = \frac{T_{i,j+1,k,t+\Delta t} + T_{i,j-1,k,t+\Delta t} - 2T_{i,j,k,t+\Delta t}}{\Delta y_i{}^2}$$

$$\frac{\partial^2 T}{\partial z^2}_{t+\Delta t} = \frac{T_{i,j,k+1,t+\Delta t} + T_{i,j,k-1,t+\Delta t} - 2T_{i,j,k,t+\Delta t}}{\Delta z_i^{\,2}}$$

$$\boldsymbol{\nabla} \cdot \dot{\boldsymbol{u}} = \frac{u_{x\,i+1,j,k,t+\Delta t} - u_{x\,i,j,k,t+\Delta t} - u_{x\,i+1,j,k,t} + u_{x\,i,j,k,t}}{\Delta x_i \Delta t}$$

$$+ \frac{u_{y\,i,j+1,k,t+\Delta t} - u_{y\,i,j,k,t+\Delta t} - u_{y\,i,j+1,k,t} + u_{y\,i,j,k,t}}{\Delta y_j \Delta t}$$

$$+ \frac{u_{z\,i,j+1,k,t+\Delta t} - u_{z\,i,j,k,t+\Delta t} - u_{z\,i,j+1,k,t} + u_{z\,i,j,k,t}}{\Delta z_k \Delta t}$$

Similarly, the discretised non-rigid motion equation at point (i,j,k) can also be described using its neighbouring points (see Figure 7). For example, the discretisation process for the first equilibrium of Eq. 4-26 that covers the displacement calculation of target point in the x-axis direction is described as follows:

$$\frac{\partial T}{\partial x}_{t+\Delta t} = \frac{T_{i+1,j,k,t+\Delta t} - T_{i-1,j,k,t+\Delta t}}{2\Delta x_i}$$

$$\frac{\partial^2 u_x}{\partial x^2}_{t+\Delta t} = \frac{u_{x\,i+1,j,k,t+\Delta t} + u_{x\,i-1,j,k,t+\Delta t} - 2u_{x\,i,j,k,t+\Delta t}}{\Delta x_i^{\,2}}$$

$$\frac{\partial^2 u_x}{\partial y^2}_{t+\Delta t} = \frac{u_{x\,i,j+1,k,t+\Delta t} + u_{x\,i,j-1,k,t+\Delta t} - 2u_{x\,i,j,k,t+\Delta t}}{\Delta y_j^{\,2}}$$

$$\frac{\partial^2 u_x}{\partial z^2}_{t+\Delta t} = \frac{u_{x\,i,j,k+1,t+\Delta t} + u_{x\,i,j,k-1,t+\Delta t} - 2u_{x\,i,j,k,t+\Delta t}}{\Delta z_k^{\,2}}$$

$$\frac{\partial}{\partial x}\left(\frac{\partial u_y}{\partial y}\right)_{t+\Delta t}$$

$$= \frac{u_{y\,i+1,j+1,k,t+\Delta t} - u_{y\,i+1,j-1,k,t+\Delta t} - u_{y\,i-1,j+1,k,t+\Delta t} + u_{y\,i-1,j-1,k,t+\Delta t}}{4\Delta x_i \Delta y_j}$$

$$\frac{\partial}{\partial x}\left(\frac{\partial u_z}{\partial z}\right)_{t+\Delta t}$$

$$= \frac{u_{z\,i+1,j,k+1,t+\Delta t} - u_{z\,i+1,j,k-1,t+\Delta t} - u_{z\,i-1,j,k+1,t+\Delta t} + u_{z\,i-1,j,k-1,t+\Delta t}}{4\Delta x_i \Delta z_k}$$

<div align="right">Eq. 4-30</div>

Applying the time domain discretisations in Eq. 4-27 and Eq. 4-28 and assembling the space domain discretisation in Eq. 4-30 in each axis direction, temperature and displacement of all inner points at the end of every time step could be expressed accordingly. The final matrix form of these equations for all included mesh points using FDM method, is like,

$$\boldsymbol{M}\left(\frac{\underline{\boldsymbol{u}}_{t+\Delta t} - 2\underline{\boldsymbol{u}}_t + \underline{\boldsymbol{u}}_{t-\Delta t}}{\Delta t^2}\right) + \boldsymbol{C}\left(\frac{\underline{\boldsymbol{u}}_{t+\Delta t} - \underline{\boldsymbol{u}}_{t-\Delta t}}{2\Delta t}\right) + \boldsymbol{K}\underline{\boldsymbol{u}}_{t+\Delta t} = \boldsymbol{F}_{t+\Delta t}$$

$$\underline{\boldsymbol{u}} = \begin{Bmatrix} \theta \\ \boldsymbol{u} \end{Bmatrix}$$

<div align="right">Eq. 4-31</div>

where $\boldsymbol{M}$ is the global mass matrix, $\boldsymbol{C}$ is the global damping matrix, $\underline{\boldsymbol{u}}$ is the combined temperature and displacement vector, $\boldsymbol{K}$ is the stiffness matrix, Δt is the time step, and $\boldsymbol{F}$ is the total external force.

4.4 Convergence testing

For the Gauss-Seidel solution of the global matrix, the maximum number of iterations should be defined to avoid an infinite loop. However, specifying some margin of error to terminate iteration loops before reaching the maximum number of iterations can result in a reduction of computation cost.

Figure 8 shows the number of Gauss-Seidel solver iterations against the margin of error for a typical simulation of thermal mechanical interaction using FDM method. From which we can see that, smaller margins of error allow for greater accuracy of computation results, however it requires a larger number of solver iterations. Meanwhile, if the margin of error is too large, convergence may not occur due to accrued error during successive simulation iterations. But if the margin of error is too small, the maximum number of solver iterations may be reached before reaching satisfactory convergence level.
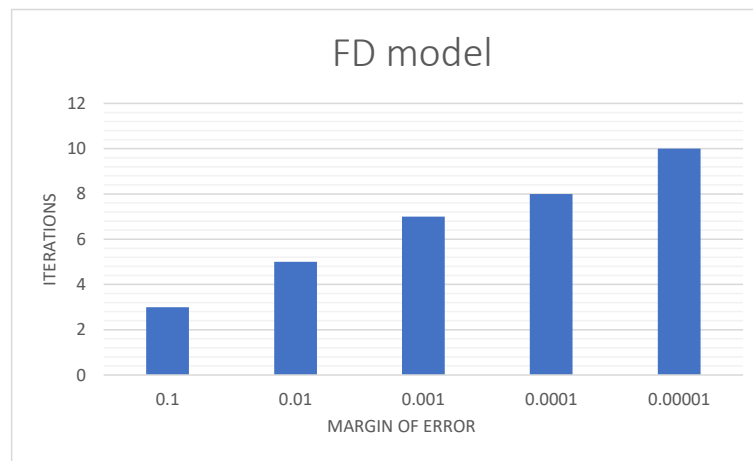
Figure 8: Number of iterations vs. margin of error for FD model

4.5   Implementation and results

In this section, a prototype system has been implemented based on the above proposed model and discretisation methods FDM. In order to evaluate the performance of such a system, trials are conducted in terms of a cubic-shape soft tissue model in the size of 10mm×10mm×10mm, which is meshed up using 1000 cubic elements with 1331 nodes, as shown in Figure 9. Under purely thermal loading condition, the needle shape heating device as used in a typical thermal ablation application is modelled as a line, with five

evenly spaced points as heat sources (the first one is located at the tip of the needle), for generating heat energy. As illustrated in Figure 10 the needle is positioned in a way that the middle of five heating points is located at the centre of the cubic-shape tissue model. It generates thermal energy through each of the five heating points at $0.08\,W$ to heat up the tissue. Also, a series of observation points: P_1 (x=0.005m, y=0.005m, z=0.005m), P_2 (x=0.006m, y=0.005m, z=0.005m), P_3 (x=0.007m, y=0.005m, z=0.005m), P_4 (x=0.008m, y=0.005m, z=0.005m), P_5 (x=0.009m, y=0.005m, z=0.005m) and P_6 (x=0.01m, y=0.005m, z=0.005m), as shown in Figure 10, are chosen to analyse soft tissue's behaviour under designed simulation conditions. The selected reference values include the tissue properties and parameters are shown in Table 2.
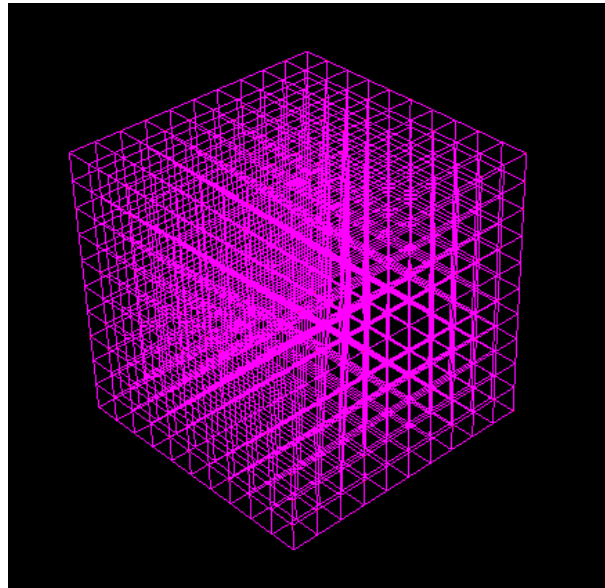
Figure 9: Meshing of cubic-shape tissue model using cubic elements
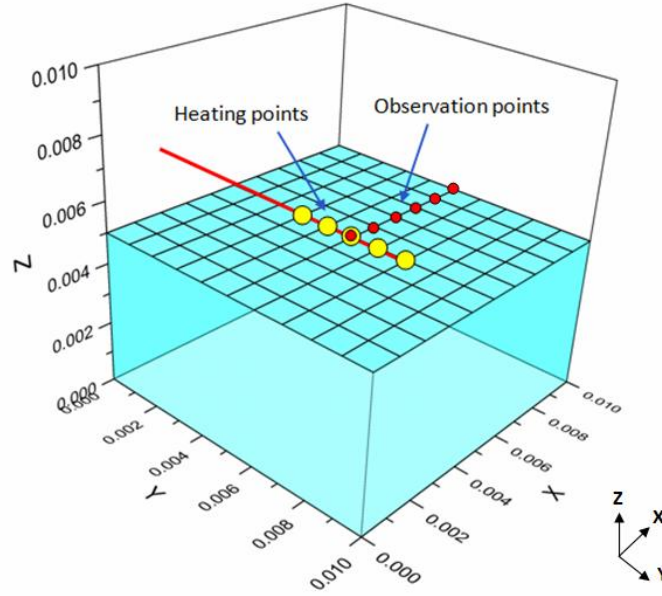
Figure 10: The Y-axis half section view of heating and observation points inside tissue model

Table 2: Tissue parameters and constants

Parameters	Value
Thermal conductivity k; W/mK	0.613
Specific heat C; J/kgK	4192
Thermal expansion coefficient α; 1/℃	3×10^{-4}
Density ρ; kg/m^3	1000
Blood perfusion rate ω_b; kg/(m^{3}s)	0.5
Arterial temperature T_b; K	310
Metabolic heat generation rate Q_m; W/m^3	33800
Blood specific heat C_b; J/kgK	3600
Young's modulus E; Pa	10.2×10^6
Poisson's ratio v;	0.35

4.5.1 Boundary conditions

To solve established governing equations, it is necessary to determine the boundary conditions under consideration. Here, for (a) Thermal, the Dirichlet boundary condition is chosen to determine the character of heat interchange over the boundary, i.e. the specified temperature on the boundaries is set to be 310 K. (b) Elastic, fixed conditions

47

is set at the tissue model surfaces, so that all boundaries cannot move freely. For the initial condition at $t = 0$ s, we assume $T_0 = 310$ K, and no strain inside the tissue model before applying heat.

4.5.2   Temperature distribution

Figure 11 shows the temperature changes at the five heating source points, P_1-P_5, where thermal energy is directly applied for duration of 120s. It can be seen that the increase rate of temperature is different at the initial stage and afterwards. Temperature is increasing rapidly initially, while afterwards, no significant change is observed until the end of simulation time, although heating is continuously applied within this period. For the spatial temperature distribution, Figure 12 shows that final temperatures at selected points, P_1-P_6 with respective distances from the centre of heating source of 0m, 0.001m, 0.002m, 0.003m, 0.004m and 0.005m, respectively, are descending from 367K to 310K after 120 seconds of thermal interaction. Combining Figure 11 and Figure 12, gives how heat energy is distributed within the heated tissue, that is the temperature at the heating centre is much higher compared with other surrounding points, while the changing rate reduces both spatially and temporally.
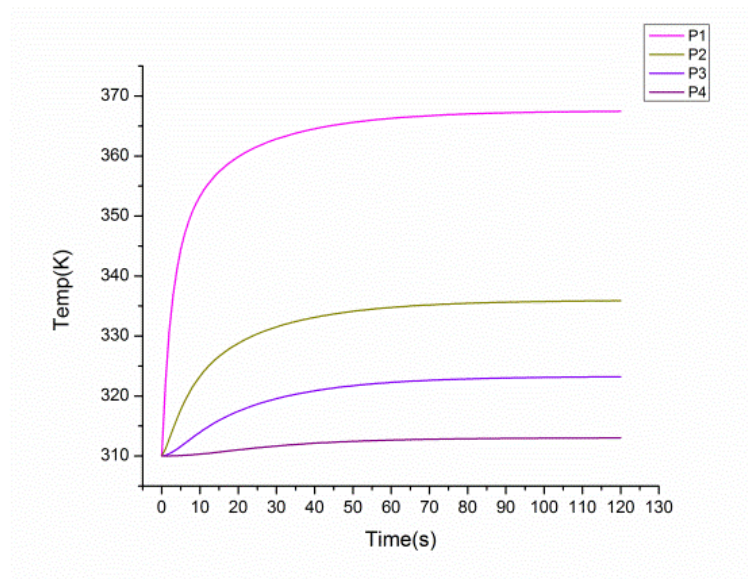
Figure 11: Temperature at the heating source points
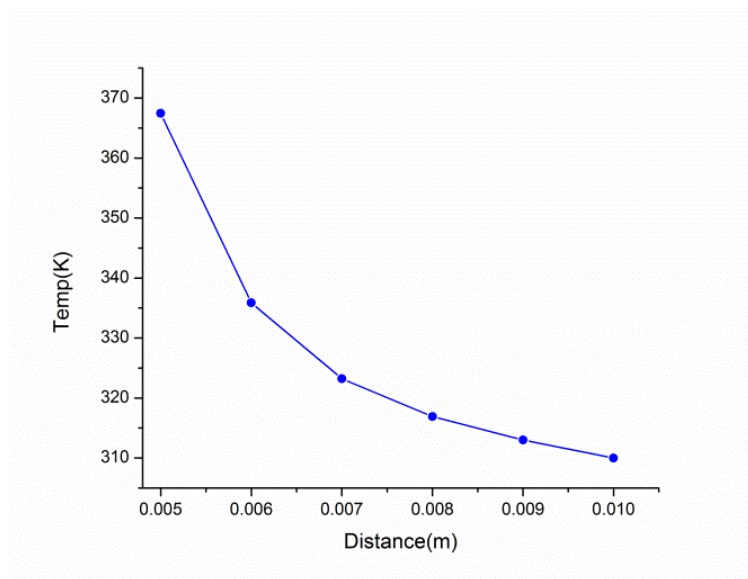
Figure 12: Temperature vs. distance curve at 120 s

4.5.3 Displacement distribution

Figure 13 left gives the displacement of plane x=0.001m at the end simulation time of

120s, Figure 13 right shows the displacement of its symmetric plane x=0.009m with

respect to a mid-plane of the cubic-shape model. Considering the position and distribution of heating sources, every two selected symmetric planes with regard to a mid-plane across the centre of heating line deform outward symmetrically as expected, see Figure 14 and Figure 15. It also has to be mentioned that the distance from these planes to the centre of heating area is chosen to be the same: 0.004m.
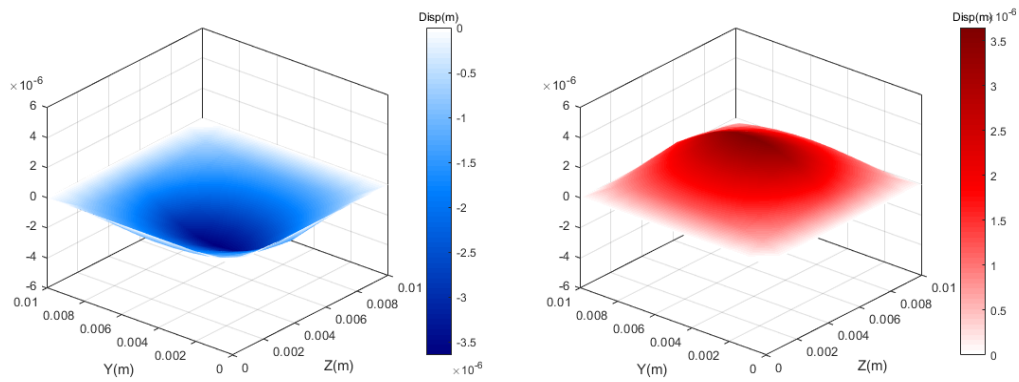
Figure 13: X-axis displacement at plane X=0.001m and X=0.009m at 120 s
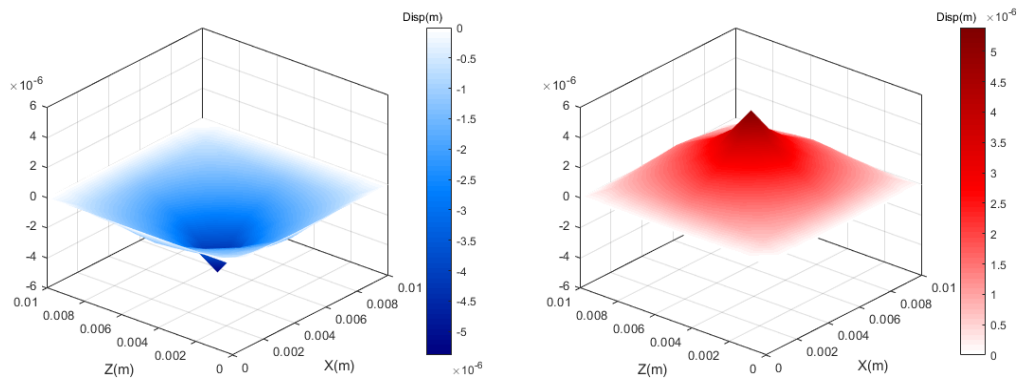
Figure 14: Y-axis displacement at plane Y=0.001m and Y=0.009m at 120 s
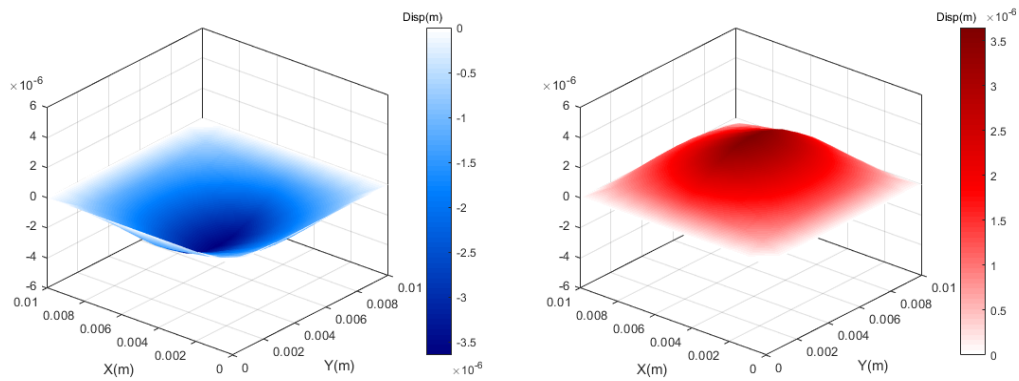
Figure 15: Z-axis displacement at plane Z=0.001m and Z=0.009m at 120s

Figure 16 and Figure 17 show a close look of the thermally induced mechanical deformations with respect to temperature change, at a series of points within the deformed tissue model: P_1 to P_4. By tracing the displacement of point P_2, as shown in Figure 16, it can be seen that both of its y and z-axis displacements are equal to zero. Similarly, there would be no y and z-axis displacement for points P_2-P_4. Thus, only x-axis displacements change of these four points are concerned next. Within the time range of 0 to 120 seconds, curves representing three different points P_2-P_4 in Figure 17 show quite similar changing trend while the heating centre P_1 stays still considering it is the centre of heating sources and the cubic-shape tissue model. Basically, the point located farthest from the centre of heating sources had smallest deformation. However, comparing with other two points (P_2, P_4) that located all further away from the heating centre P_1, displacement of P_3 surprisingly becomes larger and larger than P_2. To explain these, one has to refer to Figure 18, which plots displacement and temperature variations of five selected observation points (P_1-P_6) that located from 0 to 0.01m away from the heating centre (see Figure 10) at three selected heating duration of 10s, 50s and 120s. From which we can get that as the heat continually applied, the displacement peak along selected observation line moves from P_2 to P_3.

51
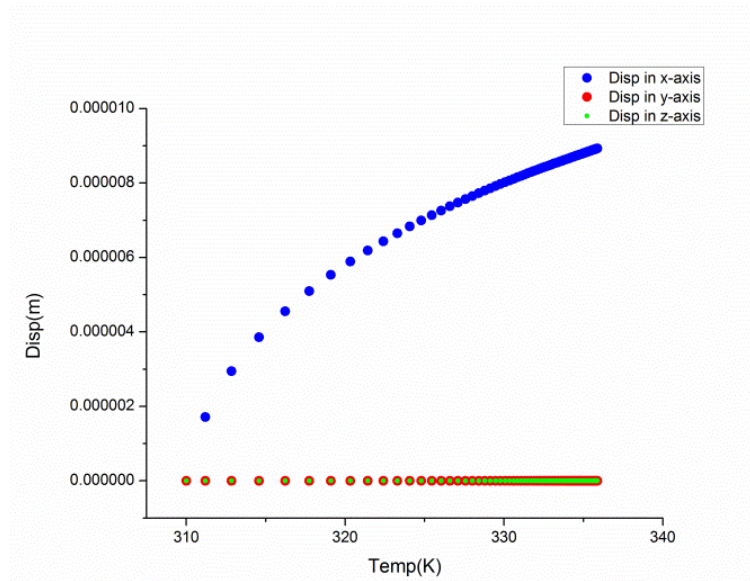
Figure 16: Displacement vs. temperature curves at point P_2 (0.006m, 0.005m, 0.005m)
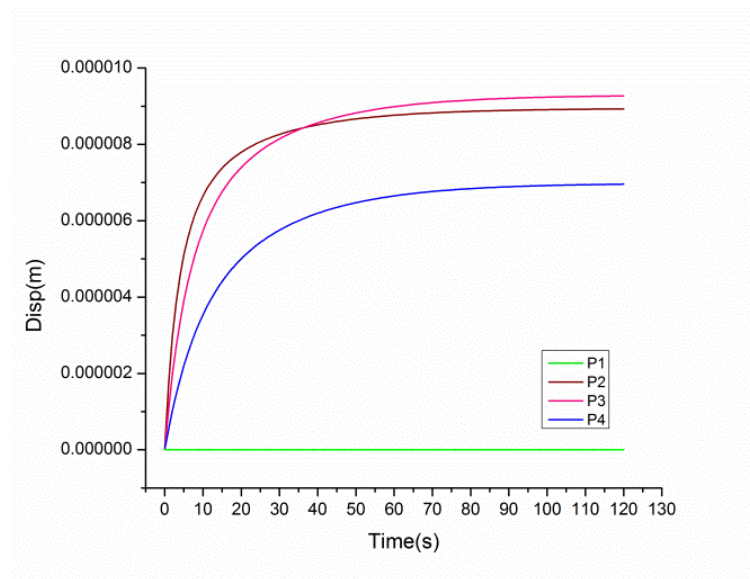
Figure 17: Displacement vs. time curves at observation points P_1, P_2, P_3 and P_4
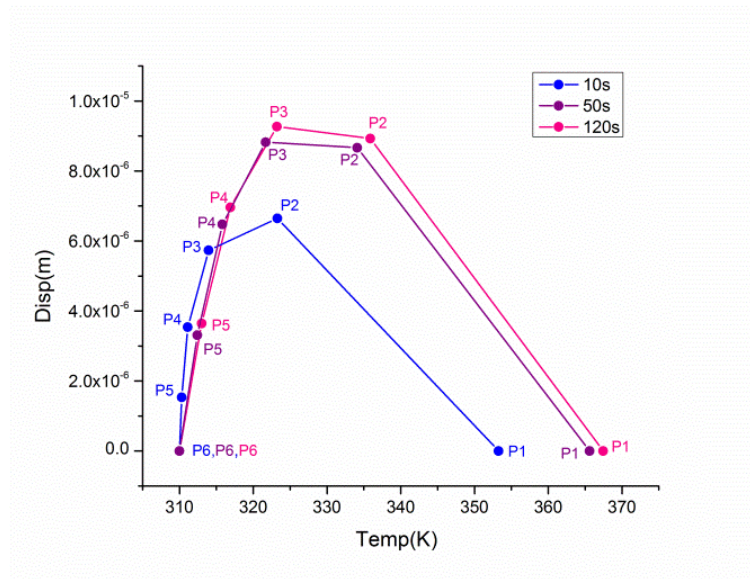
Figure 18: Displacement vs. temperature curves at different time points

4.5.4 Strain distribution

To analysis the strain distribution based on resultant displacement distribution, strain ε_{xx} is specially studied at selected observation points P_1-P_4. Strain vs. heating duration curves at these points are as plotted in Figure 19, it can be seen that, the strain increase rate for all points are relatively large at the beginning of heating, similar as the profiles of temperature and displacement over the same time range. Positive strain is only observed at points P_1 and P_2 near the heating centre, while negative strain happens at P_3 and P_4 close to fixed boundary surface. Meanwhile, the positive and negative strain can also be interpreted as soft tissue expansion and shrinkage, respectively. By comparing the magnitude of observed strain curves, it can be concluded that towards the end of simulation, for points located near the heating centre P_1 is influenced more severely by temperature distribution than P_2, while for points located near the constrained boundaries P_4 is influenced more severely than P_3.

53
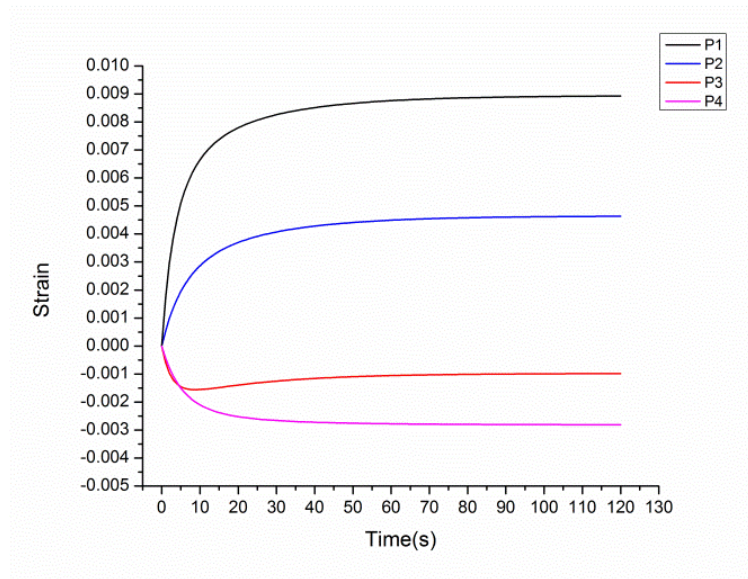
Figure 19: Strain vs. time curves at observation points P_1, P_2, P_3 and P_4

4.6   Conclusion

Following the formulation of constitutive theory in the thermodynamic framework using the method of multiplicative decomposition of thermal mechanical deformation gradient, as conducted in Chapter 3, in this Chapter, the next step of formulation is focused on the features of target soft tissues. It is assumed that the tissue body is elastically and thermally isotropic material and obeys Fourier's law of heat transfer theory, and also has metabolic heat generation and embedded blood vessel perfusion. The formulated constitutive and bioheat transfer equations are then combined with law of non-rigid mechanics of motion to establish our proposed thermal mechanical soft tissue model. The numerical method FDM and implicit time integration scheme are utilized to construct the proposed model into a computer program. Simulation tests have also been performed to analyse the thermal and mechanical responses of purely thermal heated soft tissue during thermal ablation. Based on our considered boundary conditions, the results demonstrate that, thermally, the tissue near the heating sources

54

is influenced more severely than the tissue located further away, while the changing rate reduces both spatially and temporally. However mechanically, as the heat is continually applied the displacement peak among heated tissue moves along the heat propagation direction. Further, soft tissue expansion and shrinkage are explained by positive and negative strain observed during our simulation. Theoretically, these simulation results can also be used as theoretical basis for better understanding of the physical observations during real life thermal ablation applications.

5 Prediction of tissue thermal mechanical damage

As an effective alternative of traditional tissue cancer treatments, thermal ablation has the advantages of minimally invasive, shortened recovery time, and controlled side effect to surrounding healthy tissues. The success of this therapy requires highly accurate characterization of tissue damage under thermal and mechanical loads. Currently, most of the existing studies only rely on thermal-induced temperature elevation to predict tissue damage area, ignoring the effect of tissue deformation during this procedure [19, 95, 98, 99]. However, even a relatively small variation in thermally and/or mechanically induced tissue deformation can lead to various effects such as altered production of hormones, suppressed immune response, and protein denaturation [119]. Investigation also shows that the Arrhenius burn integration is the most commonly used model to describe tissue thermal damage in literature [28, 57, 120]. However, in such a chemical rate based damage model, the thermal mechanical effect due to thermal variation and/or external force is often ignored. In fact, such an influence may affect the barrier (energy level) to unfolding protein from a relative native state to a transition state [15, 121], leading to further or the reverse damage to biological tissues. Therefore, it is an absolute necessity to take this effect into account to accurately characterize tissue damage during thermal ablation.

In Chapter 4, we have presented a method to characterize the thermal-induced mechanical behaviours of soft tissues relying on the method of multiplicative decomposition of thermal mechanical deformation gradient. In this Chapter, the issue of tissue thermal-mechanical damage will be further studied based on this model and

using an alternative damage prediction method by taking into account of the thermal mechanical effect.

5.1   The effect of force upon denaturation of protein

As aforementioned, extracellular matrix is the main load-carrying element in a wide variety of soft tissues and it provides structural integrity. As a major constituent of extracellular matrix, collagen is a rather stiff and hard protein. The collagen molecule has a triple-helical structure, where the helices are linked together through hydrogen bonds [121], see Figure 20. Basically, denaturation of the protein molecule happens when the hydrogen bonds break resulting from either high temperature or external force.
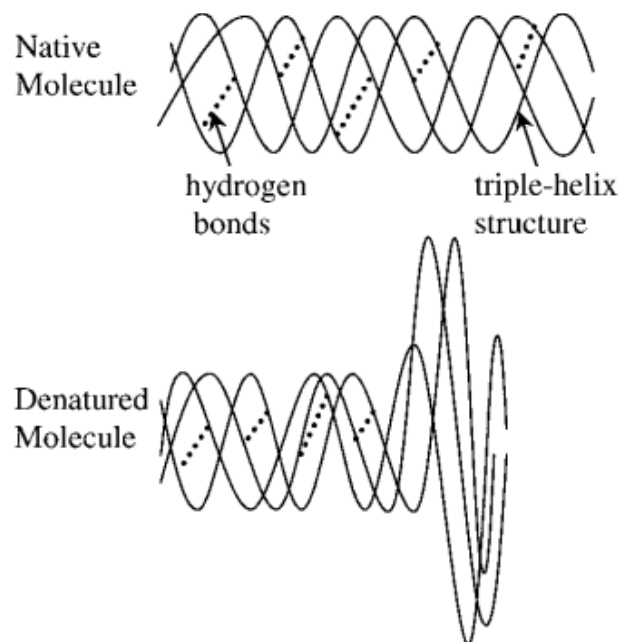
Figure 20: Native and denatured states of collagen molecule (Stylianopoulos et al. [121])

As illustrated in Figure 21, in a conventional two state free energy model of protein folding, the collagen has two configurations (folded and unfolded) exchanging via a

high energy transition state. There are two energy levels with native (folded) being at lower energy level, which is thermodynamically favorable at physiological temperatures. At zero force condition, the energy barrier between native and transition state is defined as the activation Gibbs free energy $\Delta \boldsymbol{G}_{TS-N}$, and energy barrier between denatured and transition state defined as $\Delta \boldsymbol{G}_{TS-D}$.

Under external force, as with any protein denaturation (defined as k), the energy barrier between native and transition state is lowered providing energy is imparted to the system through external mechanical work [15, 121]. In detail as shown in Eq. 5-1 to Eq. 5-4, the tensile force $\boldsymbol{F}$ applied on the molecule destabilises the native state by contribution of $\boldsymbol{F}x_u$. Meanwhile, the denatured state is stablised by the force with a contribution of $\boldsymbol{F}x_f$. Here x_u and x_f is the observed distance along the axis of applied force to the transition state for mechanical unfolding and refolding pathway.

$$k_u^0 = Aexp\left(-\frac{\Delta \boldsymbol{G}_{TS-N}}{k_B T}\right)$$

$$k_f^0 = Aexp\left(-\frac{\Delta \boldsymbol{G}_{TS-D}}{k_B T}\right)$$

$$k_u(F) = Aexp\left(-\frac{\Delta \boldsymbol{G}_{TS-N} - \boldsymbol{F}x_u}{k_B T}\right) = k_u^0 exp\left(\frac{\boldsymbol{F}x_u}{k_B T}\right)$$

$$k_f(F) = Aexp\left(-\frac{\Delta \boldsymbol{G}_{TS-D} + \boldsymbol{F}x_f}{k_B T}\right) = k_f^0 exp\left(\frac{-\boldsymbol{F}x_f}{k_B T}\right)$$

where A is the frequency factor, k_B is Boltzmann's constant, T is temperature in Kelvin, $\Delta \mathbf{\textit{G}}_{TS-N}$ and $\Delta \mathbf{\textit{G}}_{TS-D}$ are the activation energy for unfolding and refolding.
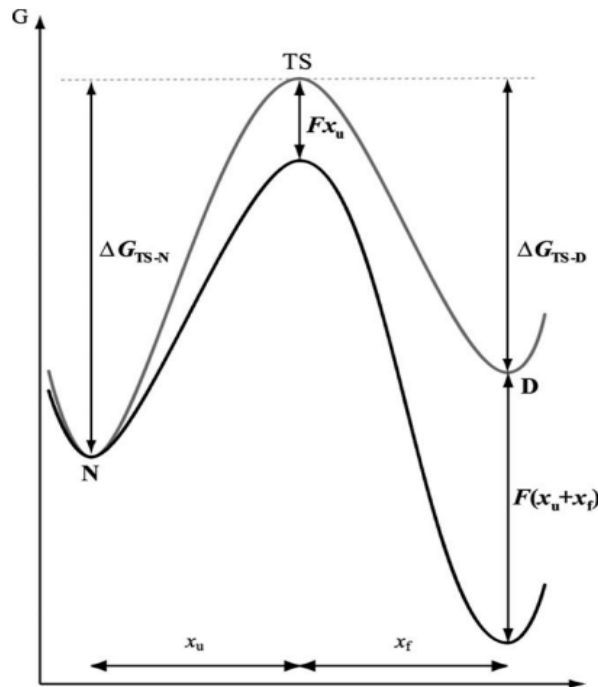
Figure 21: Two state free energy, transition state (TS) and denatured state (D) relative to native state (N). Grey represents zero force situation and black for landscape under applied force. (Rounsevell et al. [12])

5.2   Thermal-mechanical damage model

Soft tissues endure thermal stress and deformation due to temperature variation and/or external force. As proteins in tissues can be denatured at relatively small activation energy due to energy imparted to the system through external mechanical work, it is reasonable to conclude that biological tissues are more easily to be damaged or the reverse under deformation, no matter such deformation is induced by temperature variation or external force. This indicates both thermally and mechanically stored strain energy through deformation affects proteins to overcome the barrier from a relative native state to a transition state during any denaturation.

59

Based on the description in the above section where the tensile force applied on the target molecule destabilizes the native state by contribution of mechanical work, this chapter incorporates thermally and mechanically induced strain energy into the traditional tissue damage model of Arrhenius integration to characterize tissue thermal damage. Focusing on the unfolding rate contribution during protein denaturation process as expressed in Eq. 5-3, Shen et al. has proposed a thermal mechanical tissue damage model by replacing the term $\boldsymbol{F}x_u$ with E_T as follows [7], as has been expressed in Eq. 2-3,

$$\Omega = A \int_0^t exp\left(-\frac{\Delta E - E_T}{RT}\right) dt$$

where A is a material parameter (frequency factor or damage rate factor), ΔE is the activation energy, R is the universal gas constant, and t is the exposure time at a given temperature T. E_T is the stored strain energy by thermal loading, which is further represented by Eq. 5-6, where V_{mol} stands for the molar volume of target tissue.

$$E_T = \frac{1}{2}V_{mol}\sigma_{ij}\varepsilon_{ij}$$

Different from Eq. 5-5 [7], instead of using stored energy as calculated by Eq. 4-12 and Eq. 4-14 in Chapter 4, the stress expression is readjusted by taking out the thermal strain terms $3ka(\theta - \theta_0)$ in Eq. 4-12, considering only stored strain energy based on resultant tissue deformation is the key influence factor of our proposed model, the modified damage model as expressed in Eq. 5-7. The improvement of proposed thermal mechanical damage prediction model also lies in the fact that, the purely mechanically

induced strain energy term as included by Stylianopoulos et al. in [121] and the purely thermally induced strain energy term as introduced by Shen et al. in [7] in the damage model, is replaced with both thermally and mechanically induced strain energy term $\acute{E}_{TM}$ calculated from the resultant tissue deformation. The proposed model is expressed in the following form,

$$\Omega = A \int\limits_{0}^{t} exp\left(-\frac{\Delta E - \acute{E}_{TM}}{RT}\right) dt$$

Generally, it is more suitable for dealing with complex situations like combined thermal and mechanical loading during thermal ablation application. Besides the following implementation under purely thermal loads, other detailed implementation based on proposed thermal mechanical damage model under thermal and mechanical loads will be further described in Chapter 7.

5.3   Implementation

Simulations are conducted to investigate the performance of presented thermal mechanical damage model based on the same simulation conditions and input tissue sample as mentioned in Chapter 3 (see Figure 8 and 9). For the comparison analysis purpose, two different types of tissue samples (see Table 3) are used in this section to identify the influence of thermal mechanical interaction on tissue damage prediction. Other parameters used in our simulation tests are as shown in Table 2 and Table 4.

Table 3: Tissue type

Soft tissue type	Young's modulus (Pa)	Poisson's ratio
Type I	10.2×10^6	0.35
Type II	120×10^6	0.49

Table 4: Arrhenius parameters

Parameters	Value
Activation energy ΔE; J/mol	667000
Frequency factor A; 1/s	1.98×10^{106}
Gas constant R; J/(molK)	8.314
Molar volume V_{mol}; m^3/mol	0.285

To study strain energy distribution within thermal treated tissue as a result of temperature variation, analysis has been conducted at plane Y=0.005m. Figure 22 shows the distribution of strain energy at this plane at simulation time: 10s and the end of simulation: 120s for type I tissue, while Figure 23 shows corresponding distributions for type II tissue. It is observed that the point located at the centre of selected plane encounters the maximum strain energy, with the value of 1625.18 J/m^3 and 3091.80 J/m^3 for type I tissue at 10s and 120s, and the value of 841464.90 J/m^3 and 1465832.67 J/m^3 for type II tissue at 10s and 120s. It can be concluded that, for the same type of soft tissue, the magnitude of generated strain energy at 10s and 120s are basically within the same order, while larger value of strain energy happens at longer duration of heating. But for different type of tissue samples, it is demonstrated that type II tissue has an increase of stored strain energy with orders of magnitude than type I tissue.
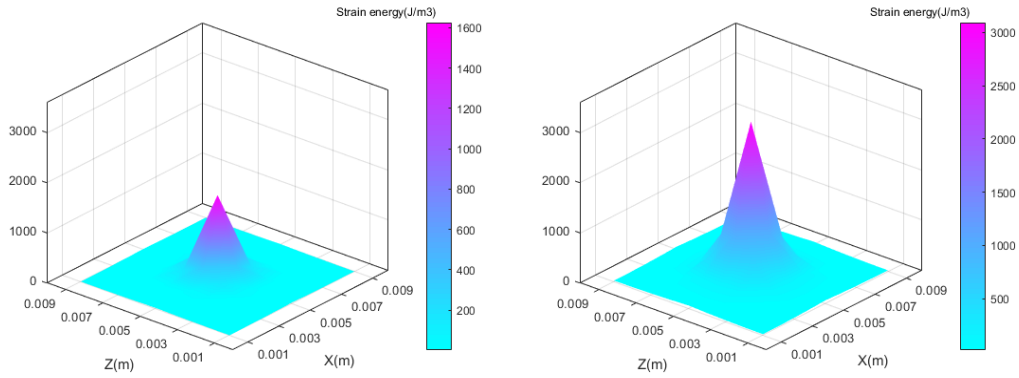
Figure 22: Strain energy comparison at time 10s and 120s for type I tissue
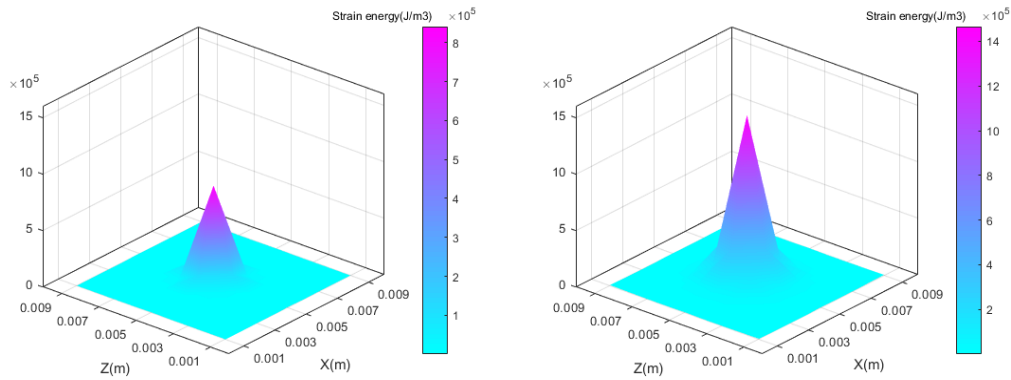
Figure 23: Strain energy comparison at time 10s and 120s for type II tissue

By referring to the activation energy ΔE, as listed in the thermal mechanical damage prediction model, such an influence of tissue deformation on damage prediction may be remarkable as strain energy $\hat{E}_{TM}$ is becoming comparable to ΔE. Assuming tissue damage $\Omega = 1$ [3] is the target damage state, comparison of the ablation zone based on thermal and thermal mechanical damage prediction models are as illustrated in Figure 24 and Figure 25 for tissue type I, Figure 26 and Figure 27 for tissue type II. It can be seen that for prediction model that considering tissue deformation, the tissue endures a higher level of damage. Meanwhile, the resultant damage field follows the profile of

63

temperature distribution, with decreasing rate becoming smaller along the heat propagating direction. Specially, for tissue type I, the deviation of ablation zone between two damage prediction models is relatively small for both 10s and 120s of heating. But for tissue type II, the deviation is remarkable especially for short duration of thermal treatment. Such a observation is also consistent with the discussion that the prediction deviation may be remarkable as strain energy $\acute{E}_{TM}$ is becoming comparable to ΔE, since for the boundary tissues at the section plane of damage using threshold $\Omega = 1$, the only comparable $\acute{E}_{TM}$ is observed for tissue type II at 10s of heating, as illustrated by comparing Figure 23 left with Figure 27 left.
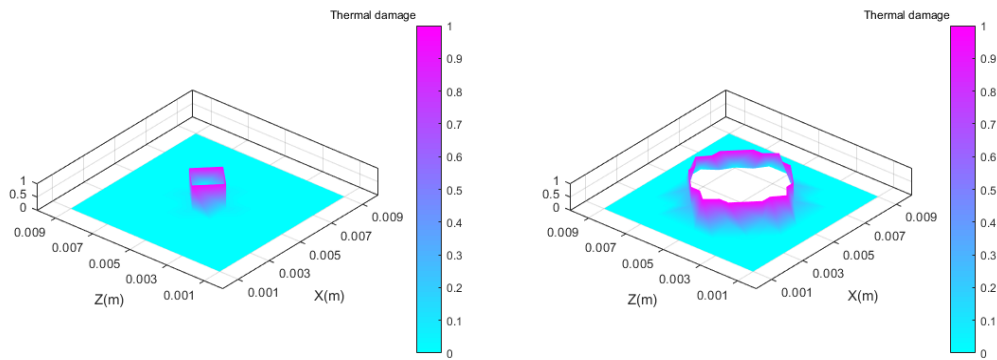
Figure 24: Thermal damage comparison at time 10s (left) and 120s (right) for type I tissue
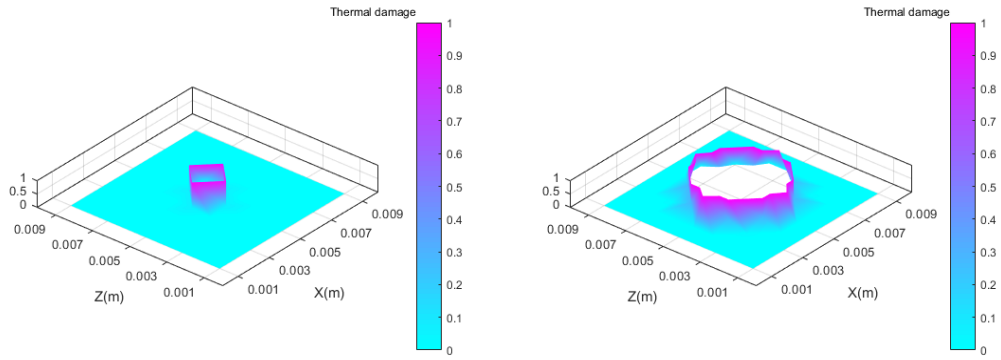
Figure 25: Thermal mechanical damage comparison at time 10s (left) and 120s (right) for type I tissue
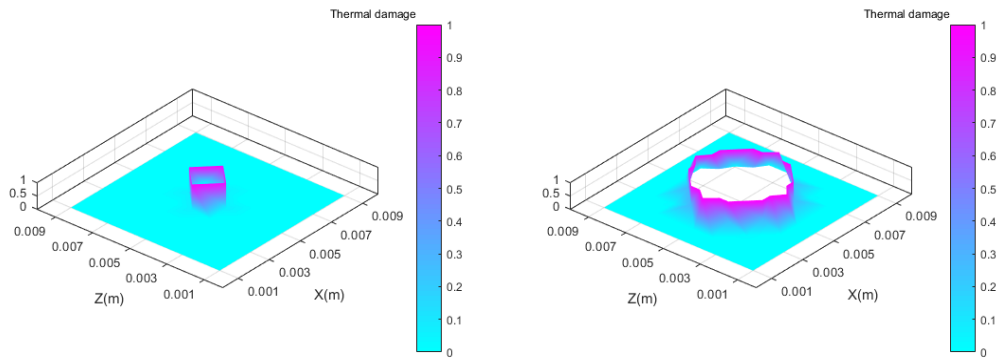
Figure 26: Thermal damage comparison at time 10s (left) and 120s (right) for type II tissue
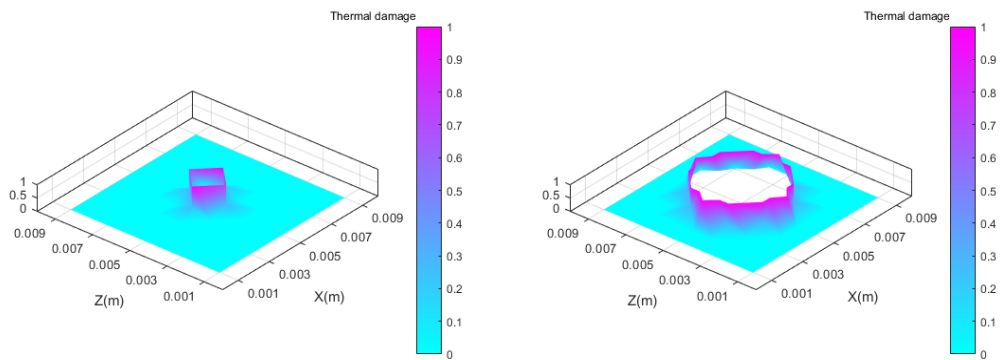
Figure 27: Thermal mechanical damage comparison at time 10s (left) and 120s (right) for type II tissue

5.4 Conclusion

As with any protein denaturation, the energy barrier to unfolding protein from a relative native state to a transition state is affected providing energy is imparted to the system, it inspires us that both thermally and mechanically stored strain energy caused by tissue deformation can affect the energy barrier between native and transition state, leading to further or the reverse damage to treated biological tissues. Therefore, it is an absolute necessity to take this effect into account to accurately characterize tissue damage during thermal ablation. This chapter presents such a method by incorporating tissue deformation into the traditional damage model of Arrhenius integration. Still employing the established Fourier thermal mechanical model in Chapter 4 to describe soft tissues' thermal-mechanical behaviours under purely thermal load and using the numerical method of FDM to solve corresponding governing equations, further simulations are performed in this Chapter to analysis established damage model. Comparison analysis for models with and without considering tissue deformation demonstrates that the presented method can account for tissue thermal damage more effectively than the method without considering tissue deformation. Depending on the tissue parameters used, such a deviation against traditional thermal damage model can be remarkable, and the deviation of predicted ablation zone considering tissue deformation is no longer non-negligible, especially for short duration of thermal ablation. In practice, these findings may provide a more reliable guideline for relevant surgeons to control the tissue damage zone during thermal ablation procedure.

6   Non-Fourier based thermal mechanical model using FEM

Currently, the existing tissue-thermal energy interaction models are mainly established based on the Fourier bioheat transfer theory [44, 94, 122]. However, the Fourier bioheat transfer theory assumes an infinite speed of heat propagation in the target material, which does not correspond to a real-world situation. On the other hand, a possible non-Fourier bioheat transfer theory disregards this assumption, and depicts that a local change in temperature cannot cause perturbation in temperature at all points in the medium instantaneously. In other words, thermal behaviour in non-homogenous media needs a relaxation time or characteristic time to accumulate enough energy to transfer to the nearest elements. In a microscopic point of view, the necessity of a finite speed of heat propagation has also been demonstrated in [123], and such non-Fourier thermal behaviour in biological tissues has also been experimentally observed in literature [23, 24, 50, 124].

In this chapter, the author focused on building a more generalized model for our target problem, by considering more relevant aspects during thermal ablation process such as: 1) more complex irregular volume meshes will be accounted; 2) a non-classical bioheat transfer model will be presented, which noting the relaxing of heat flux in classical Fourier bioheat transfer equation, characterized by a thermal characteristic (relaxation) time. Shortly, proposed model in this chapter is a more generalized model, as it includes more general aspects in practice that may affect final thermal damage predicting in soft tissue ablation.

Meanwhile, comparison analysis between Fourier and non-Fourier based thermal mechanical models is performed in this chapter, and the established thermal

mechanical damage model in Chapter 5 is also included in this chapter for further comparison of these two models.

6.1 Non-Fourier bioheat transfer

As mentioned in Chapter 4, the Fourier based bioheat transfer equation [44] can be described as following,

$$\rho C \frac{\partial T}{\partial t} + \beta T_0 \frac{\partial (\mathbf{\nabla} \cdot \boldsymbol{u})}{\partial t} = k\mathbf{\nabla}^2 T + C_b \omega_b \rho_b (T_b - T) + Q_m + Q_{ext}$$

where ρ is density, C is the specific heat, T is the temperature at time t, k is the thermal conductivity, C_b is the specific heat of blood, ω_b is the blood perfusion, ρ_b is the density of blood, T_b is the temperature of blood vessel, Q_m is the generated metabolic heat and Q_{ext} is the external heat source.

Since the heat flux $\mathbf{q}(\boldsymbol{r}, t)$ can be expressed in the following form, where r denotes the position vector,

$$\mathbf{q}(\boldsymbol{r}, t) = -k\mathbf{\nabla}T$$

Applying the concept of finite heat propagation velocity, a modified unsteady heat conduction equation [125, 126] is formulated in Eq. 6-3, where τ_p is thermal relaxation time of soft tissue.

$$\mathbf{q}(\boldsymbol{r}, t + \tau_p) = -k\mathbf{\nabla}T$$

Using first order Taylor expansion, the above equation becomes,

$$\mathbf{q}(r, t + \tau_p) = \mathbf{q}(r, t) + \tau_p \frac{\partial \mathbf{q}(r, t)}{\partial t}$$

Combining Eq. 6-2 and Eq. 6-4, $-k\boldsymbol{\nabla}^2 T$ in Eq. 6-1 can be written in the following expression,

$$\boldsymbol{\nabla}\left(\mathbf{q}(r, t) + \tau_p \frac{\partial \mathbf{q}(r, t)}{\partial t}\right) = -k\boldsymbol{\nabla}^2 T$$

Also from Eq. 6-1 and Eq. 6-2, we can also get the equivalent of $\boldsymbol{\nabla}\big(\boldsymbol{q}(\boldsymbol{r}, t)\big)$,

$$\boldsymbol{\nabla}\big(\boldsymbol{q}(r, t)\big) = -\rho C \frac{\partial T}{\partial t} - \beta T_0 \frac{\partial(\boldsymbol{\nabla}\cdot\boldsymbol{u})}{\partial t} + C_b \omega_b \rho_b (T_b - T) + Q_m + Q_{ext}$$

Substituting Eq. 6-6 into Eq. 6-5, so that,

$$-\rho C \frac{\partial T}{\partial t} - \beta T_0 \frac{\partial(\boldsymbol{\nabla}\cdot\boldsymbol{u})}{\partial t} + C_b \omega_b \rho_b (T_b - T) + Q_m + Q_{ext}$$

$$+ \tau_p \frac{\partial\left(-\rho C \dfrac{\partial T}{\partial t} - \beta T_0 \dfrac{\partial(\boldsymbol{\nabla}\cdot\boldsymbol{u})}{\partial t} + C_b \omega_b \rho_b (T_b - T) + Q_m + Q_{ext}\right)}{\partial t}$$

$$= -k\boldsymbol{\nabla}^2 T$$

Rearranging Eq. 6-7 yields [127],

$$\tau_p \rho C \frac{\partial^2 T}{\partial t^2} + \big(\tau_p C_b \omega_b \rho_b + \rho C\big)\frac{\partial T}{\partial t} + \tau_p \beta T_0 \frac{\partial^2(\boldsymbol{\nabla}\cdot\boldsymbol{u})}{\partial t^2} + \beta T_0 \frac{\partial(\boldsymbol{\nabla}\cdot\boldsymbol{u})}{\partial t}$$

$$= k\boldsymbol{\nabla}^2 T + \tau_p \frac{\partial Q_m}{\partial t} + \tau_p \frac{\partial Q_{ext}}{\partial t} + C_b \omega_b \rho_b (T_b - T) + Q_m + Q_{ext}$$

which is the non-Fourier form of bioheat transfer equation.

Regarding the thermal relaxation time approximation, denoted as τ_p in above, there is still no direct experimental method existed for its determination at present. But it has been suggested that τ_p can be determined by fitting experimental temperature data with established non-Fourier bioheat transfer equation, by using τ_p as a variable parameter. Most biological materials that contain cells, superstructures, liquids, and solid tissues are non-homogeneous, so that their thermal relaxation times are much larger compared to homogeneous substances (ranging from 10^{-14} to 10^{-8}). Among relevant studies, Mitra et al. found that the value of τ_p in processed meat is about 15.5 s [50], Roetzel et al. found it to be 1.77 s [128]. For a more homogeneous inner structure cornea, it is considered to have a lower value of τ_p = 0.1 s by López-Molina et al. [21].

6.2   The finite element method

On discretising our proposed model using continuum approach in Chapter 4, the adopted FDM method only considers regular volume meshes. For the proposed model in this chapter, we extends the numerical modelling to deal with complex irregular volume meshes like human organ, by referring to the finite element scheme.

The following gives the FEM discretisation process based on our established governing equations in detailed steps:
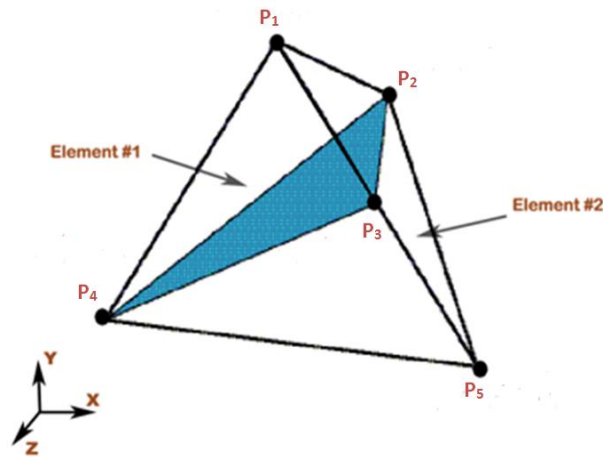
Figure 28: Tetrahedron element

Step 1: On discretising non-Fourier bioheat transfer equation as established above using finite element scheme, firstly, the temperature field within an individual four-node linear tetrahedron element (e) (see Figure 28) is approximated in terms of shape functions,

$$T^{(e)}(x, y, z) = N_r \{T_r\}$$

Here, T_r is the temperature component at each element node. The shape function $N_r = \{N_{r1}, N_{r2}, N_{r3}, N_{r4}\}$ is function of space variables. And the integrated form of Eq. 6-8 over an individual element is obtained by applying Galerkin's weighted residual method as following, where the test function $N_{rr} = [N_r]^T$, are used as the weighting factors [129],

$$\int_{V(e)} \left(\tau_p \rho C \frac{\partial^2 T}{\partial t^2} + \left(\tau_p C_b \omega_b \rho_b + \rho C \right) \frac{\partial T}{\partial t} + \tau_p \beta T_0 \frac{\partial^2 (\boldsymbol{\nabla} \cdot \boldsymbol{u})}{\partial t^2} + \beta T_0 \frac{\partial (\boldsymbol{\nabla} \cdot \boldsymbol{u})}{\partial t} - k \boldsymbol{\nabla}^2 T \right.$$

$$\left. - \tau_p \frac{\partial Q_m}{\partial t} - \tau_p \frac{\partial Q_{ext}}{\partial t} - C_b \omega_b \rho_b (T_b - T) - Q_m - Q_{ext} \right) N_{,,} dV$$

$$= 0$$

Meanwhile, the integrated form of heat flux can be rewritten as,

$$\int_{V(e)} (-k \boldsymbol{\nabla}^2 T) N_{,,} \, dV = \int_{V(e)} q_{i,i} N_{,,} \, dV = \int_{A(e)} (q_i n_i) N_{,,} dA - \int_{V(e)} q_i \frac{\partial N_{,,}}{\partial x_i} dV$$

Rearranging the form, we have,

$$\left(\int_{V(e)} \tau_p \rho C N_{,,} N_{,} \, dV \right) \ddot{\theta} + \left(\int_{V(e)} (\tau_p C_b \omega_b \rho_b + \rho C) N_{,,} N_{,} \, dV \right) \dot{\theta}$$

$$+ \left(\int_{V(e)} k \frac{\partial N_{,,}}{\partial x} \frac{\partial N_{,}}{\partial x} \, dV + \int_{V(e)} k \frac{\partial N_{,,}}{\partial y} \frac{\partial N_{,}}{\partial y} \, dV \right.$$

$$\left. + \int_{V(e)} k \frac{\partial N_{,,}}{\partial z} \frac{\partial N_{,}}{\partial z} \, dV \right) \theta + \left(\int_{V(e)} C_b \omega_b \rho_b N_{,,} N_{,} \, dV \right) \theta$$

$$+ \left(\int_{V(e)} \tau_p \beta T_0 \frac{\partial N_{,,}}{\partial x} N_{,} dV \right) \ddot{u}_x + \left(\int_{V(e)} \tau_p \beta T_0 \frac{\partial N_{,,}}{\partial y} N_{,} dV \right) \ddot{v}$$

$$+ \left(\int_{V(e)} \tau_p \beta T_0 \frac{\partial N_{,,}}{\partial z} N_{,} dV \right) \ddot{n} + \left(\int_{V(e)} \beta T_0 \frac{\partial N_{,,}}{\partial x} N_{,} dV \right) \dot{u}$$

$$+ \left(\int_{V(e)} \beta T_0 \frac{\partial N_{,,}}{\partial y} N_{,} dV \right) \dot{v} + \left(\int_{V(e)} \beta T_0 \frac{\partial N_{,,}}{\partial z} N_{,} dV \right) \dot{n}$$

$$= \int_{V(e)} \left(\tau_p \frac{\partial Q_m}{\partial t} + \tau_p \frac{\partial Q_{ext}}{\partial t} + Q_m + Q_{ext} \right) N_{,,} \, dV$$

$$- \int_{A(e)} (q_i n_i) N_{,,} dA$$

<div align="right">**Eq. 6-12**</div>

Step 2: For discretisation of the dynamic system model Eq. 4-25 as mentioned in Chapter 4 using finite element scheme, displacement components within an individual element (e) are approximated in terms of the same shape functions as used for temperature field approximation.

$$u_i^{(e)}(x, y, z) = N_{,} \{U_i\}$$

<div align="right">**Eq. 6-13**</div>

Similarly, using the same the weighting functions $N_{,,}$, the formal Galerkin approximation of motion dynamic governing equation is reduced to,

$$\int_{V(e)} \left(\rho \ddot{u}_i - \sigma_{ij,j} - F_i \right) N_{,,} dV = 0$$

For the second term of the above equation, its integrated form can be further written as,

$$\int_{V(e)} (\sigma_{ij,j}) N_{,,} dV = \int_{A(e)} \sigma_{ij} n_j N_{,,} dA - \int_{V(e)} \frac{\partial N_{,,}}{\partial x_j} \sigma_{ij} dV$$

where n_j is the component of the unit outer normal vector to the boundary. Substituting Eq.6-15 into Eq.6-14 gives,

$$\int_{V(e)} \rho \ddot{u}_i N_{,,} dV - \int_{A(e)} \sigma_{ij} n_j N_{,,} dA + \int_{V(e)} \frac{\partial N_{,,}}{\partial x_j} \sigma_{ij} dV - \int_{V(e)} F_i N_{,,} dV = 0$$

According to Cauchy's formula, the traction force components acting on the boundary are related to the stress tensor as,

$$t_i^n = \sigma_{ij} n_j$$

Combining these equations Eq.6-16 and Eq.6-17 we have,

$$\int_{V(e)} \rho \ddot{u}_i N_{,,} dV + \int_{V(e)} \frac{\partial N_{,,}}{\partial x_j} \left(\mu \left(u_{i,j} + u_{j,i} \right) + \lambda u_{k,k} \delta_{ij} - \beta \theta \delta_{ij} \right) dV = \int_{A(e)} t_i^n N_{,,} dA$$

$$+ \int_{V(e)} F_i N_{,,} dV$$

Now, the displacement components in the base element (e) are approximated by Eq. 6-18. For a three-dimensional problem, using these approximation, Eq. 6-18 is expanded into three equations in x, y and z-directions, as follows,

$$\left(\int_{V(e)} \rho N_{,,} N_{,} dV \right) \ddot{u}_x$$

$$+ \left(\int_{V(e)} \mu \frac{\partial N_{,,}}{\partial x} \frac{\partial N_{,}}{\partial x} dV + \int_{V(e)} \mu \frac{\partial N_{,,}}{\partial y} \frac{\partial N_{,}}{\partial y} dV \right.$$

$$+ \int_{V(e)} \mu \frac{\partial N_{,,}}{\partial z} \frac{\partial N_{,}}{\partial z} dV \left. \right) u_x + \left(\int_{V(e)} \frac{\mu}{1-2v} \frac{\partial N_{,,}}{\partial x} \frac{\partial N_{,}}{\partial x} dV \right) u_x$$

$$+ \left(\int_{V(e)} \frac{\mu}{1-2v} \frac{\partial N_{,,}}{\partial x} \frac{\partial N_{,}}{\partial y} dV \right) u_y + \left(\int_{V(e)} \frac{\mu}{1-2v} \frac{\partial N_{,,}}{\partial x} \frac{\partial N_{,}}{\partial z} dV \right) u_z$$

$$- \left(\int_{V(e)} \beta \frac{\partial N_{,,}}{\partial x} N_{,} dV \right) \theta = \int_{A(e)} t_x^n N_{,,} dA + \int_{V(e)} F_x N_{,,} dV$$

<div align="right">**Eq. 6-19**</div>

$$\left(\int_{V(e)} \rho N_{,,} N_{,} dV \right) \ddot{u}_y$$

$$+ \left(\int_{V(e)} \mu \frac{\partial N_{,,}}{\partial x} \frac{\partial N_{,}}{\partial x} dV + \int_{V(e)} \mu \frac{\partial N_{,,}}{\partial y} \frac{\partial N_{,}}{\partial y} dV \right.$$

$$+ \int_{V(e)} \mu \frac{\partial N_{,,}}{\partial z} \frac{\partial N_{,}}{\partial z} dV \left. \right) u_y + \left(\int_{V(e)} \frac{\mu}{1-2v} \frac{\partial N_{,,}}{\partial y} \frac{\partial N_{,}}{\partial x} dV \right) u_x$$

$$+ \left(\int_{V(e)} \frac{\mu}{1-2v} \frac{\partial N_{,,}}{\partial y} \frac{\partial N_{,}}{\partial y} dV \right) u_y + \left(\int_{V(e)} \frac{\mu}{1-2v} \frac{\partial N_{,,}}{\partial y} \frac{\partial N_{,}}{\partial z} dV \right) u_z$$

$$- \left(\int_{V(e)} \beta \frac{\partial N_{,,}}{\partial x} N_{,} dV \right) \theta = \int_{A(e)} t_y^n N_{,,} dA + \int_{V(e)} F_y N_{,,} dV$$

<div align="right">**Eq. 6-20**</div>

$$\left(\int_{V(e)} \rho N_{,,} N_{,} dV \right) \ddot{u}_z$$

$$+ \left(\int_{V(e)} \mu \frac{\partial N_{,,}}{\partial x} \frac{\partial N_{,}}{\partial x} dV + \int_{V(e)} \mu \frac{\partial N_{,,}}{\partial y} \frac{\partial N_{,}}{\partial y} dV \right.$$

$$+ \int_{V(e)} \mu \frac{\partial N_{,,}}{\partial z} \frac{\partial N_{,}}{\partial z} dV \left. \right) u_z + \left(\int_{V(e)} \frac{\mu}{1 - 2v} \frac{\partial N_{,,}}{\partial z} \frac{\partial N_{,}}{\partial x} dV \right) u_x$$

$$+ \left(\int_{V(e)} \frac{\mu}{1 - 2v} \frac{\partial N_{,,}}{\partial z} \frac{\partial N_{,}}{\partial y} dV \right) u_y + \left(\int_{V(e)} \frac{\mu}{1 - 2v} \frac{\partial N_{,,}}{\partial z} \frac{\partial N_{,}}{\partial z} dV \right) u_z$$

$$- \left(\int_{V(e)} \beta \frac{\partial N_{,,}}{\partial x} N_{,} dV \right) \theta = \int_{A(e)} t_z^n N_{,,} dA + \int_{V(e)} F_z N_{,,} dV$$

Step 3: Combining these two discretisations: temperature and displacement field together, since they are coupled, one can get the discrete equilibrium equation for each element in question. Taking two connected tetrahedron elements for example (see Figure 28), where the element composition is as shown in Table 5. Stiffness matrix K for element 1 has the form $K_{(1)}$, for element 2, it is like $K_{(2)}$, as shown in Figure 29. Assembling two elements, one can get the stiffness matrix $K_{(12)}$, as shown in Figure 30.

Step 4: Integrating each component and assembling all included elements under consideration, finally one will get a global characteristic equation for all mesh points, expressed in a matrix form as follows. From which, the temperature and displacement components, as well as the external heating source and applied force are all related.

$$M \underline{\ddot{u}} + C \underline{\dot{u}} + K \underline{u} = F$$

$$\underline{u} = \begin{Bmatrix} \theta \\ u \end{Bmatrix}$$

where M is the global mass matrix, C is the global damping matrix, $\underline{u}$ is the combined temperature and displacement vector, K is the stiffness matrix, and F is the total external force.

Table 5: Node-element connectivity chart

Element	Node 1	Node 2	Node 3	Node 4
1	P_1	P_2	P_3	P_4
2	P_2	P_3	P_4	P_5
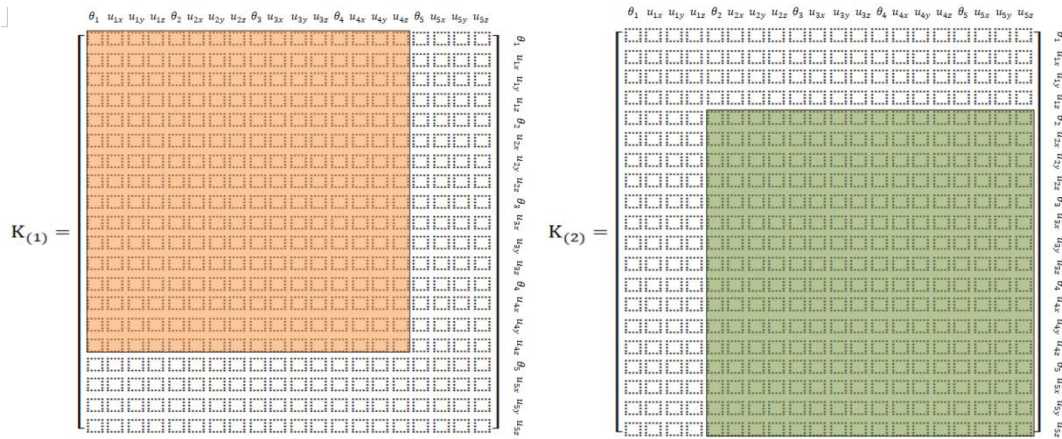
Figure 29: Stiffness matrix of element 1 (left) and stiffness matrix of element 2 (right)
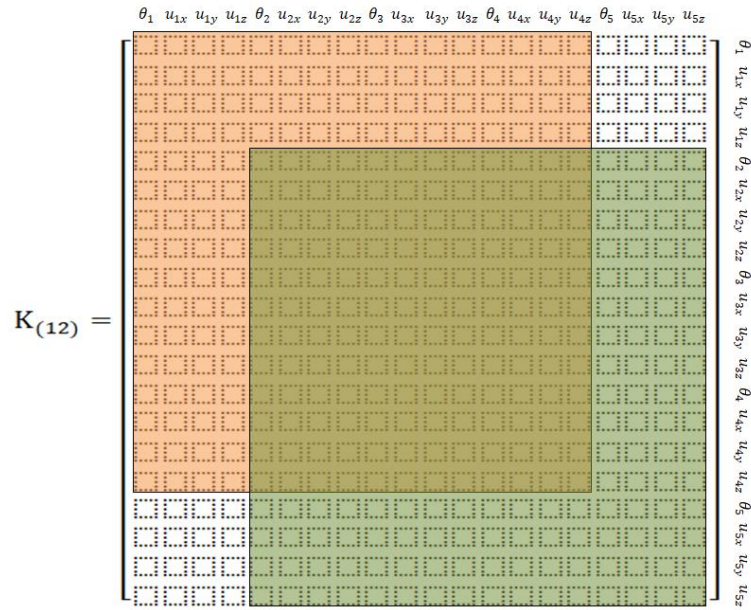
Figure 30: Global stiffness matrix of elements 1 and 2

Step 5: Finally, the thermal mechanical damage at the end of each time step can be expressed in the following expression, based on known thermal mechanical damage Ω^t at time t and strain energy $\acute{E}_{TM}{}^{t+\Delta t}$ during the time step: t to $t + \Delta t$.

$$\Omega^{t+\Delta t} = \Omega^t + A\,exp\left(-\frac{\Delta E - \acute{E}_{TM}{}^{t+\Delta t}}{RT}\right)\Delta t$$

<div align="right">

Eq. 6-24

</div>

Step 6: To maintain the stability of established simulation system under some large time steps, the implicit time integration scheme is adopted to approximate time derivatives included in the global matrix, which maintains a first order time accuracy.

$$\ddot{\boldsymbol{u}}^{t+\Delta t} = \frac{\dot{\boldsymbol{u}}^{t+\Delta t} - \dot{\boldsymbol{u}}^t}{\Delta t} = \frac{\dfrac{\boldsymbol{u}^{t+\Delta t} - \boldsymbol{u}^t}{\Delta t} - \dfrac{\boldsymbol{u}^t - \boldsymbol{u}^{t-\Delta t}}{\Delta t}}{\Delta t}$$

<div align="right">

Eq. 6-25

</div>

$$\dot{T}^{t+\Delta t} = \frac{T^{t+\Delta t} - T^t}{\Delta t}$$

Substituting Eq.6-25 and Eq.6-26 into Eq.6-22, and rewrite it, we get,

$$\left(\frac{\boldsymbol{M}}{\Delta t^2} + \frac{\boldsymbol{C}}{\Delta t} + \boldsymbol{K}\right)\underline{\boldsymbol{u}}^{t+\Delta t} = \left(\frac{2\boldsymbol{M}}{\Delta t^2} + \frac{\boldsymbol{C}}{\Delta t}\right)\underline{\boldsymbol{u}}^t - \frac{\boldsymbol{M}}{\Delta t^2}\underline{\boldsymbol{u}}^{t-\Delta t} + \boldsymbol{F}^{t+\Delta t}$$

6.3 Condensation

Firstly, rewrite Eq.6-27 into the following form. In order to reduce computation time and realize real-time simulation based on our proposed model, K' can be pre-computed to save memory.

$$\boldsymbol{K}'\underline{\boldsymbol{u}}^{t+\Delta t} = \boldsymbol{b}^{t+\Delta t}$$

with,

$$\boldsymbol{K}' = \frac{\boldsymbol{M}}{\Delta t^2} + \frac{\boldsymbol{C}}{\Delta t} + \boldsymbol{K}$$

$$\boldsymbol{b}^{t+\Delta t} = \left(\frac{2\boldsymbol{M}}{\Delta t^2} + \frac{\boldsymbol{C}}{\Delta t}\right)\underline{\boldsymbol{u}}^t - \frac{\boldsymbol{M}}{\Delta t^2}\underline{\boldsymbol{u}}^{t-\Delta t} + \boldsymbol{F}^{t+\Delta t}$$

As matrix system Eq.6-28 models the behaviour of target object volumetrically, it contains information of both internal and surface nodes. Providing the simulation purpose of our target problem only concerns internal nodes (or some of the internal nodes), we use condensation to surface points (or the rest of selected internal points)

from Eq.6-28. However, the behaviour of internal nodes will show exactly the same as original volumetric system, only the matrix size is reduced for improving of computation efficiency.

Assuming numbering of volumetric nodes that forming the finite element model is ordered with surface nodes (denoted as s) comes firstly and then internal nodes (denoted as i). Eq.6-28 can be rewritten in the following form of block matrix system, as,

$$\begin{bmatrix} K'_{ss} & K'_{si} \\ K'_{is} & K'_{ii} \end{bmatrix} \begin{bmatrix} \underline{u}_s^{t+\Delta t} \\ \underline{u}_i^{t+\Delta t} \end{bmatrix} = \begin{bmatrix} b_s^{t+\Delta t} \\ b_i^{t+\Delta t} \end{bmatrix}$$

<div align="right">Eq. 6-31</div>

Creating a matrix system that only includes variables of internal nodes:

$$K'^*_{ii} \underline{u}_i^{t+\Delta t} = b_i^{t+\Delta t *}$$

<div align="right">Eq. 6-32</div>

Here,

$$K'^*_{ii} = K'_{ii} - K'_{is} K'_{ss}^{-1} K'_{si}$$

<div align="right">Eq. 6-33</div>

$$b_i^{t+\Delta t *} = b_i^{t+\Delta t} - K'_{is} K'_{ss}^{-1} b_s^{t+\Delta t}$$

<div align="right">Eq. 6-34</div>

The entire simulation algorithm can be described as: 1. Solving matrix $K'^*_{ii}{}^{-1}$ and $K'_{is} K'_{ss}^{-1}$ in the pre-computation stage at $t = 0$, and store it in memory; 2. Calculating vector $b^{t+\Delta t}$ at each time step using stored matrix $K'_{is} K'_{ss}^{-1}$ and updated vectors $b_i^{t+\Delta t}$ and $b_s^{t+\Delta t}$; 3. The matrix vector multiplication in Eq. 6-32 is calculated using

selected numerical algorithm. For different boundary conditions: for example free and fixed surfaces movement, the way we impose such boundary condition is by switching on and off surfaces movement. For another example of constant and not constant surface temperature boundary conditions, the boundary condition is imposed by switching on and off constant surface temperatures.

6.4   Convergence testing

Figure 31 shows the number of Gauss-Seidel solver iterations against the margin of error for a typical simulation of linear thermal mechanical interaction using FEM method. Similar conclusion can be derived as smaller margins of error allow for greater accuracy of computation results but requires a larger number of solver iterations. Meanwhile, more iterations are needed for the same level of convergence to be reached for FEM based model than FDM based model, see Figure 8.
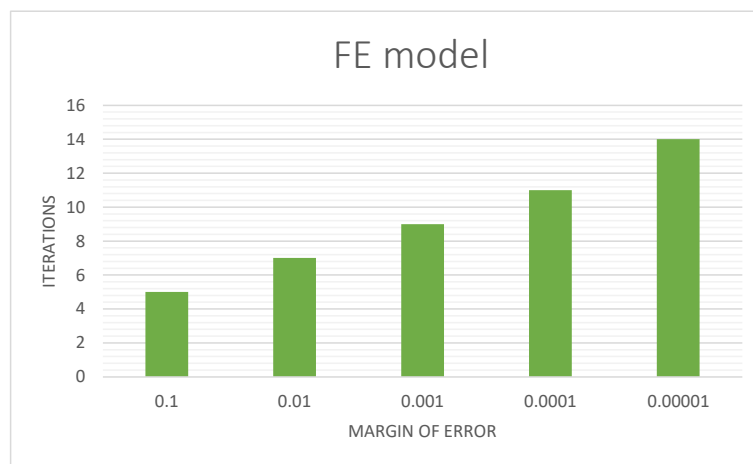
Figure 31: Number of iterations vs. margin of error for linear FE model

6.5 Results and discussion

6.5.1 Case study I: cubic-shape tissue model

In this section, trials are conducted to evaluate the performance of our proposed non-Fourier thermal mechanical model in terms of a cubic-shape tissue model, as aforementioned in Chapter 4. Meshing it up using tetrahedron elements, the tissue mesh model contains 6000 elements with 1331 nodes (see Figure 32). The needle used in a typical thermal ablation treatment is modelled as a straight line, with five evenly spaced points at its tip to generate heat energy at 0.08 W on each point (see Figure 33). Parameters used in this chapter are as shown in Table 6 and other used thermal and mechanical parameters are as listed in Table 2 and Table 4. During numerical solving, fixed boundary and constant temperature of 310 K at all surfaces were set, and at $t = 0$ s, we assume $T_0 = 310$ K, and no strain inside the tissue model before applying heat.
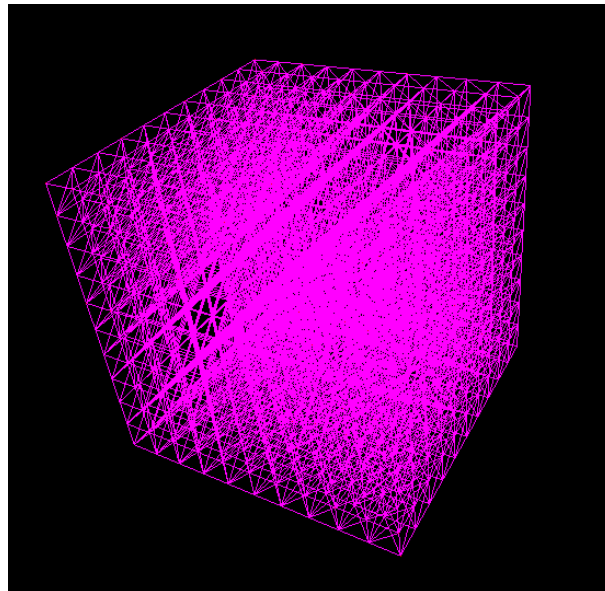
Figure 32: Meshing of cubic-shape tissue model using tetrahedron elements
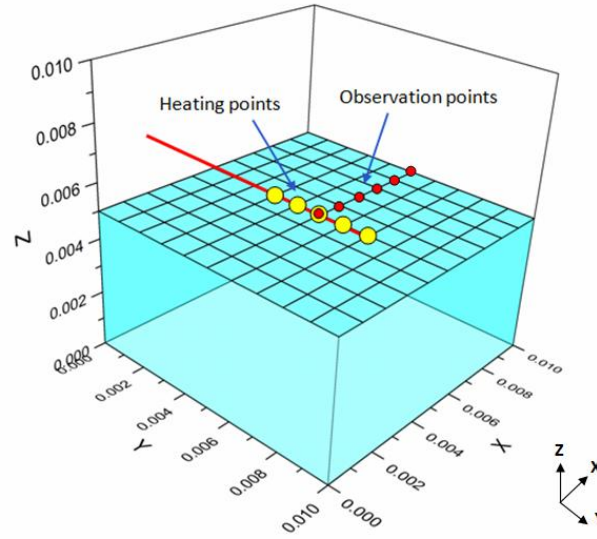
Figure 33: Positioning of heating sources

Table 6: Tissue parameters and constants

Parameters	Value
Young's modulus E; Pa	10.2×10^6
Poisson's ratio v;	0.35
Characteristic Time τ_p; s	16

6.5.1.1 Temperature distribution

Based on the numerical method FEM, the simulation results based on our proposed model in this chapter: non-Fourier based thermal mechanical model, is compared with previous presented model in chapter 4: Fourier based thermal mechanical model which ignores the non-Fourier behaviour of heat transfer in soft tissue during thermal ablation process. Three observation points: P_1 (x=0.005m, y=0.005m, z=0.005m), P_2 (x=0.006m, y=0.005m, z=0.005m), P_3 (x=0.007m, y=0.005m, z=0.005m) are chosen to observe the thermo-mechanical behaviour of the cubic-shape tissue model (see Figure 31). Figure 34 illustrates the temperature changes at these points within a heating period of 120 s for two models. As we can see, at the beginning of heating for non-

Fourier model, the temperature rising involves oscillations, and relatively smaller values of temperature are observed, while for Fourier model the temperature keeps increasing gradually during the whole process. As the exposure time approaches steady-state conditions, temperature rise for both models merges at a closed value at each selected point.
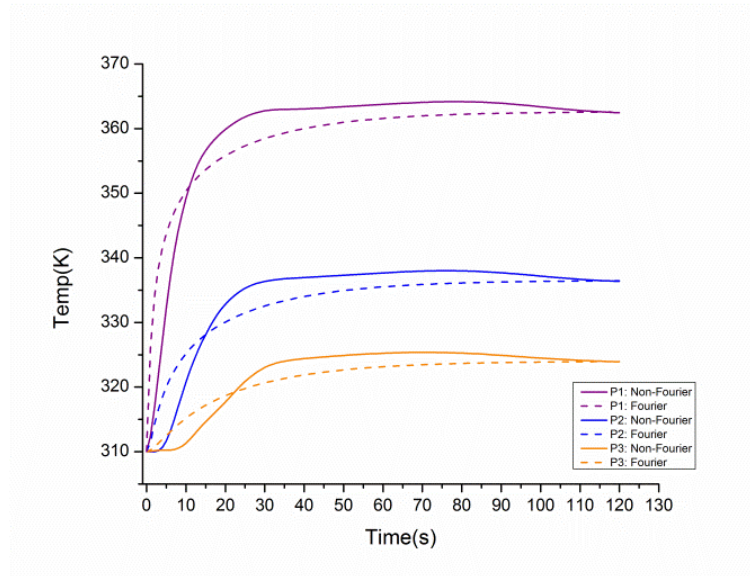
Figure 34: Temperature change at selected points

Considering the position and distribution of applied heating sources, one specific plane that is perpendicular to the heating line: Y=0.005m, is also selected to show temperature distribution at 10s and 120s (see Figure 35 and Figure 36). As expected, the highest temperature is reached at the centre of selected plane, while points located around it with equal distances have same predicted temperatures. Due to time relaxation of heat transfer as considered in non-Fourier model, temperature distribution at initial heating shows relatively lower temperature value across the

entire selected plane, while a similar steady state value is reached for both models at the end of simulation time.

Figure 35: Comparison of temperature distribution between Fourier (left) and non-Fourier model (right) at 10s
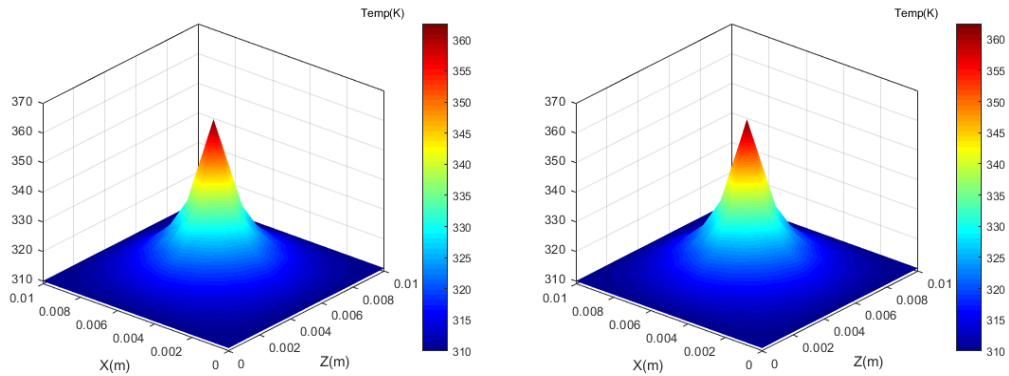
Figure 36: Comparison of temperature distribution between Fourier (left) and non-Fourier model (right) at 120s

6.5.1.2 *Strain, stress and strain energy distribution*

For Fourier and non-Fourier thermal mechanical model, Figure 37 also gives strain distribution: $(\varepsilon_{xx}, \varepsilon_{yy}, \varepsilon_{zz})$ on plane: Y=0.005m, at simulation duration of 10s. As expected, ε_{xx} and ε_{zz} shows quite similar plots, while the peak value of ε_{xx} and ε_{zz}

85

(same values) is larger comparing with ε_{yy}. Due to the thermal relaxation introduced in non-Fourier model, generated strain shows a relatively lower value than Fourier model at initial heating: 10s. But for strain distribution at the end of heating: 120s (see Figure 38), such difference is almost negligible. Meanwhile, positive strain are only observed at points near the heating centre, while negative strain happens at points close to fixed boundary surfaces. As aforementioned, the positive and negative strain can also be interpreted as soft tissue expansion and shrinkage respectively during physical experiments.

Figure 37: Comparison of strain $\varepsilon_{xx}, \varepsilon_{yy}, \varepsilon_{zz}$ distribution between Fourier (left) and non-Fourier model (right) at 10s
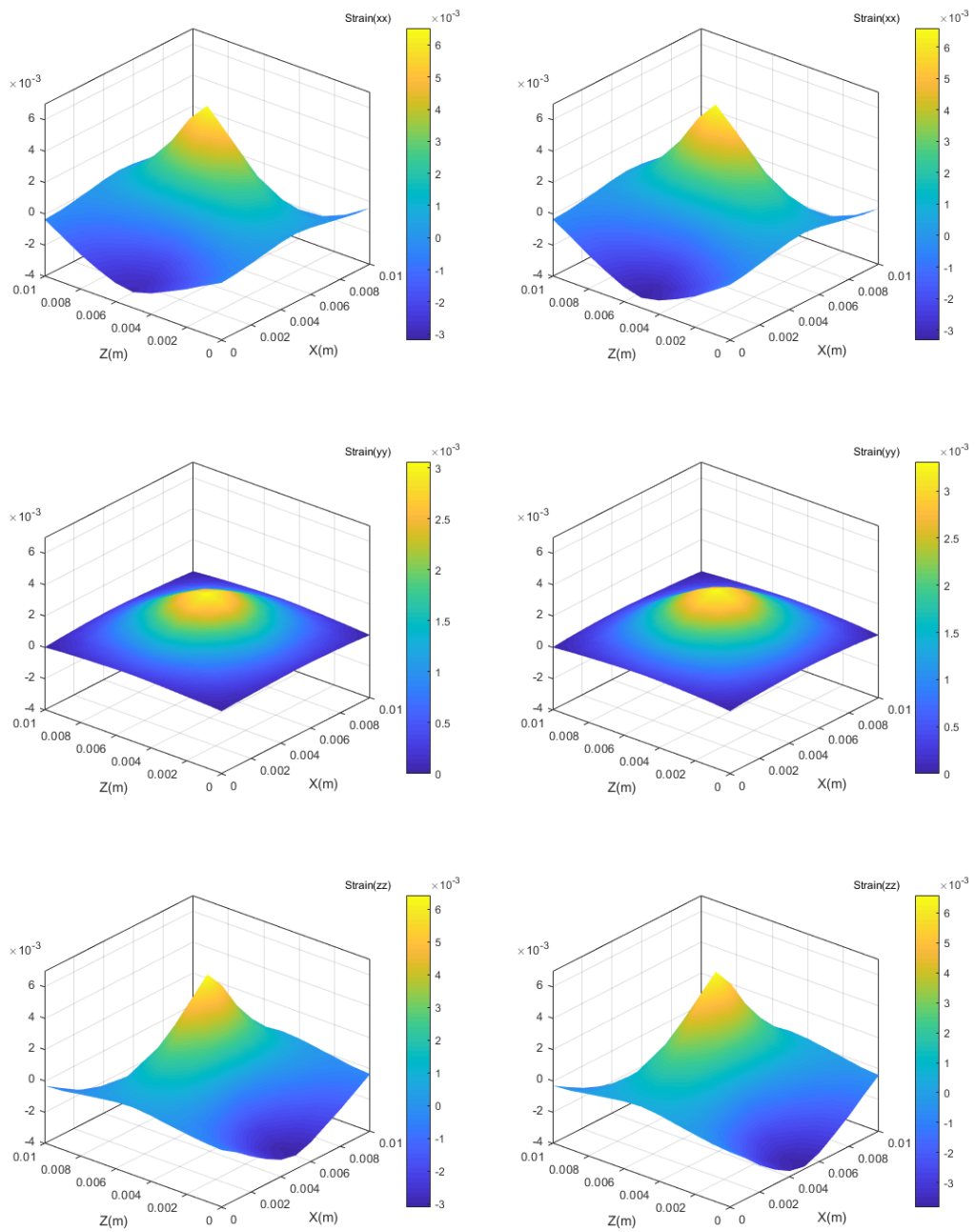
Figure 38: Comparison of strain $\varepsilon_{xx}, \varepsilon_{yy}, \varepsilon_{zz}$ distribution between Fourier (left) and non-Fourier model (right) at 120s

Move to stress field, similar trends for stress distribution: $(\sigma_{xx}, \sigma_{yy}, \sigma_{zz})$ at the same selected plane are observed as illustrated in Figure 39 and Figure 40, but the values of

them all show negative across selected plane. To explain this, we may refer to the fixed boundary condition which makes the target tissue cube not being able to expand during the entire heating process.
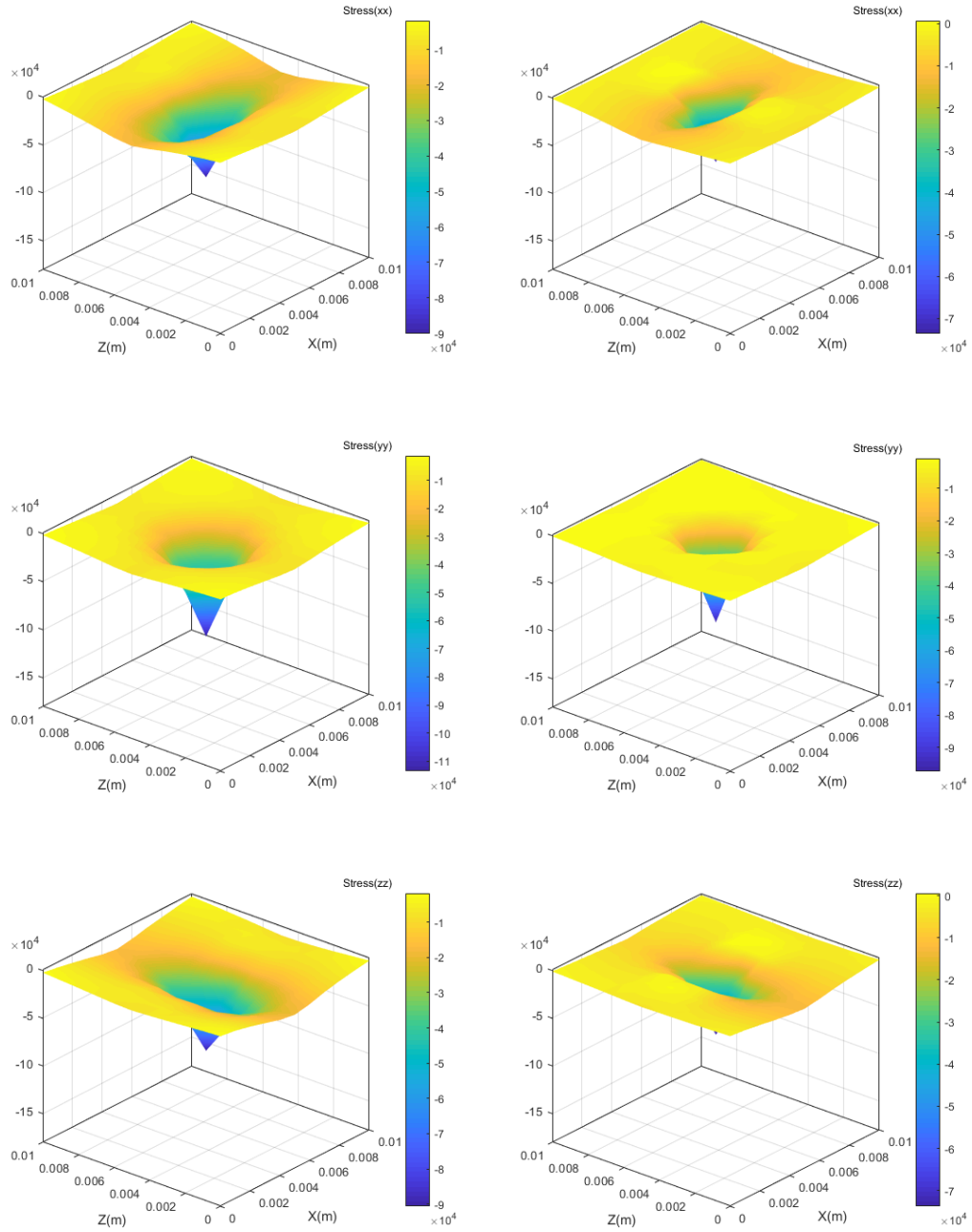
Figure 39: Comparison of stress $\sigma_{xx}, \sigma_{yy}, \sigma_{zz}$ distribution between Fourier (left) and non-Fourier model (right) at 10s
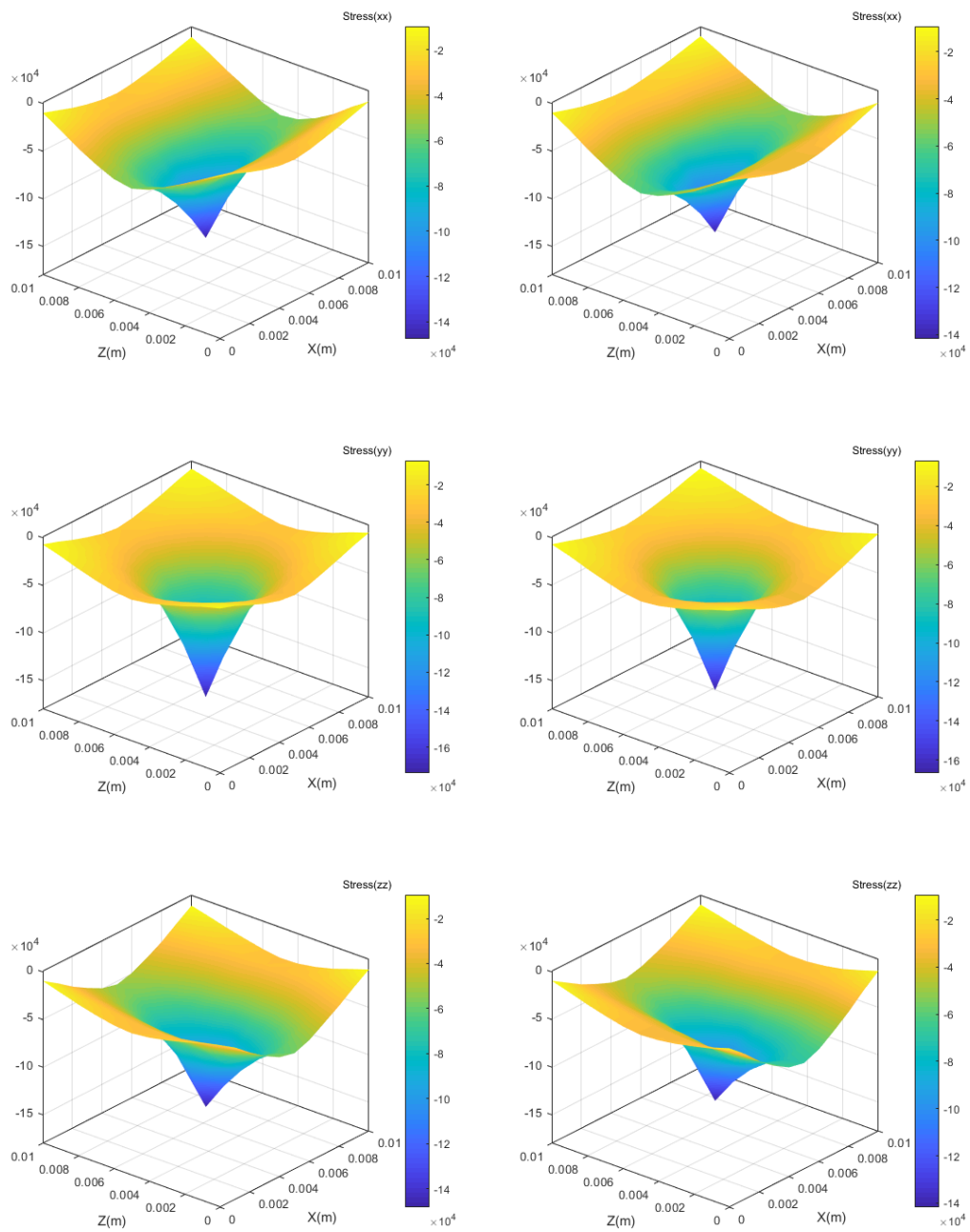
Figure 40: Comparison of stress $\sigma_{xx}, \sigma_{yy}, \sigma_{zz}$ distribution between Fourier (left) and non-Fourier model (right) at 120s

Considering distributions of strain and stress show similar trends, strain energy distributions at 10s and 120s of simulation are also plotted. As aforementioned in

Chapter 5, instead of using stored energy as calculated by Eq. 4-12 and Eq. 4-14 in Chapter 4, the stress expression is readjusted by taking out the thermal strain terms $3ka(\theta - \theta_0)$ in Eq. 4-12, considering only stored strain energy based on resultant tissue deformation is the key influence factor of our presented thermal mechanical damage model. As illustrated in Figure 41 and Figure 42, the same information of observable deviation is confirmed at initial stage of heating, while such a difference became negligible as the steady states of temperature distribution are reached for both models. Recalling the conclusion in Chapter 5 which demonstrates that the prediction deviation between traditional thermal and presented thermal mechanical damage model may be remarkable only if stored strain energy $\acute{E}_{TM}$ is comparable to ΔE, the influence of tissue deformation is not further identified in the following section because the observation results of strain energy in Figure 41 and Figure 42 are not comparable to the value of ΔE.
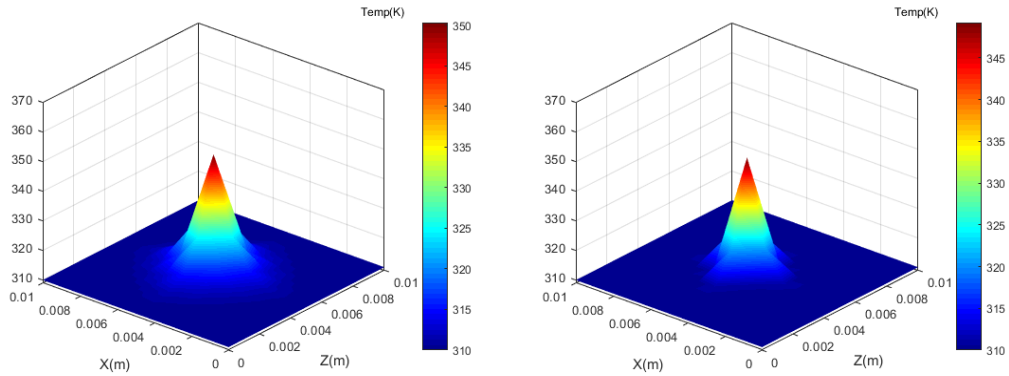

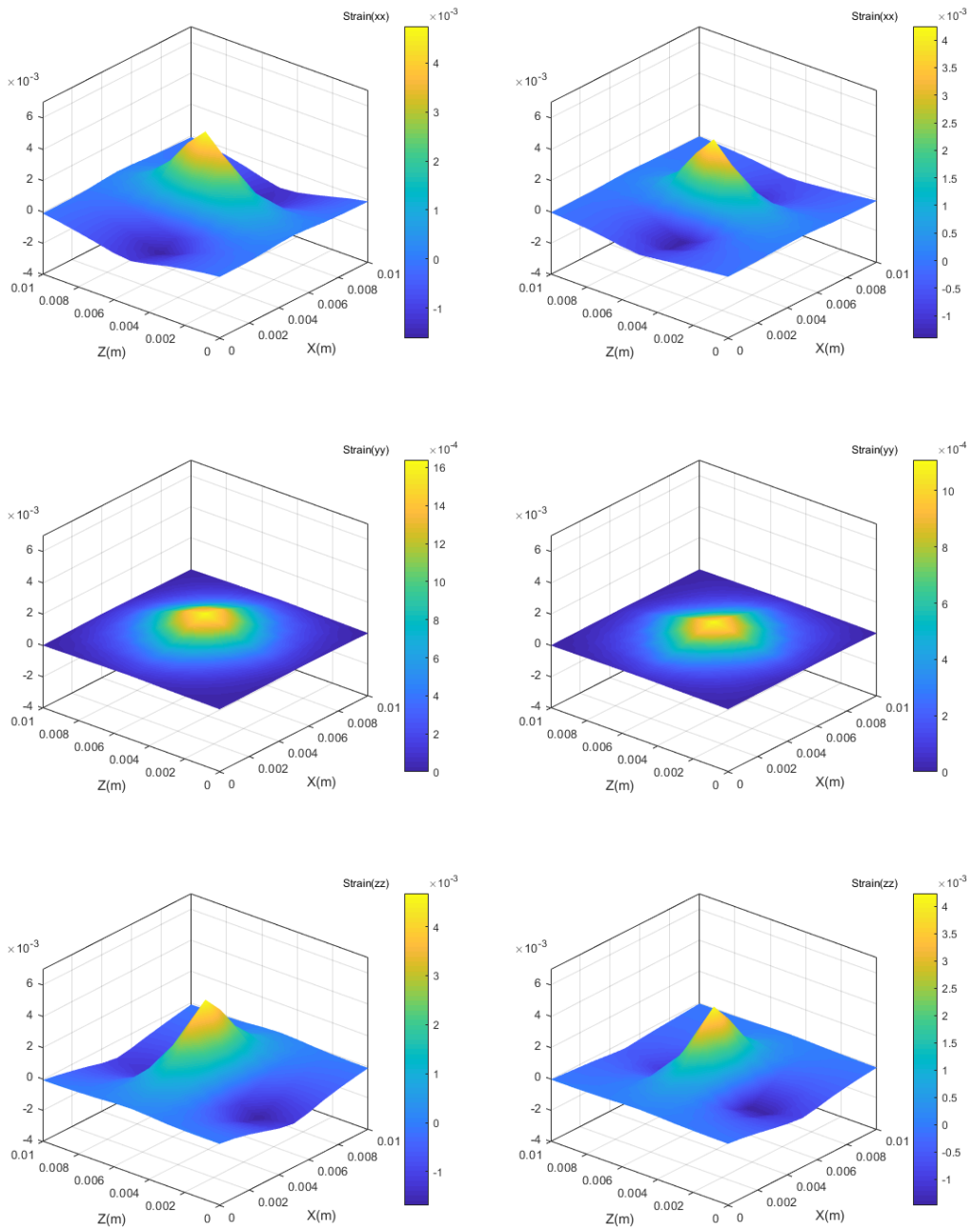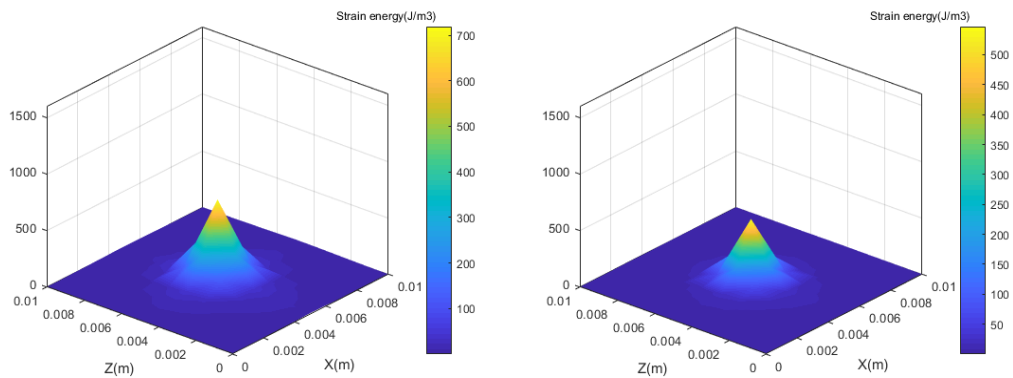Figure 41: Comparison of strain energy distribution between Fourier (left) and non-Fourier model (right) at 10s
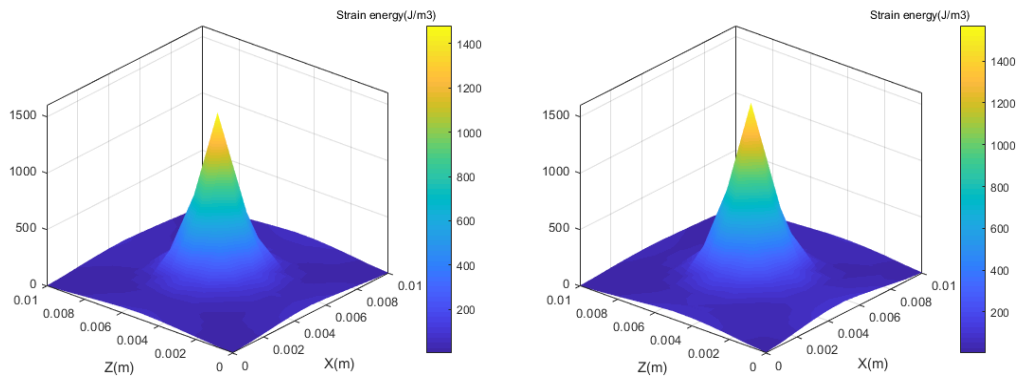
Figure 42: Comparison of strain energy distribution between Fourier (left) and non-Fourier model (right) at 120s

6.5.1.3   *Damage distribution*

Based on the above discussion on strain energy distribution, this section focuses evaluating the influence of Fourier and non-Fourier effect on prediction of soft tissue damage. Firstly, damage comparison between Fourier and non-Fourier thermal mechanical models are done at the observation points P_1-P_3 (see Figure 43) versus heating duration. Assuming that the threshold of irreversible thermal damage is $\Omega = 1$ [3], one can see that, for points near the heating centre: P_1 and P_2, thermal damage of the Fourier model increase faster and reach threshold damage earlier than non-Fourier based model, while delayed thermal damage is observed for points located further away (P_3) from heating centre using Fourier based model. It also has to be noted that, although a merged temperature may be predicted based on two bioheat transfer theories at the end of simulation, as shown in Figure 34, depending on two factors, namely thermal relaxation time of target tissue and defined damage threshold, the predicted tissue ablation boundary may be varied. In detail, as shown at observation point P_3 in Figure 43, the higher temperature prediction after certain time point using

non-Fourier based model (see Figure 34) makes this point reach the target damage state earlier than Fourier based model.
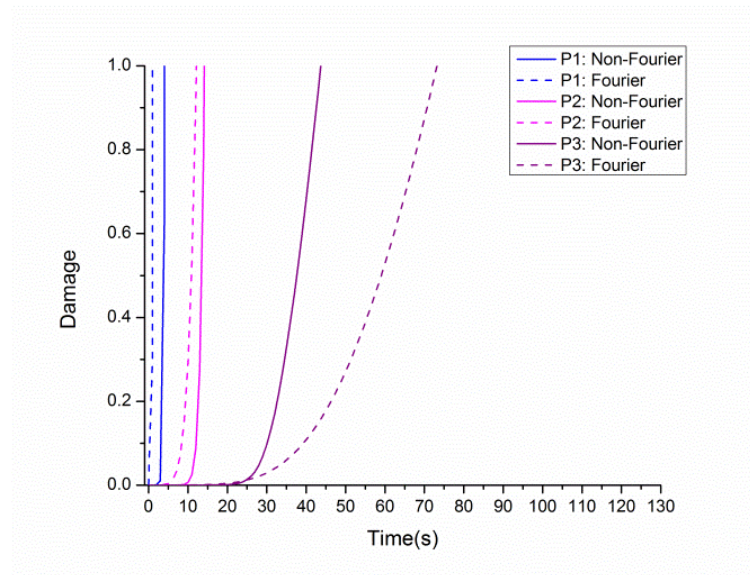
Figure 43: Damage vs. time comparison

To give it a clear description, damage distributions at plane Y=0.005m are further plotted at initial 10s and final 120s, see Figure 44 and Figure 45. Using the threshold $\Omega = 1$ to define tissue's thermal ablation zone, it is shown that the ablation zone for non-Fourier model is smaller than Fourier model at 10s of heating, but the final ablation zone at 120s is bigger than Fourier model. Regarding the smaller damage zone at 10s for non-Fourier model, it is because adopted tissue damage prediction model is an exponential function of temperature, so even a small deviation on temperature prediction can strongly affect the final tissue damage prediction, not to mention the obvious lower temperature prediction observed for non-Fourier based model at 10s. Or it can be explained as that the thermal relaxation of soft tissue would delay heat propagation among target tissue, leading to a lower tissue damage prediction for a

relatively short duration of heating. Regarding the larger damage zone at 120s for non-Fourier model, it can be attributed to the oscillation of temperature rising inside thermal treated tissue, as shown in Figure 34. Combining the defined damage threshold, it is possible that a target damage state would be reached before the steady state of heat transfer is completed within heated tissue.
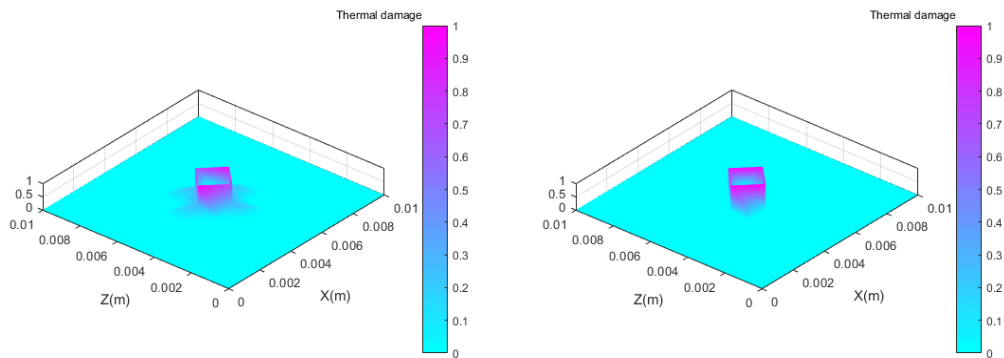
Figure 44: Comparison of ablation zone between Fourier model (left) and non-Fourier model (right) at 10s
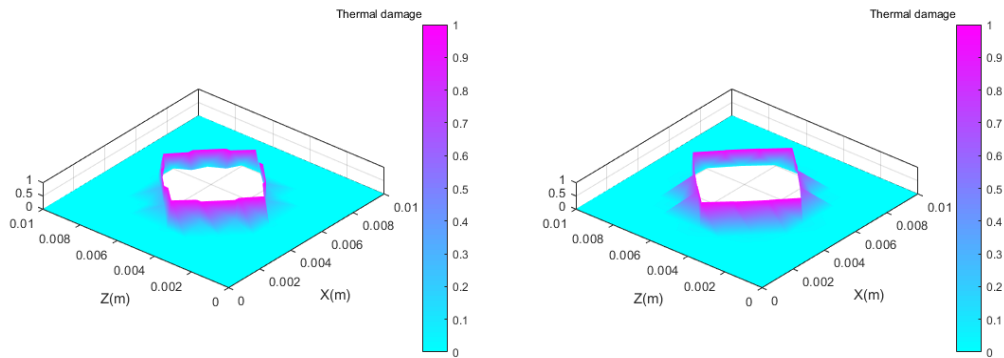
Figure 45: comparison of ablation zone between Fourier model (left) and non-Fourier model (right) at 120s

6.5.1.4 Execution time on computer

In practice, an applicable medical simulation system has to perform in an update rate of 15-20 frames/second [103], equals the requirement of a single iteration time less than 66.6 milliseconds. Still using the same meshed up tissue model as illustrated in Figure 30 to test the computation performance of our established non-Fourier based thermal mechanical model using FEM, but the boundary condition is changed into: free moving and heat convective boundary surfaces. It has to be mentioned that the computation costs are based on a Gauss-Seidel iterative solver on solving obtained linear system of equations after standard discretisations of governing equations using FEM method. By recording the end time of each iteration in development platform Netbeans IDE 8.1: "*DateFormat dateFormat = new SimpleDateFormat("yyyy/MM/dd HH:mm:ss.SSS")*", Table 7 provides comparison of computational cost (single iteration) for the proposed model in this chapter with and without using the condensation method described in section 6.3. Fundamentally, by applying condensation method, the basic determinant (simulation nodes number) for computation speeding would be reduced while the behaviour of condensed nodes still showing exactly the same as original mesh model. Simulation results shows that, instead of using all of the meshing nodes (1331) for calculating, proposed model applying condensation method reduces calculated nodes to 729 nodes, which makes it capable of achieving real-time performance for target problem with the margin of error of 0.001, as long as a pre-computation is performed on the host side.

Table 7: Computational time with and without condensation

Process(heating and deformation)	Without condensation/1331	With condensation/729
Single iteration	256-281 milliseconds	54-57 milliseconds

6.5.2   Case study II: liver-shape tissue model

For comparison purpose, the fixed and constant temperature at boundary surfaces are used in this section, but the trials are conducted in terms of a human liver-shape and sized tissue model to evaluate the performance of proposed non-Fourier thermal mechanical model. The liver-shape tissue model is meshed up using tetrahedron elements, which contains 5906 elements with 1642 nodes, as shown in Figure 46. Thermal ablation is performed by applying the same heating pattern with power of 0.08 W at each of the five heating points: (0.02m, 0.003m, -0.0285m), (0.02m, 0.004m, -0.0285m), (0.02m, 0.005m, -0.0285m), (0.02m, 0.006m, -0.0285m), (0.02m, 0.007m, -0.0285m) as aforementioned in case study I. The values of relevant thermal and mechanical parameters of the simulated liver-shape tissue model are as listed in Table 2, Table 4 and Table 6.
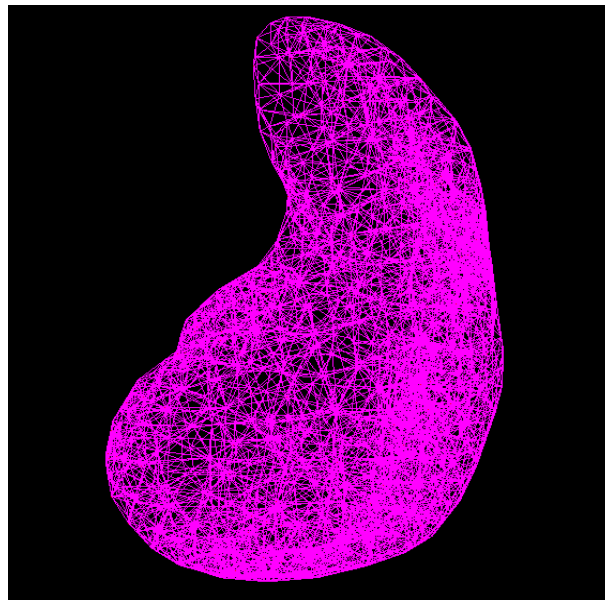
Figure 46: Meshing of liver-shape tissue model

A plane (Y=0.005m) located perpendicular to the heating line is selected to show temperature and damage distribution at the end of heating duration: 120 s, as shown in Figure 47 and Figure 48. However, comparing with the simulation results based on a purely cubic-shape tissue model as described in case study I, the temperature peak using liver-shape tissue model is obviously lower than purely cubic-shape tissue model in Figure 36 right. In addition, thermal ablation zone (defined using the threshold $\Omega = 1$) at this selected plane shows that the final damage radius under the same heating protocol is around 0.0018m, as shown in Figure 49, which is clearly smaller than the result of around 0.0022m using purely cubic-shape tissue model, as shown in Figure 45 right. To explain these, the input liver-shape tissue model is clearly larger in size than the aforementioned cubic-shape tissue body, so that the applied heat has been absorbed by the entire liver-shape tissue model instead of just the smaller sized cubic-shape tissue model.
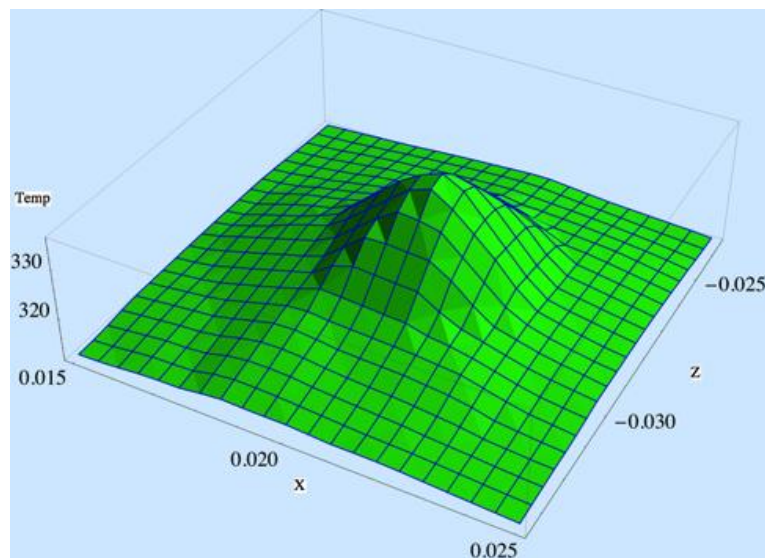
Figure 47: Temperature distribution for liver-shape tissue model at 120 s
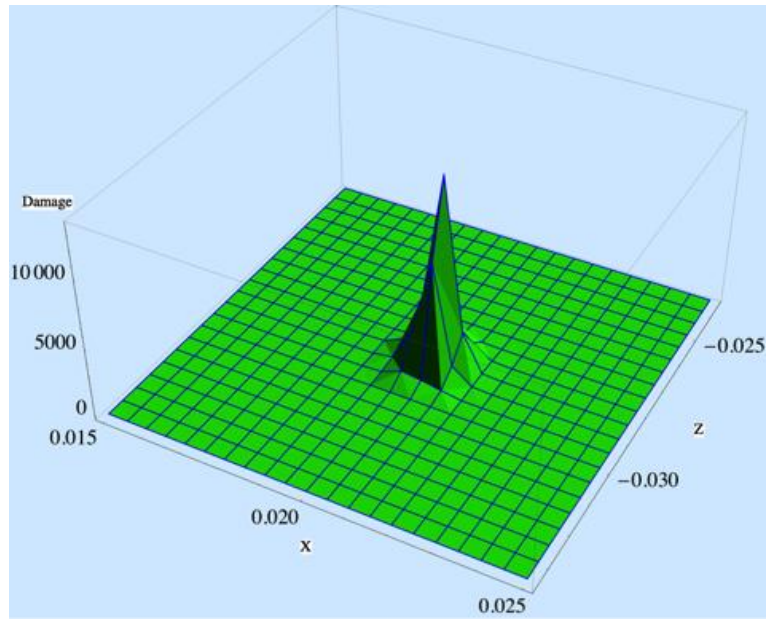
Figure 48: Thermal damage distribution for liver-shape tissue model at 120s
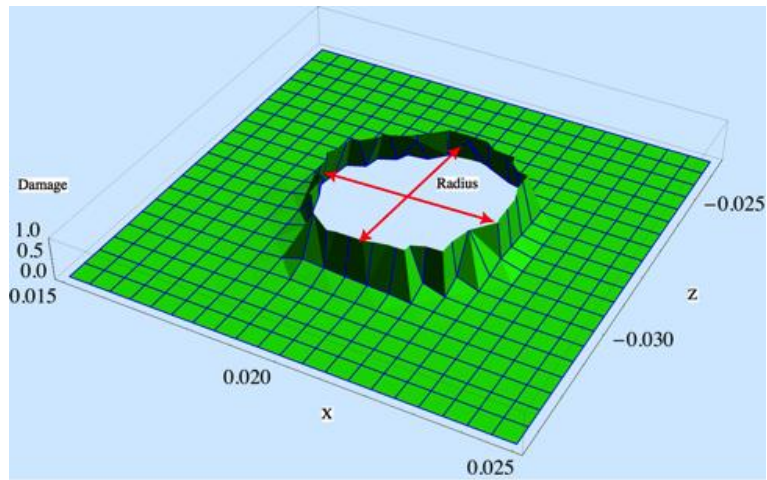
Figure 49: Thermal ablation zone for liver-shape tissue model at 120 s

6.5.3 Comparison of FDM and FEM formulation

At the first stage of validation, two proposed methods based on different discretisation techniques: FDM and FEM are compared. The aim is to test the simulation results from perspective of accuracy and computation efficiency. Therefore, the simulation

condition was set as, power of $Q_{ext} = 7X10^6$ W/m^3 is generated all over the cubic-shape tissue model with the size of 10mm×10mm×10mm for a duration of 120 seconds. While other material parameters and boundary condition is set as the same in Chapter 4. The reason of not choosing points heating as the heating source can be explained as: for FDM model, the introduced heat is actually generated through a minimum volume of mesh element (e$_{v1}$), with the amount of applied heat energy equals to Q_{ext}* e$_{v1}$. For FEM model, applied heat amount equals to Q_{ext}* e$_{v2}$, here e$_{v2}$ stands for the element volume where the heating point is located. Clearly the heat amount introduced through the same heating rate Q_{ext} is not equal. Therefore, corresponding comparison is not reliable for distinguishing two established discretisation methods: FDM and FEM.

The meshed up model contains 1331 nodes and 1000 elements for FDM method (see Figure 9), and 1331 nodes and 6000 elements for FEM method (see Figure 32). Since one test is enough to indicate the difference of two discretisation techniques, the simulation is performed only based on one proposed model: Fourier based thermal mechanical model. Parameters used in this comparison test are as listed in Table 2, and the simulation results of temperature and displacement in three coordinate axes are as illustrated in Figure 50 to Figure 53, which show quite good consistency. Tracing a single point at the centre of input tissue model with simulation duration (see Figure 54 and Figure 55), one can get that the maximum temperature difference for two discretisation methods is less than 2.4%, and maximum displacement difference is less than 4.7%.
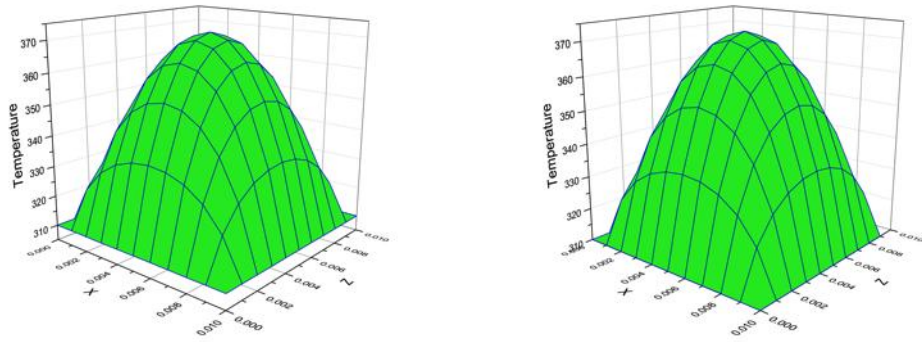
Figure 50: Comparison of temperature distribution between FEM (left) and FDM (right) at 120s
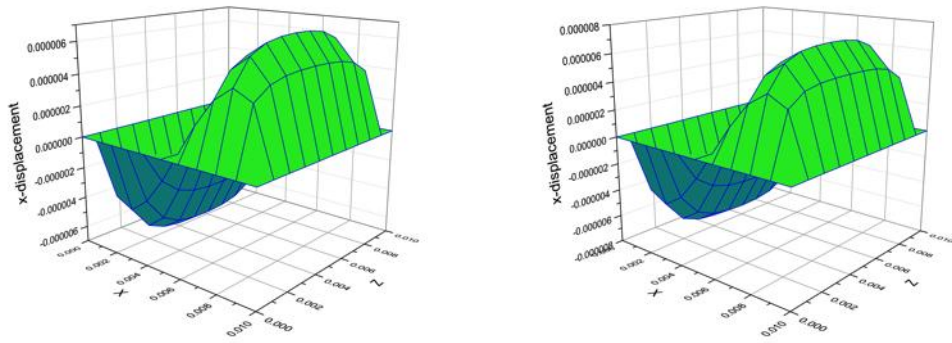
Figure 51: Comparison of x-axis displacement between FEM (left) and FDM (right) at 120s
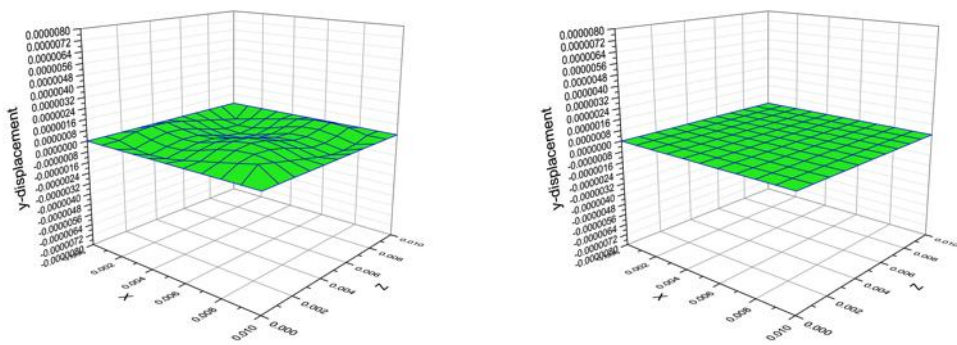
Figure 52: Comparison of y-axis displacement between FEM (left) and FDM (right) at 120s
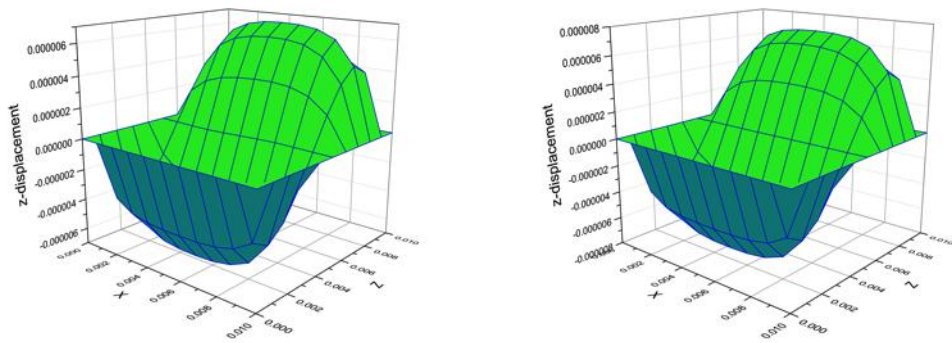
Figure 53: Comparison of z-axis displacement between FEM (left) and FDM (right) at 120s
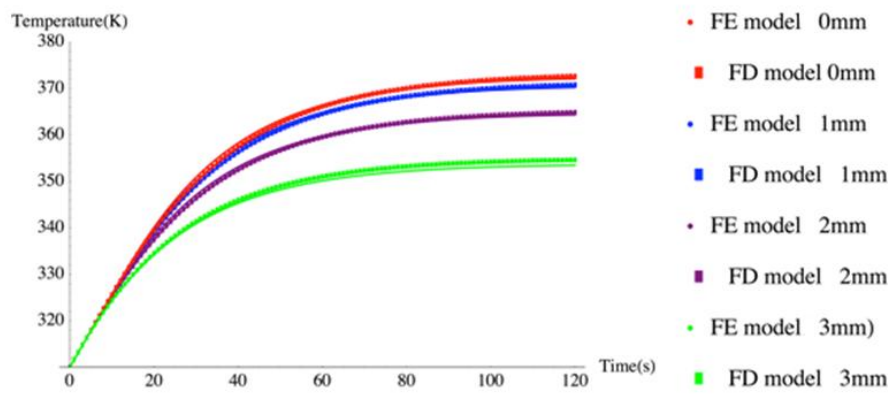
Figure 54: Temperature comparison
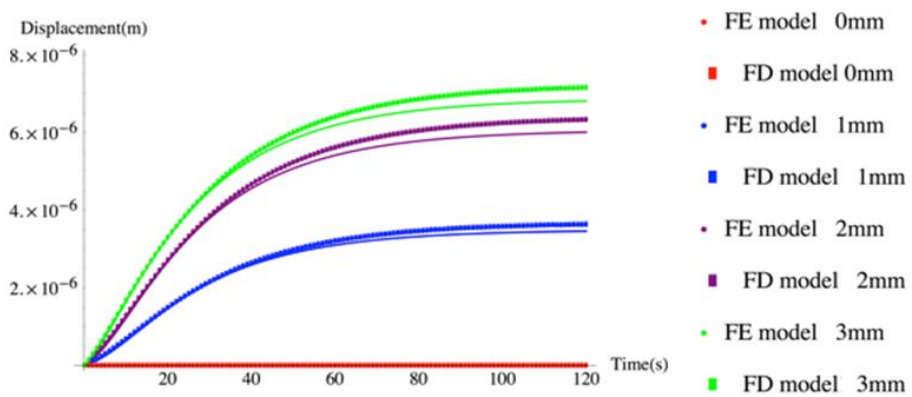
Figure 55: X-axis displacement comparison

101

Comparing computation costs using FDM and FEM methods, the results are as shown in Table 8. It can be obtained that both techniques can support real-time performance (less than 66.6 milliseconds) base on current meshing methods and boundary condition. It has to be mentioned that the computation costs are based on a Gauss-Seidel iterative solver on solving obtained linear system of equations after standard discretisations of governing equations using two numerical methods.

Table 8: Executing time comparison

Process (heating and deformation)	FD/ 729 nodes	FE/ 729 nodes
Single iteration	49-55 milliseconds	54-57 milliseconds

6.5.4   Validation of proposed models

For the second stage of validation, our proposed model: non-Fourier based thermal mechanical model using FEM formulation against commercialized finite element analysis software LISA is performed. Considering there is still no existed and commercialised simulation program that is the same as our built, at this stage of validation, the non-Fourier effects, biological behaviours like: blood perfusion and metabolic heat generation within heated tissue, as well as coupled thermal mechanical influence, are ignored during simulation comparisons. And the validation is performed in two steps: firstly temperature field and then displacement field. Still using the same meshed up cubic-shape tissue model (see Figure 32) and the same simulation scenario as we set in Chapter 4, but here the heating power is applied on single heating point at the centre of cubic-shape tissue model at 0.08 W for duration of 120 seconds. Figure 56 shows the temperature change at mid-plane Y=0.005m at 120s. As we can see, simulation results of our proposed model are in a very good agreement with LISA results, with error less than 0.01%.
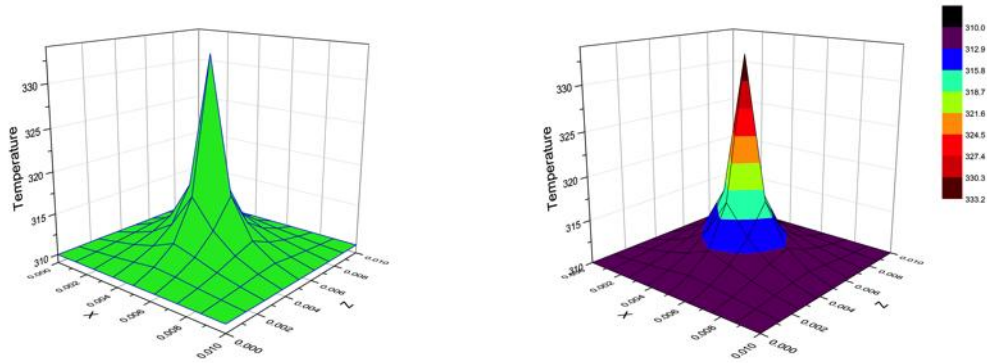
Figure 56: Comparison of temperature distribution between our model (left) and LISA (right) at 120s

Then, proposed non-Fourier thermal mechanical model using FEM formulation which includes all the biological behaviours like: blood perfusion, metabolic heat generation within heated tissue as well as coupled thermal mechanical influence, is further verified in terms of displacement field. To do this, temperature field derived from our established model at the end of heating: 120s is used as the input of third party finite element analysis tool LISA for comparing of generated displacement field. Displacement in three coordinate axes at mid-plane Y=0.005m are as plotted in Figure 57 to Figure 59. One can obtain that simulation results of our proposed model are in very good agreement with results from LISA tool.
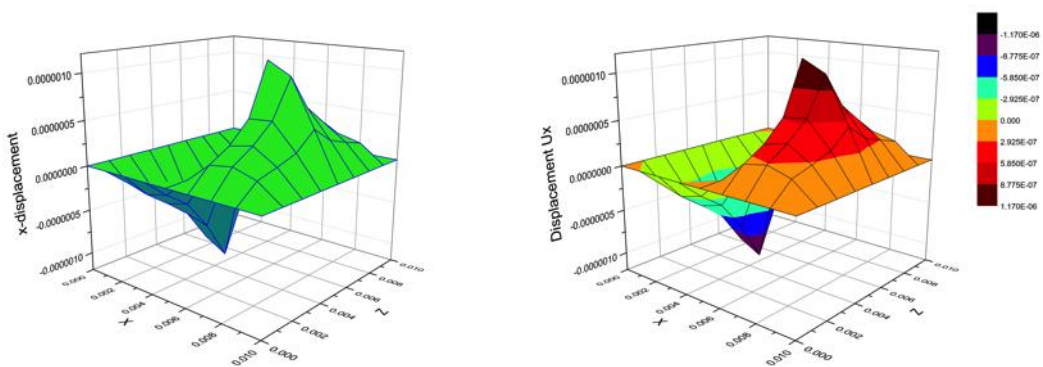
Figure 57: Comparison of displacement in x-axis between our model (left) and LISA (right) at 120s
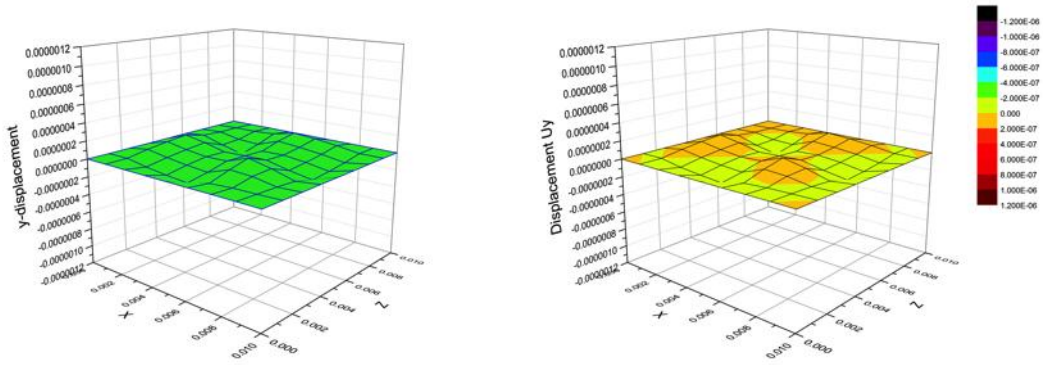
Figure 58: Comparison of displacement in y-axis between our model (left) and LISA (right) at 120s
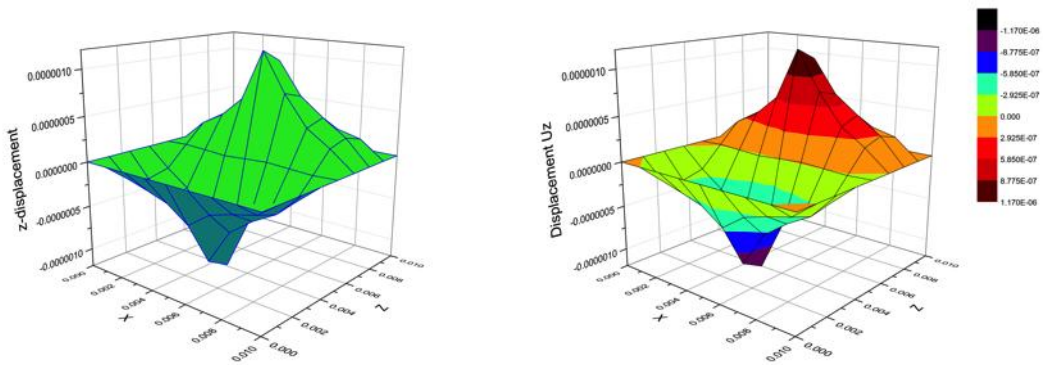
Figure 59: Comparison of displacement in z-axis between our model (left) and LISA (right) at 120s

6.5.5   Validation against experimental results

In this section, the proposed model based on non-Fourier bioheat transfer theory will be further verified by practical experimentation in temperature field. Given the plenty of experimental data on thermal behaviours of soft tissues available in the literature [99, 120, 130-132], the straightforward way is to compare our proposed model with these available experimental data for performance verification purpose.

In terms of frequency used microwave-heating pattern as used in practical thermal ablation treatment, an analytical expression of three dimensional energy distribution is

assumed in the form of Eq. 6-36 [133, 134], which can be applied to estimate the external heating source term Q_{ext} in aforementioned bio-heat transfer equations,

$$Q_{ext}(W/mm^3) = C_t Q \frac{[2\varrho r + (n-2)]e^{-2\varrho r}}{r^n} e^{-z^2/z_0^2}$$

<div align="right">

Eq. 6-35

</div>

where C_t is a scale constant, Q is microwave power, ϱ is an attenuation constant, r is the radial distance from the centre of the antenna, n is a exponential constant, z is the axial distance from the electrode tip, z_0 is the axial decay distance.

Based on the above energy distribution expression, validation of our proposed model in terms of microwave heating source is performed next. The simulation results will be compared with existed experimental data by the work of Wu etc. in [99], to test the efficiency and accuracy of our established model. The simulated porcine liver model in the experiment is shown in Figure 60. To generate heat, a single slot microwave antenna is immersed into the liver cube to a depth of 27 mm. The microwave power used is 40 W with frequency of 2.45 GHz and the initial liver tissue temperature is 293 K. Boundary conditions are set to be convective boundary conditions with the convective heat transfer coefficient of 5 W/(m²K) and the ambient air temperature of 293K. Blood perfusion is assumed to be zero for ex-vivo tissues. Related parameters used in the simulation are as listed in Table 9 [99] [133].
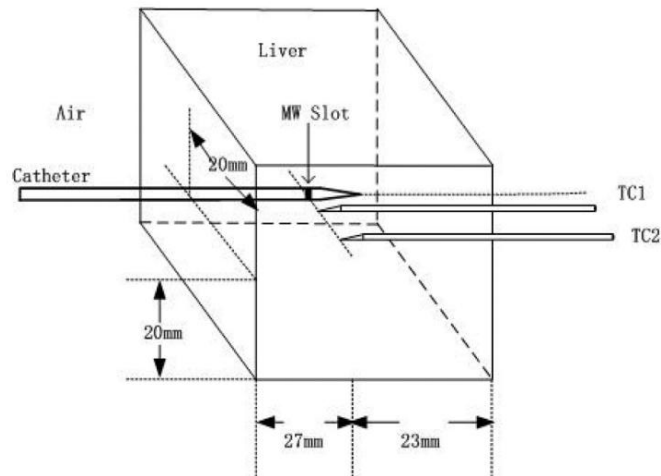
Figure 60: Model geometry in MW heating (Wu et al. [99])

Table 9: Properties of liver tissue and microwave antenna

Parameters	Values
Thermal conductivity k; W/mK	0.465
Specific heat C; J/kgK	3628
Density ρ; kg/m^3	1050
Metabolic heat generation rate Q_m; W/m^3	33800
Characteristic Time τ_p; s	12
Exponential constant;	2.2
Attenuation constant ϱ; mm^{-1}	0.0413
Scale constant C_t; mm$^{-0.8}$	0.00316
Axial decay distance z_0; mm	18.5

Comparison and analysis of heating process is done within the entire 120 seconds of continuing heating. For two selected points with distance of 2mm and 5mm to the heat generation centre, denoted as TC1 and TC2 in Figure 60, several experiments are performed to trace their temperature, as was done by Wu etc. in [99]. After that, the average temperatures vs. time curves are chosen for comparison purpose with their established thermal model which emphasized on temperature dependent biomaterial

properties. Plotting all of the results including Wu's model, experiment data, our Fourier and non-Fourier based thermal mechanical models into the same Figure (see Figure 61), we found that for points located near the heating sources, i.e. TC1, our proposed models and Wu's model all have quite good fitting performance, while our non-Fourier based model has better prediction results at initial stage of heating. For points located further away of heating sources, i.e. TC2, all simulation models have prediction offset, however by introducing relaxation time during bioheat transfer, our non-Fourier based model gives an improved fitting at the beginning of thermal treatment. As the heating duration is approaching the end of simulation, all these presented models, Wu's model, our Fourier and non-Fourier models, have merged at a closed steady state prediction of experiment results.
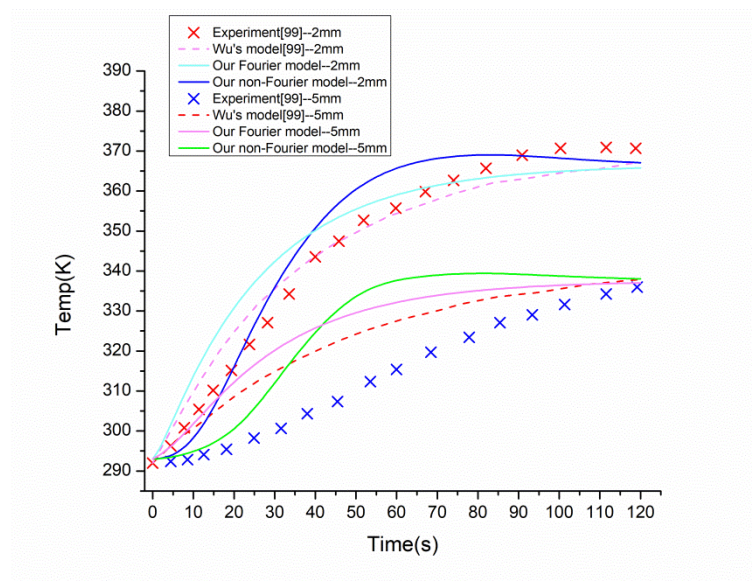
Figure 61: Numerical simulation results vs. experimental data (Wu et al. [99])

6.6   Conclusion

The success of thermal ablation depends strictly on precise prediction of temperature distribution and resulting damage area. A possible non-Fourier nature of soft tissues may play an important role during thermal treatment planning process. In this chapter, we have investigated coupled temperature and deformation field in heated tissue model based on non-Fourier bioheat transfer theory. Still employing presented thermal mechanical damage prediction model in chapter 5, simulation results are compared between Fourier and non-Fourier bioheat transfer based thermal mechanical models. The established mathematical problem has been solved using a FEM scheme to account for irregular tissue geometry, and a condensation method has been used to improve the computational speed. The simulation results demonstrate that the introduced thermal relaxation time in thermal treated biological tissues would delay the peak temperature reaching time at all thermal affected points. Therefore, the non-Fourier based thermal mechanical model is expected to provide more realistic predictions than Fourier based thermal mechanical model in temperature field. Furthermore, deviation in strain, stress and damage field prediction between these two models suggests that non-Fourier behaviour of soft tissue under purely thermal load, together with thermal mechanical influence as discussed in Chapter 5 plays an essential role in thermal ablation simulation, especially for a relatively short duration of heating that is comparable to the thermal relaxation time of target tissue. Regarding the final damage zone prediction that is defined by a provided threshold, the ablation boundary may be varied although a merged temperature may be predicted by two bioheat transfer theories based models after prolonged exposure, attributed to the deviation of predicted temperatures inside tissue body before the steady state is reached.

7 Non-linear thermal mechanical model using FEM

Focusing on a commonly encountered type of soft tissue that is reinforced by collagen fibre bundles, it may also have an anisotropic nature, given that different tissues perform specific functions in the body. Collagen fibre bundles are oriented in different directions, according to the function of the tissue [73]. For example, artery tissue has fibre bundles arranged in the axial-circumferential polar plane to limit inflectional and axial deformation. Therefore, a constitutive model characterising this kind of soft tissue must take into accounts both material symmetry and degree of anisotropy.

Further, under purely thermal induced tissue deformation, the above chapters focused on linear range of strain-stress relationship characterisation, which is a reasonable choice for related thermal treatment. However, in practical application of thermal therapy, even small movement of operation tool/device for delivering heat can generate strain out of linear limit. In some applications, such external mechanical loading is even designed to come with thermal loading, for instance, an indenter heating of skin tissue to cure its disease [16]. To account for such influence, in this chapter our research will move on to nonlinear range characterization of soft tissue response under combined thermal and mechanical loads.

Based on the method of multiplicative decomposition of thermal mechanical deformation gradient, the above chapters have given the formulation of corresponding constitutive model and heat transfer equations. In this Chapter, the formulation is focused on the nonlinear and anisotropic features of soft tissues by assuming: the tissue body is a type of thermally isotropic and elastically anisotropic nonlinear material; and the anisotropic state of target biomaterial remains the same during thermal expansion

and mechanical deformation. Subsequently, the established mathematical model under thermal and mechanical loads would be coded into a self developed computer program using FEM and total Lagrangian formulations.

7.1   Nonlinear thermal mechanical model

7.1.1   Material symmetry

The symmetry group R' of a material is a set of all orthogonal mappings which preserve the material symmetry [135]. For anisotropic materials, the symmetry group R' can be defined with the aid of the so-called structural tensors $\mathbf{L}_i$, with $i = 1,2,3 \dots, n$, as the following,

$$R'\left(\mathbf{Q}\mathbf{L}_i\mathbf{Q}^\mathrm{T}\right) = R'(\mathbf{L}_i)$$

<div align="right">Eq. 7-1</div>

where $\mathbf{Q}$ is any orthogonal transformation that can satisfy the above condition of material symmetry, written in terms of the strain energy function for anisotropic materials, the symmetry group Ψ_e is expressed as,

$$\Psi_e\left(\mathbf{Q}\mathbf{C}_e\mathbf{Q}^\mathrm{T}, \mathbf{Q}\mathbf{L}_i\mathbf{Q}^\mathrm{T}\right) = \Psi_e(\mathbf{C}_e, \mathbf{L}_i)$$

<div align="right">Eq. 7-2</div>

To represent a material symmetry with respect to selected direction l_i, the structural tensor: $\mathbf{L}_i$ can be defined by the following [135],

$$\mathbf{L}_i = l_i \otimes l_i$$

<div align="right">Eq. 7-3</div>

To satisfy Eq. 7-2 for anisotropic materials, strain energy should be a function of five invariants as follows [135]:

$$\Psi_e = \Psi_e(I_1, I_2, I_3, I_4, I_5)$$

$$I_1 = tr(\mathbf{C}_e), \qquad I_2 = \frac{1}{2}\left(I_1^2 - tr(\mathbf{C}_e^2)\right), \qquad I_3 = det(\mathbf{C}_e) = J^2$$

$$I_{4i} = \mathbf{L}_i : \mathbf{C}_e, \qquad I_{5i} = \mathbf{L}_i : \mathbf{C}_e^2$$

<div align="right">**Eq. 7-4**</div>

where $tr(\mathbf{C}_e) = tr(\mathbf{F}_e^T \mathbf{F}_e)$, $\mathbf{F}_e$ is the elastic deformation gradient, $J = det(\mathbf{F}_e)$ denotes the Jacobian.

7.1.2 Modified Neo-Hookean free energy function

Suppose that free energy of collagen fibre bundles reinforced soft tissues, such as arterial tissue and human skin, can be estimated as a thermodynamic model for pseudoelasticity, therefore an anisotropic nonlinear thermoelastic constitutive model is proposed in this chapter. Formulation of this constitutive model using multiplicative decomposition method of thermal mechanical deformation gradient will be conducted in the subsequent section.

Treating soft tissues as composites composed of ground substance reinforced with stiffer collagen fibre bundles, it is common to decompose the strain energy densities modelling into an isotropic part which estimates the behaviour of ground substance [17] and an anisotropic part which includes the effect of reinforcement [74, 75]. Using this decomposition, the strain energy function of anisotropic biomaterials can be represented as:

$$\Psi_e = \Psi_e^{iso}(I_1, I_2, I_3) + \Psi_e^{fiber}(I_{4i}, I_{5i})$$

<div align="right">Eq. 7-5</div>

Also, as experimental evidences indicate, soft tissues can be considered as compressible materials with effective Poisson's ratio ranges from 0.3 to 0.5 [88]. Therefore, applying compressible Neo-Hookean strain energy function to estimate the isotropic part of anisotropic tissue materials, we develop the following anisotropic thermoelastic free energy density model in unit volume,

$$\Psi_e = \rho_\theta \psi_e = \frac{\mu}{2}(I_1 - 3) - \mu \ln J + \frac{\lambda}{2}(\ln J)^2 + \Psi_e^{fiber}$$

<div align="right">Eq. 7-6</div>

where Ψ_e^{fiber} stands for the stored energy of collagen fibre bundles per unit volume.

7.1.3 Anisotropic modelling with collagen fibre bundles

Representing stored energy of collagen fibre bundles during thermal mechanical loadings, the free-energy term Ψ_e^{fiber} as shown in our proposed model uses a distributed collagen fibre bundles orientation as in [18, 136, 137]. Suppose that the biomaterial consists of an isotropic ground substance and embedded in families of fibre bundles characterized by one preferred direction in the reference configuration, defined as $\boldsymbol{a}_{0i}$ in terms of unit vector, we have the forms [137],

$$\Psi_e^{fiber} = \frac{k_1}{2k_2}\{exp[k_2(I_{4i} - 1)^2] - 1\}$$

<div align="right">Eq. 7-7</div>

$$I_{4i} = \mathbf{L}_i : \mathbf{C}_e = tr(\mathbf{F}_e^T \mathbf{F}_e \boldsymbol{a}_{0i} \otimes \boldsymbol{a}_{0i})$$

<div align="right">Eq. 7-8</div>

We remark that k_1 and k_2 are positive material constants which can be determined from experiments. It need be noted that the fibre bundle direction is defined as $l_i = \{cos\,\theta, sin\,\theta, 0\}$, if we suppose it is in xy plane and oriented with angle θ to the x-axis. Taking the arterial tissue for example, when we design the longitudinal direction is along y-axis and circumferential plane is parallel to xz plane, the absolute value of the angle between the fibre bundle direction and circumferential direction greater than 45° shows that the fibre bundle are closer to the longitudinal direction than circumferential direction [138]. This indicates that the target tissue should be stiffer in the longitudinal than circumferential direction.

7.1.4   Stress response

Using the multiplicative decomposition method, the thermal mechanical deformation gradient can be decomposed into its elastic and thermal parts as discussed in Chapter 2,

$$\mathbf{F} = \mathbf{F}_e \cdot \mathbf{F}_\theta$$

<div align="right">Eq. 7-9</div>

For thermally isotropic materials, the deformation gradient caused by thermal load can be simplified as,

$$\mathbf{F}_\theta = \varsigma(\theta)\mathbf{I}$$

<div align="right">Eq. 7-10</div>

Assuming $\alpha(\theta)$ to be the coefficient of thermal expansion at temperature θ [113],

$$\varsigma(\theta) = exp\left[\int_{\theta_0}^{\theta} \alpha(\theta)\, d\theta\right]$$

<div align="right">Eq. 7-11</div>

113

As from the derivations in Chapter 2, the second Piola-Kirchhoff stress tensor $\mathbf{S}_e$ and $\mathbf{S}$ are given as,

$$\mathbf{S}_e = \mathbf{F}_e^{-1}\frac{\partial(\rho_\theta\psi_e)}{\partial\mathbf{F}_e}$$

$$= [\lambda(\theta)\ln J - \mu(\theta)]\mathbf{F}_e^{-1}\mathbf{F}_e^{-T} + \mu(\theta)\mathbf{I}$$

$$+ 2k_1(I_{4i} - 1)exp[k_2(I_{4i} - 1)^2](\boldsymbol{a}_{0i} \otimes \boldsymbol{a}_{0i})$$

$$\mathbf{S} = (det\mathbf{F}_\theta)\mathbf{F}_\theta^{-1} \cdot \frac{\partial(\rho_\theta\psi_e)}{\partial\mathbf{E}_e} \cdot \mathbf{F}_\theta^{-T} = (det\mathbf{F}_\theta)\mathbf{F}_\theta^{-1} \cdot \mathbf{S}_e \cdot \mathbf{F}_\theta^{-T}$$

Recalling $\boldsymbol{F} = \boldsymbol{F}_e\boldsymbol{F}_\theta$, by substituting $\boldsymbol{F}_e = \boldsymbol{F}\boldsymbol{F}_\theta^{-1}$ and Eq. 7-10 into Eq. 7-12 and Eq. 7-13, finally it yields,

$$\mathbf{S} = \varsigma^3(\theta)[\lambda(\theta)\ln J - \mu(\theta)]\mathbf{F}^{-1}\mathbf{F}^{-T} + \varsigma(\theta)\mu(\theta)\mathbf{I}$$

$$+ 2\varsigma(\theta)k_1(I_{4i} - 1)exp[k_2(I_{4i} - 1)^2](\boldsymbol{a}_{0i} \otimes \boldsymbol{a}_{0i})$$

with J and I_i being expressed as,

$$J = \frac{1}{\varsigma(\theta)}det\ (\mathbf{F})$$

$$I_{4i} = \frac{1}{\varsigma(\theta)^2}tr(\mathbf{F}^T\mathbf{F}\boldsymbol{a}_{0i} \otimes \boldsymbol{a}_{0i})$$

If we adopt the following approximation for $\varsigma(\theta)$,

$$\varsigma(\theta) = 1 + a(\theta - \theta_0)$$

The expression in Eq. 7-14 can be simplified as the following if the lame parameters are assumed to be constants,

$$\mathbf{S} = [\lambda \ln J - \mu]\mathbf{F}^{-1}\mathbf{F}^{-T} + \mu\mathbf{I} + 2k_1(I_{4i} - 1)exp[k_2(I_{4i} - 1)^2](\boldsymbol{a}_{0i} \otimes \boldsymbol{a}_{0i})$$
$$+ 2k_1\alpha(\theta - \theta_0)(I_{4i} - 1)exp[k_2(I_{4i} - 1)^2](\boldsymbol{a}_{0i} \otimes \boldsymbol{a}_{0i})$$
$$- 3\alpha(\theta - \theta_0)[\mu - \lambda \ln J]\mathbf{F}^{-1}\mathbf{F}^{-T} + \alpha[\theta - \theta_0]\mu\mathbf{I}$$

with J and I_i being simplified as,

$$J = \frac{1}{1 + a(\theta - \theta_0)} det\ (\mathbf{F})$$

$$I_{4i} = \frac{1}{1 + 2a(\theta - \theta_0)} tr(\mathbf{F}^T\mathbf{F}\boldsymbol{a}_{0i} \otimes \boldsymbol{a}_{0i})$$

7.2   Governing equations

7.2.1   Non-rigid mechanics of motion

Appling the law of the non-rigid mechanics of motion, which can be written as,

$$\rho\ddot{\boldsymbol{u}} = \boldsymbol{F}_{int} + \rho\boldsymbol{b} + \boldsymbol{F}_{ext}$$

where $\boldsymbol{u}$ is the displacement vector, $\boldsymbol{F}_{int}$ is the internal force, and $\boldsymbol{b}$ is the specific body force, $\boldsymbol{F}_{ext}$ is the external force.

7.2.2　Bioheat transfer

The Fourier and non-Fourier form of bioheat transfer equations including thermoelastic effect can be described in Eq. 7-22 and Eq. 7-23,

$$\rho C \frac{\partial T}{\partial t} + \beta T_0 \frac{\partial (\boldsymbol{\nabla} \cdot \boldsymbol{u})}{\partial t} = k\boldsymbol{\nabla}^2 T + C_b \omega_b \rho_b (T_b - T) + Q_m + Q_{ext}$$

<div align="right">Eq. 7-22</div>

$$\tau_p \rho C \frac{\partial^2 T}{\partial t^2} + \left(\tau_p C_b \omega_b \rho_b + \rho C\right)\frac{\partial T}{\partial t} + \tau_p \beta T_0 \frac{\partial^2 (\boldsymbol{\nabla} \cdot \boldsymbol{u})}{\partial t^2} + \beta T_0 \frac{\partial (\boldsymbol{\nabla} \cdot \boldsymbol{u})}{\partial t}$$

$$= k\boldsymbol{\nabla}^2 T + \tau_p \frac{\partial Q_m}{\partial t} + \tau_p \frac{\partial Q_{ext}}{\partial t} + C_b \omega_b \rho_b (T_b - T) + Q_m + Q_{ext}$$

<div align="right">Eq. 7-23</div>

7.3　FEM formulation

7.3.1　Weak form

Step 1: On discretising bioheat transfer models using finite element scheme, the temperature field within an individual element (e) is approximated in terms of shape functions,

$$T^{(e)}(x, y, z) = N_{,}\{T_{,}\}$$

<div align="right">Eq. 7-24</div>

Here, $T_{,}$ is the temperature vector at each element node. The shape function $N_{,}$ is function of space variables. And the integrated form of bioheat transfer governing equations as expressed in Eq. 7-22 and Eq. 7-23 over an individual element (e) is obtained by applying Galerkin's weighted residual method as following, where $N_{,,}$ is used as the weighting factors [129], with $N_{,,} = [N_{,}]^T$,

$$\int_{V(e)} \left(\rho C \frac{\partial T}{\partial t} + \beta T_0 \frac{\partial (\boldsymbol{\nabla} \cdot \boldsymbol{u})}{\partial t} - k\boldsymbol{\nabla}^2 T - C_b \omega_b \rho_b (T_b - T) - Q_m - Q_{ext} \right) N_{,,} dV = 0$$

$$\int_{V(e)} \left(\tau_p \rho C \frac{\partial^2 T}{\partial t^2} + \left(\tau_p C_b \omega_b \rho_b + \rho C \right) \frac{\partial T}{\partial t} + \tau_p \beta T_0 \frac{\partial^2 (\boldsymbol{\nabla} \cdot \boldsymbol{u})}{\partial t^2} + \beta T_0 \frac{\partial (\boldsymbol{\nabla} \cdot \boldsymbol{u})}{\partial t} - k\boldsymbol{\nabla}^2 T \right.$$

$$\left. - \tau_p \frac{\partial Q_m}{\partial t} - \tau_p \frac{\partial Q_{ext}}{\partial t} - C_b \omega_b \rho_b (T_b - T) - Q_m - Q_{ext} \right) N_{,,} dV$$

$$= 0$$

The integrated form of Eq. 7-25 and Eq. 7-26 can be rearranged in the following,

$$\left(\int_{V(e)} \rho C N_{,,} N_{,} dV \right) \dot{\theta}$$

$$+ \left(\int_{V(e)} k \frac{\partial N_{,,}}{\partial x} \frac{\partial N_{,}}{\partial x} dV + \int_{V(e)} k \frac{\partial N_{,,}}{\partial y} \frac{\partial N_{,}}{\partial y} dV \right.$$

$$+ \left. \int_{V(e)} k \frac{\partial N_{,,}}{\partial z} \frac{\partial N_{,}}{\partial z} dV \right) \theta + \left(\int_{V(e)} C_b \omega_b \rho_b N_{,,} N_{,} dV \right) \theta$$

$$+ \left(\int_{V(e)} \beta T_0 \frac{\partial N_{,,}}{\partial x} N_{,} dV \right) \dot{u} + \left(\int_{V(e)} \beta T_0 \frac{\partial N_{,,}}{\partial y} N_{,} dV \right) \dot{v}$$

$$+ \left(\int_{V(e)} \beta T_0 \frac{\partial N_{,,}}{\partial z} N_{,} dV \right) \dot{n}$$

$$= \int_{V(e)} (Q_m + Q_{ext}) N_{,,} dV - \int_{A(e)} (q_i n_i) N_{,,} dA$$

$$\left(\int_{V(e)} \tau_p \rho C N_{,,} N_{,} \, dV \right) \ddot{\theta} + \left(\int_{V(e)} \left(\tau_p C_b \omega_b \rho_b + \rho C \right) N_{,,} N_{,} \, dV \right) \dot{\theta}$$

$$+ \left(\int_{V(e)} k \frac{\partial N_{,,}}{\partial x} \frac{\partial N_{,}}{\partial x} \, dV + \int_{V(e)} k \frac{\partial N_{,,}}{\partial y} \frac{\partial N_{,}}{\partial y} \, dV \right.$$

$$+ \left. \int_{V(e)} k \frac{\partial N_{,,}}{\partial z} \frac{\partial N_{,}}{\partial z} \, dV \right) \theta + \left(\int_{V(e)} C_b \omega_b \rho_b N_{,,} N_{,} \, dV \right) \theta$$

$$+ \left(\int_{V(e)} \tau_p \beta T_0 \frac{\partial N_{,,}}{\partial x} N_{,} dV \right) \ddot{u}_x + \left(\int_{V(e)} \tau_p \beta T_0 \frac{\partial N_{,,}}{\partial y} N_{,} dV \right) \ddot{v}$$

$$+ \left(\int_{V(e)} \tau_p \beta T_0 \frac{\partial N_{,,}}{\partial z} N_{,} dV \right) \ddot{n} + \left(\int_{V(e)} \beta T_0 \frac{\partial N_{,,}}{\partial x} N_{,} dV \right) \dot{u}$$

$$+ \left(\int_{V(e)} \beta T_0 \frac{\partial N_{,,}}{\partial y} N_{,} dV \right) \dot{v} + \left(\int_{V(e)} \beta T_0 \frac{\partial N_{,,}}{\partial z} N_{,} dV \right) \dot{n}$$

$$= \int_{V(e)} \left(\tau_p \frac{\partial Q_m}{\partial t} + \tau_p \frac{\partial Q_{ext}}{\partial t} + Q_m + Q_{ext} \right) N_{,,} \, dV$$

$$- \int_{A(e)} (q_i n_i) N_{,,} dA$$

<div align="right">**Eq. 7-28**</div>

Step 2: For discretisation of the dynamic system model in finite element scheme, displacement components within an individual element (e) are approximated in terms of the same shape functions as used for temperature field approximation.

$$u_i^{(e)}(x, y, z) = N_{,} \{U_i\}$$

<div align="right">**Eq. 7-29**</div>

Similarly, using the same the weighting functions $N_{,,}$, the formal Galerkin approximation of motion dynamic governing equation is as,

<div align="right">118</div>

$$\int_{V(e)} N_{,,}(\rho\ddot{\boldsymbol{u}} - \boldsymbol{F}_{int} - \rho\boldsymbol{b} - \boldsymbol{F}_{ext})dV = 0$$

To determine the second term in the above equation $\boldsymbol{F}_{int}$, the total potential energy generated inside deformed material can be written in the following equivalent form,

$$\int_{V(e)} \frac{1}{2}\{\boldsymbol{\epsilon}\}^T\{\boldsymbol{s}\}\, dV = \int_{V(e)} \boldsymbol{F}_{int}^T\{\boldsymbol{u}\}dV$$

while the strain and stress vector in the above equation can be written as,

$$\{\boldsymbol{\epsilon}\} = \{E_{11}, E_{22}, E_{33}, 2E_{12}, 2E_{23}, 2E_{13}\} = [\boldsymbol{B}]\{\boldsymbol{u}\}$$

$$\{\boldsymbol{s}\} = \{S_{11}, S_{22}, S_{33}, 2S_{12}, 2S_{23}, 2S_{13}\} = [\boldsymbol{D}][\boldsymbol{B}]\{\boldsymbol{u}\}$$

with $[\boldsymbol{B}]$ as the strain displacement matrix, $[\boldsymbol{D}]$ as material stiffness matrix.

Also, from our established nonlinear thermal mechanical model, the expression of second Piola-Kirchhoff stress tensor and Green-Lagrange strain are in the following forms,

$$\begin{aligned}
S_{ij} = {}& [\lambda\, lnJ - \mu]\mathrm{F}_{ij}^{-1}\mathrm{F}_{ij}^{-T} + \mu\mathbf{I} + 2k_1(I_{4i} - 1)exp[k_2(I_{4i} - 1)^2](\boldsymbol{a}_{0i} \otimes \boldsymbol{a}_{0i}) \\
& + 2k_1\alpha(\theta - \theta_0)(I_{4i} - 1)exp[k_2(I_{4i} - 1)^2](\boldsymbol{a}_{0i} \otimes \boldsymbol{a}_{0i}) \\
& - 3\alpha(\theta - \theta_0)[\mu - \lambda\, lnJ]\mathrm{F}_{ij}^{-1}\mathrm{F}_{ij}^{-T} + \alpha[\theta - \theta_0]\mu\mathbf{I}
\end{aligned}$$

$$E_{ij} = \frac{1}{2}\left(F_{ij}^T F_{ij} - I_{ij}\right) = \frac{1}{2}\left(\left(u_{i,j} + \delta_{ij}\right)^T \left(u_{i,j} + \delta_{ij}\right) - I_{ij}\right)$$

$$= \frac{1}{2}\left(\left(u_{i,j}\right) + \left(u_{i,j}\right)^T + \left(u_{i,j}\right)^T \left(u_{i,j}\right)\right)$$

<div align="right">Eq. 7-35</div>

Substituting Eq. 7-32 and Eq. 7-33 into Eq. 7-31, it can be rewritten as,

$$\int_{V(e)} \frac{1}{2}\{u\}^T [B]^T [D][B]\{u\}dV = \int_{V(e)} F_{int}^T \{u\}dV$$

<div align="right">Eq. 7-36</div>

$$\int_{V(e)} [B]^T [D][B]\{u\}\, dV = \int_{V(e)} F_{int}^T \{u\}dV$$

<div align="right">Eq. 7-37</div>

Since we have $[D][B]\{u\} = \{s\}$, by referring to variation of potential energy in both sides of Eq. 7-37 to displacement vector u, yields,

$$\int_{V(e)} [B]^T \{s\}\, dV = \int_{V(e)} F_{int}\, dV$$

<div align="right">Eq. 7-38</div>

Therefore, the integrated form to determine internal force can be written as,

$$\int_{V(e)} N_{,,} F_{int}\, dV = \int_{V(e)} N_{,,} [B]^T \{s\}\, dV$$

<div align="right">Eq. 7-39</div>

where,

$$N_{,,} = [N_{,}]^T$$

<div align="right">Eq. 7-40</div>

Then, Eq. 7-39 can be written as,

$$\int_{V(e)} N_{,I} \boldsymbol{F}_{int} \, dV = \int_{V(e)} N_{,I}^T [\boldsymbol{B}]^T \{\boldsymbol{s}\} \, dV$$

Introducing the following expressions from Eq. 7-42 to Eq. 7-44 while applying four node linear tetrahedral element,

$$[\boldsymbol{B}_0] = [\boldsymbol{B}][N_{,I}]$$

$$[\boldsymbol{B}_0] = \{B_0^1 \quad B_0^2 \quad \dots \quad B_0^k\}, k = 4$$

$$[B_0^k] = \begin{bmatrix} F_{11}N_{Ik,x} & F_{21}N_{Ik,x} & F_{31}N_{Ik,x} \\ F_{12}N_{Ik,y} & F_{22}N_{Ik,y} & F_{32}N_{Ik,y} \\ F_{13}N_{Ik,z} & F_{23}N_{Ik,z} & F_{33}N_{Ik,z} \\ F_{11}N_{Ik,y} + F_{12}N_{Ik,x} & F_{21}N_{Ik,y} + F_{22}N_{Ik,x} & F_{31}N_{Ik,y} + F_{32}N_{Ik,x} \\ F_{12}N_{Ik,z} + F_{13}N_{Ik,y} & F_{22}N_{Ik,z} + F_{23}N_{Ik,y} & F_{32}N_{Ik,z} + F_{33}N_{Ik,y} \\ F_{11}N_{Ik,z} + F_{13}N_{Ik,x} & F_{21}N_{Ik,z} + F_{23}N_{Ik,x} & F_{31}N_{Ik,z} + F_{33}N_{Ik,x} \end{bmatrix}$$

Hence, Eq. 7-41 can be further written as,

$$\int_{V(e)} N_{,I} \boldsymbol{F}_{int} \, dV = \int_{V(e)} [\boldsymbol{B}_0]^T \{\boldsymbol{s}\} \, dV$$

For applied four node linear tetrahedral elements we also have,

$$\int_{V(e)} [\boldsymbol{B}_0]^T \{\boldsymbol{s}\} \, dV = V(e)[\boldsymbol{B}_0]^T \{\boldsymbol{s}\}$$

121

Step 3: Combining these two discretisations: temperature field and thermal mechanical deformation field as they are coupled, one can get the discrete equilibrium equation for each element in question. Integrating each component and assembling all included elements under consideration, finally one will get a global characteristic equation for all mesh points, expressed in a matrix form as follows. From which, the temperature and displacement components, as well as the external heating source and applied force are all related.

$$M\underline{\ddot{u}} + C\underline{\dot{u}} + K\underline{u} = F$$

$$\underline{u} = \begin{Bmatrix} \theta \\ u \end{Bmatrix}$$

where M is the global mass matrix, C is the global damping matrix, $\underline{u}$ is combined temperature and displacement vector, K is the stiffness matrix and F is the total external force.

Step 4: Recalling thermal mechanical damage prediction model as in Eq. 5-7 to determine the final tissue damage based on the above established model, here the term $\acute{E}_{TM}$ is expressed as,

$$\acute{E}_{TM} = \frac{1}{2} V_{mol} \sum_{i=1,j=1}^{3} \left(s_{ij} \epsilon_{ij} \right)$$

As described in Chapter 5, in order to calculate stored energy from Eq. 7-34 and Eq. 7-35, the stress expression is readjusted by taking out the terms related to $(\theta - \theta_0)$ in

Eq. 7-34, considering only stored strain energy based on resultant tissue deformation is the key influence factor of our proposed thermal mechanical damage model, as expressed in Eq. 5-7.

7.3.2 Total Lagrangian explicit dynamics

Despite the large number of time steps needed for the explicit method, it is often more efficient than the implicit method, particularly when many expensive Newton-Raphson iterations are needed to solve inversion of varied stiffness matrix using implicit scheme.

Different from Chapter 4 and 6 where linear isotropic biomaterial is assumed, in this chapter, anisotropic nonlinear tissue model is concerned. Therefore, constant stiffness matrix cannot be derived from applied numerical method, thus, the computation speeding method based on implicit time scheme is not suitable in this chapter. But still allowing for efficient computation as required for many large-scale finite element models of biomaterials, total Lagrangian explicit dynamics (TLED) [87] that based on explicit time integration method, is chosen for spatially and temporally discretisations of the governing equations. Also, a Gauss-Seidel iterative solver is employed on solving obtained linear system of equations as shown in the following forms,

$$\boldsymbol{M}\left(\frac{\underline{\boldsymbol{u}}_{t+\Delta t} - 2\underline{\boldsymbol{u}}_t + \underline{\boldsymbol{u}}_{t-\Delta t}}{\Delta t^2}\right) + \boldsymbol{C}\left(\frac{\underline{\boldsymbol{u}}_{t+\Delta t} - \underline{\boldsymbol{u}}_{t-\Delta t}}{2\Delta t}\right) + \boldsymbol{K}\underline{\boldsymbol{u}}_t = \boldsymbol{F}_{t+\Delta t}$$

<div align="right">Eq. 7-50</div>

or,

$$\left(\frac{\boldsymbol{M}}{\Delta t^2} + \frac{\boldsymbol{C}}{2\Delta t}\right)\underline{\boldsymbol{u}}_{t+\Delta t} = \left(2\frac{\boldsymbol{M}}{\Delta t^2} - \boldsymbol{K}\right)\underline{\boldsymbol{u}}_t - \left(\frac{\boldsymbol{M}}{\Delta t^2} - \frac{\boldsymbol{C}}{2\Delta t}\right)\underline{\boldsymbol{u}}_{t-\Delta t} + \boldsymbol{F}_{t+\Delta t}$$

<div align="right">Eq. 7-51</div>

with,

$$Ku_t = \sum_i \int_{V(i)} [B_0]_t^T \{s_t\} \, dv$$

where Δt is the time step, B_0 is the strain displacement matrix, $\{s\}$ is the second Piola-Kirchoff stress vector and $V(i)$ is the ith element volume. In this thesis, the damping matrix is assumed to be proportional to the mass matrix calculated as a linear function of the global mass matrix as follows: $C = \zeta M$, where ζ is a scaling factor. This ensures that the global damping matrix is diagonal which is needed for elemental level computations to avoid complex matrix inversion in explicit integration of the system dynamics [139].

The following gives the detailed computing steps while using TLED method,

1. Load mesh and boundary conditions.

2. Pre-computation preparation by storing the inverse of (constant) matrix $\left(\frac{M}{\Delta t^2} + \frac{C}{2\Delta t} \right)$.

3. Obtain element nodal temperature and displacements $\underline{u}$ at time t and $t - \Delta t$.

4. Compute temperature and deformation gradient F, right Cauchy-Green deformation tensor C and invariants J and I_i.

5. Calculate full strain displacement matrix B_0.

6. Compute second Piola Kirchoff stress (vector) s.

7. Compute $K\underline{u}_t$ at time t.

8. Apply load: heating source and external force F at $t + \Delta t$.

9. Compute temperature and displacements $\underline{u}$ at time $t + \Delta t$ using the explicit time

integration formula.

10. Loop step 3 to 9 for the next time step.

7.4   Convergence testing

Figure 62 shows the number of Gauss-Seidel solver iterations against the margin of error for a typical simulation of nonlinear thermal mechanical interaction using FEM method. Similar conclusion can be derived as smaller margins of error allow for greater accuracy of computation results but requires a larger number of solver iterations. Meanwhile, approximately the same number of iterations is needed for the same level of convergence to be reached for nonlinear based FEM model and linear based FEM model, see Figure 31.
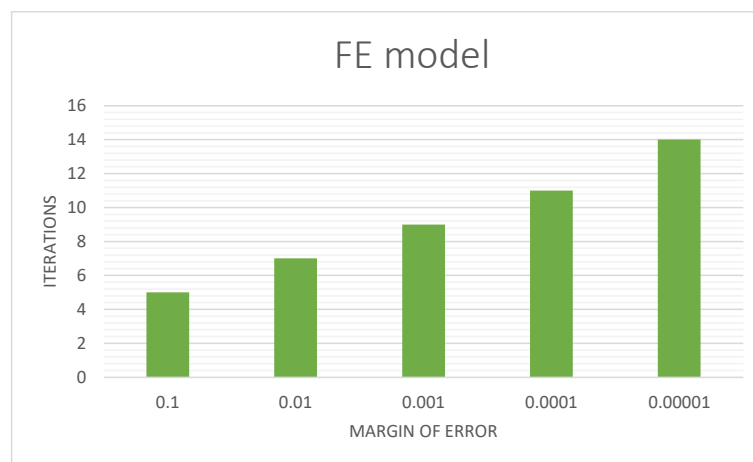
Figure 62: Number of iterations vs. margin of error for nonlinear FE model

7.5 Results and discussion

7.5.1 Validation of proposed model

In this section, proposed model in nonlinear regime: nonlinear thermal mechanical model using FEM formulation is verified in terms of displacement field, considering the temperature fields based Fourier and non-Fourier bioheat transfer theories have been validated in section 6.4.4 and 6.4.5 against commercialised analysis tool LISA and experimental data.

For a particular type of soft tissue, arterial tissue, to fit our established non-linear thermal mechanical model with experimental data in [75], Nolan et al. demonstrated that the effective Poisson's ratio of the arterial tissue ranges from 0.412 to 0.469 [140], which indicates that the material is indeed compressible. Therefore, the biomaterial parameters with the best fit are chosen as $\mu = 12.71\,\text{kPa}$, $k = 101.68\,\text{kPa}$, while the embedded two families of fibre bundles parameters are: $k_1 = 2.3632\,\text{kPa}$, $k_2 = 0.8393\,\text{Pa}$ and the angle between the two fibre bundles direction and the stretching direction is $\pm 43.39°$. Figure 63 illustrates the Cauchy stress versus strain curves of our proposed model at constant temperature, experiment data and presented model in [75]. As can be seen, the applied anisotropic constitutive model based on Neo-Hookean model as used in our proposed nonlinear thermal mechanical model has a quite good fitting with experiment data in literature.
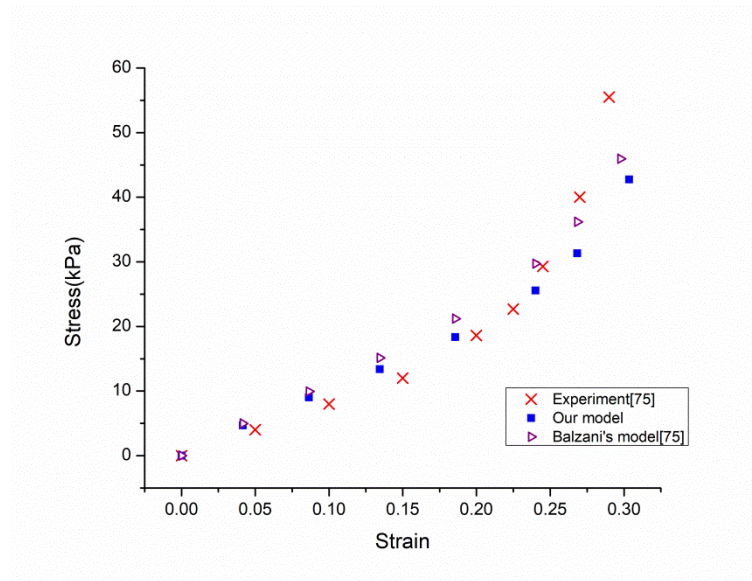
Figure 63: Cauchy stress vs. strain curves of our model and experiment data (Balzani et al. [75])

7.5.2 Heating and stretching pattern

Consider a soft tissue sample in a cubic shape with size of 0.1m×0.1m×0.1m (see Figure 64), which is discretised into uniform meshes using 3072 tetrahedron elements and 729 nodes. The simulation condition is set as, the model's top face is free to move and the other faces are kept constrained. Both stretching and heating loads are applied to the top face of the cubic-shape sample at a single point, while the temperatures on all boundary surfaces are kept constant (310K). The initial temperature of the tissue sample is 310K. In addition, we assume there is a single family of parallel fibre bundle aligned with the reference unit vector $\boldsymbol{a}_{0i}$ in the XY plane, oriented with angle θ as +45° to the Y-axis. Material properties used in our simulations are as listed in Table 10.
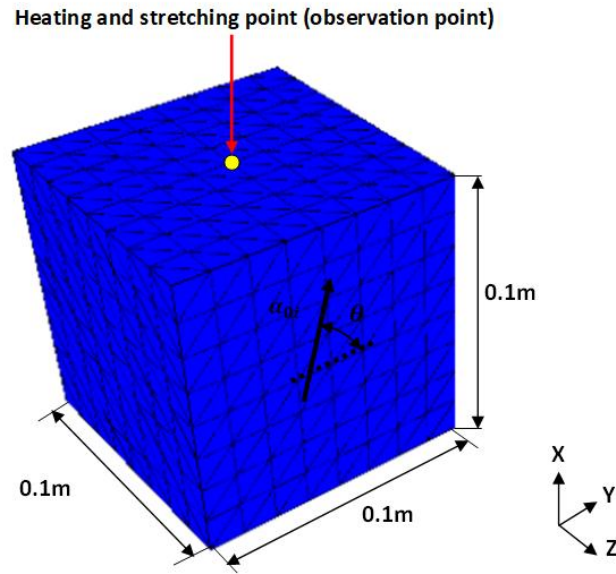
Figure 64: Heating, stretching and observation points position

Table 10: Tissue parameters and constants

Parameters	Value
Thermal conductivity k; W/mK	0.613
Specific heat C; J/kgK	4192
Thermal expansion coefficient α; 1/°C	3×10^{-4}
Density ρ; kg/m^3	1000
Shear modulus μ; Pa	1006
Poisson's ratio v;	0.35
Material constant K$_1$: Pa	2363.2
Material constant K$_2$:	0.8393
Blood perfusion rate ω_b; kg/(m^{3}s)	0.5
Arterial temperature T_b; K	310
Metabolic heat generation rate Q_m; W/m^3	33800
Blood specific heat C_b; J/kgK	3600
Characteristic Time τ_p; s	0.1

7.5.3 Time step setting

For stability reasons using explicit time scheme, rather small time step should be chosen for doing our simulation. Considering there is still no sound theory assisting

stability analysis for nonlinear differential equations, the well developed stability analysis for linear differential equations are applied here to select proper time step.

In the thermal solution of bioheat transfer equations, it is given by [141],

$$\Delta t_{crit} \leq min\left(\frac{\rho C L^2}{2k}\right)$$

where k is thermal conductivity, ρ is density, and specific heat c, L the shortest distance between any two connected finite element mesh nodes.

In mechanical solution, to estimate critical time step, the Courant Friedrichs Lewy [102] condition is applied as: $\Delta t_{crit} \leq min(L/c)$, with c being the speed of sound through the medium of interest given by,

$$c = \sqrt{\frac{\lambda + 2\mu}{\rho}}$$

where, λ and μ are constant lame parameters of target tissue materials.

Substituting listed parameters in Table 10 into Eq. 7-53 and Eq. 7-54 for critical time step calculation, we have,

$$\Delta t_{crit} \leq 0.00598 \text{ s}$$

With a great deal of adjustment to reach a stable simulation, finally the time step: 0.001s is chosen for a minimum mesh length of 0.0125m as used in our simulation tests, and the entire simulation time is set to 0.1s. Therefore, 100 iterations were

executed afterwards in order to obtain the steady state. Meanwhile, the damping coefficient ζ used in our simulations is set to 2500.

7.5.4 Purely mechanical loading problem

At the first stage of our simulation tests, only a constant tensile force of 0.325N is applied to the centre point in the normal direction of the top plane (see Figure 64), to identify its performance through comparison with other two commonly used models: linear elastic model and isotropic Neo-Hookean model (denoted as NH in plots). An observation point (see Figure 64) is also chosen to display its displacement, strain (Green-Lagrange strain), and stress (second Piola-Kirchhoff stress) variations.

Figure 65 plots the relationship of stress and strain which illustrates that, the anisotropic model is stiffer than the linear model, while the linear model is stiffer than the isotropic model during the initial range of deformation with strain < 0.08. Figure 66 to Figure 68 describe the components (displacement, strain, and stress) changes with time, which all increase gradually to a steady state value within simulation time range. Based on the illustration in Figure 69, it is observed that linear, anisotropic NH and isotropic NH models reach the balance state successively. Such an order is also consistent with displacement and strain versus time curves as shown in Figure 66 and Figure 67. To explain this, firstly we focus on two selected modes: isotropic NH with anisotropic NH. From Figure 69, it is illustrated that internal force for anisotropic NH curve is always larger than isotropic NH. Consequently, smaller values of displacement and strain should be determined before reaching steady state, just as displayed in Figure 66 and Figure 67. Similar process can be used to explain the relationship of any two models from Figure 66 to Figure 69. Besides, Figure 68 also gives the corresponding stress changes at this observation point. To display the final

130

displacement of three compared models, the deformations of the top plane at the end of simulation time are also displayed as shown in Figure 70 to Figure 72, where the peak values at selected top plane decrease in the order of: isotropic NH, anisotropic NH and linear models.
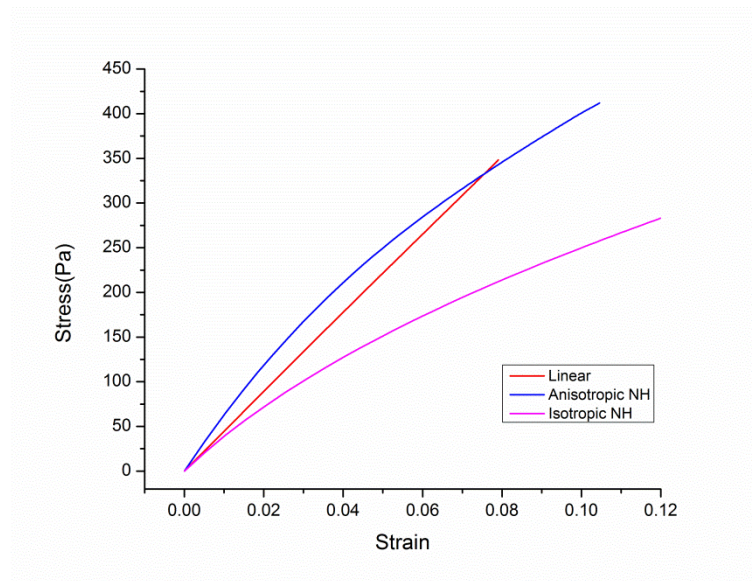
Figure 65: Strain stress relationship

Figure 66: Displacement vs. time at the observation point under mechanical loads only

Figure 67: Strain vs. time at the observation point under mechanical loads only
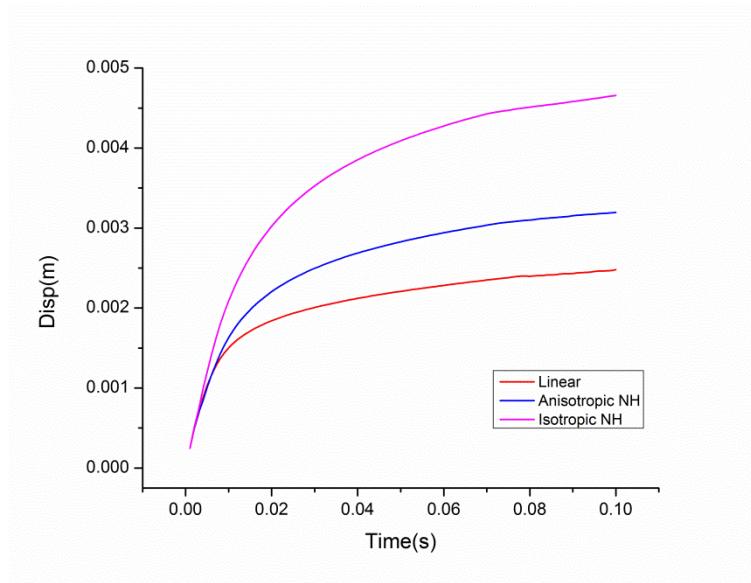
Figure 68: Stress vs. time at the observation point under mechanical loads only
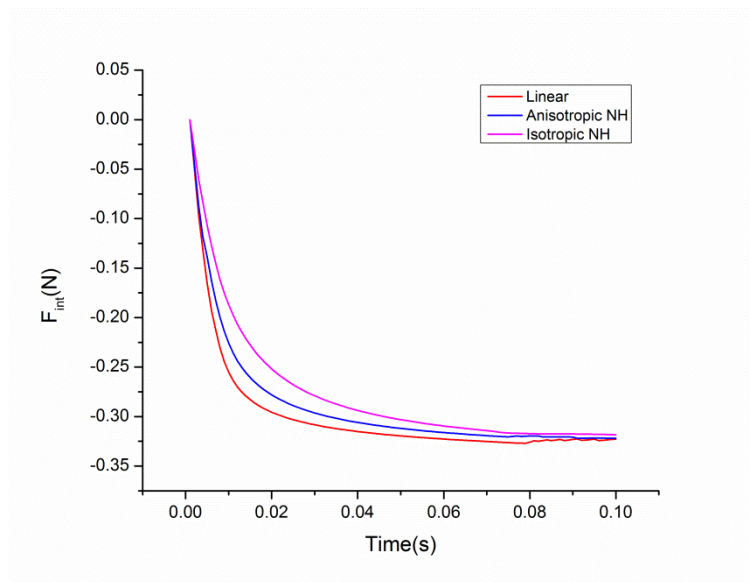
Figure 69: Internal force in x axis at the observation point under mechanical loads only
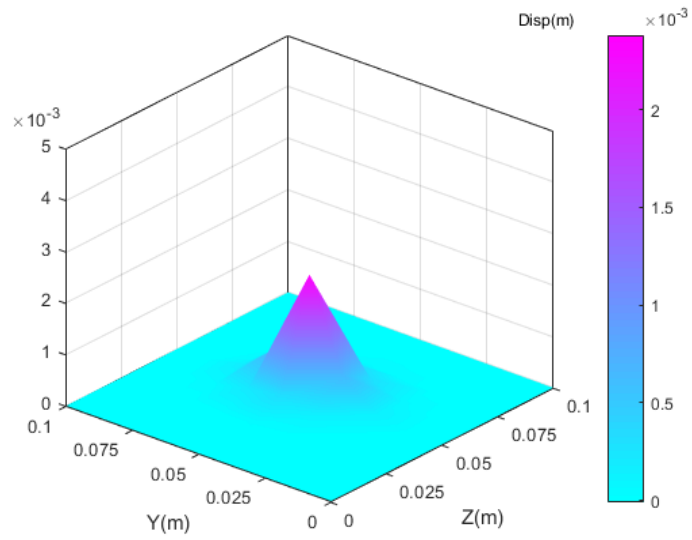
Figure 70: Deformation of plane x=0.1m for linear model under mechanical loads only
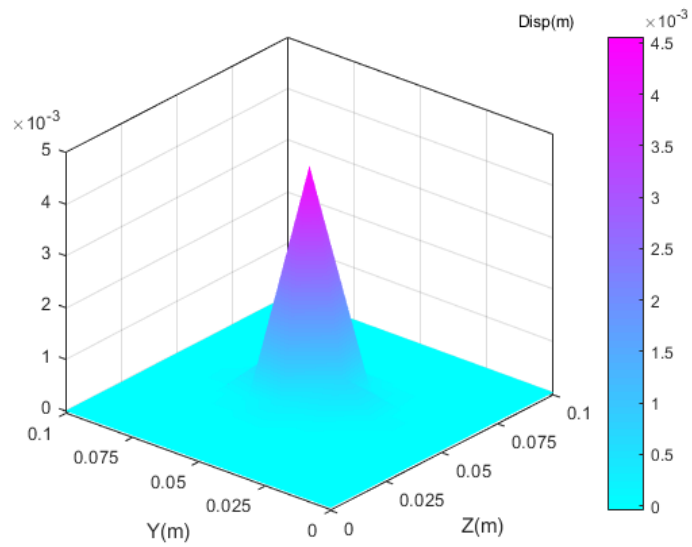
Figure 71: Deformation of plane x=0.1m for isotropic NH model under mechanical loads only
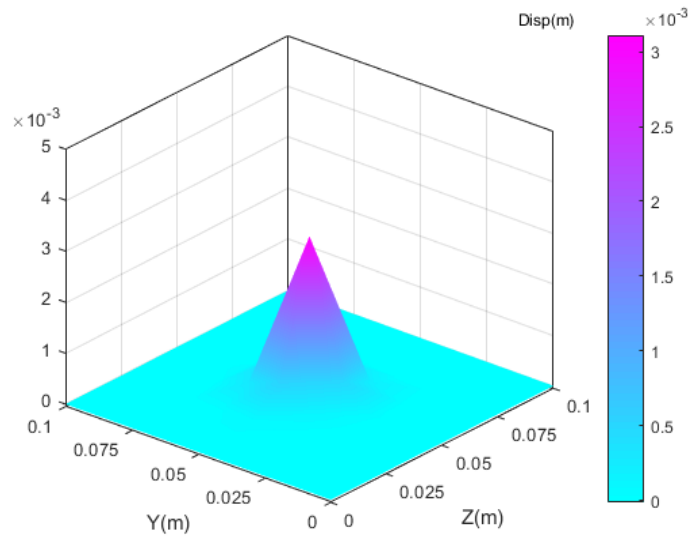
Figure 72: Deformation of plane x=0.1m for anisotropic NH model under mechanical loads only

7.5.5 Purely thermal loading problem

In order to identify the Fourier and non-Fourier effect in established nonlinear thermal mechanical model, a purely thermal loading simulation condition is designed, as: a point heating source targets at the centre of the top plane in Figure 64 would heat up the tissue model at power of $1.7X10^4$ W for a duration of 0.005s, and the total simulation time is set to be 0.1s.

For both Fourier and non-Fourier based nonlinear thermal mechanical models, corresponding distributions of temperature at the top plane are illustrated in Figure 73, where a peak value is observed at the heating point, but obviously Fourier based model gives a much higher temperature prediction than non-Fourier based model. Combing with the temperature vs. time curves in Figure 74, it is observed that a suddenly temperature rise is possible for Fourier based model, but for non-Fourier based model, a delayed and gradually rising temperature is predicted. Comparing with plots from

Figure 66 to Figure 68 under purely mechanical load, the displacement and strain curves under purely thermal load (see Figure 75 to Figure 76) all grow gradually with heating time but having relatively smaller magnitudes than under purely mechanical loading, while the stress at the same observation point is in a negative value under purely thermal load. For Fourier based model, it reaches a peak negative value of -21.47 Pa and decreases gradually to a stable value of -18.82 Pa, while for non-Fourier based model, a peak value of -7.14 Pa is approached gradually until the end of simulation time, see Figure 77. To explain the suddenly rising of stress for Fourier based model, we can refer to the temperature vs. time curve in Figure 74, where a suddenly rising of temperature is observed because of applied large amount of energy during this short period. However, due to the considered non-Fourier feature of soft tissue, such an increase of temperature at one point is not transferred infinitely through the entire tissue body immediately. Therefore, relatively lower temperature is obtained for non-Fourier model, as well as related strain and stress, as shown in Figure 76 and Figure 77.
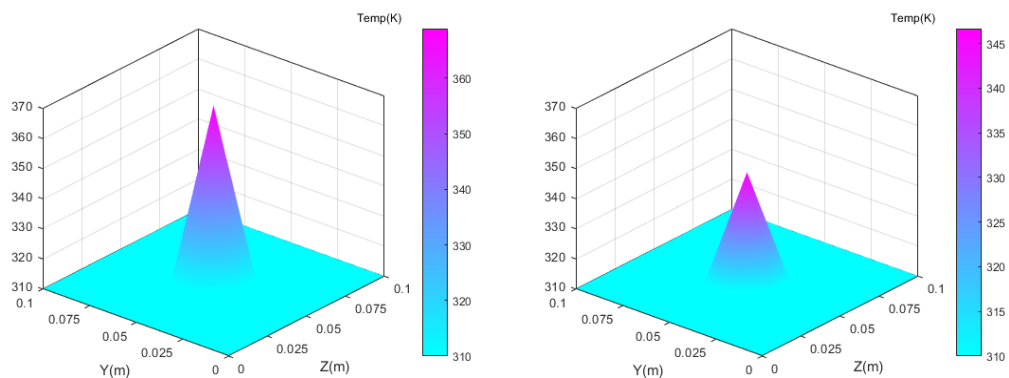
Figure 73: Temperature distribution at plane x=0.1 under thermal loads only: Fourier(left), Non-Fourier(right)
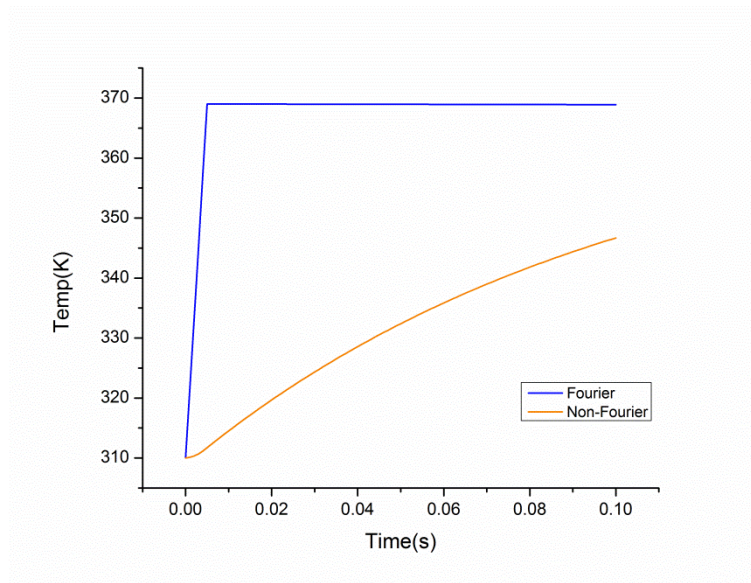
Figure 74: Temperature vs. time at the observation point under thermal loads only
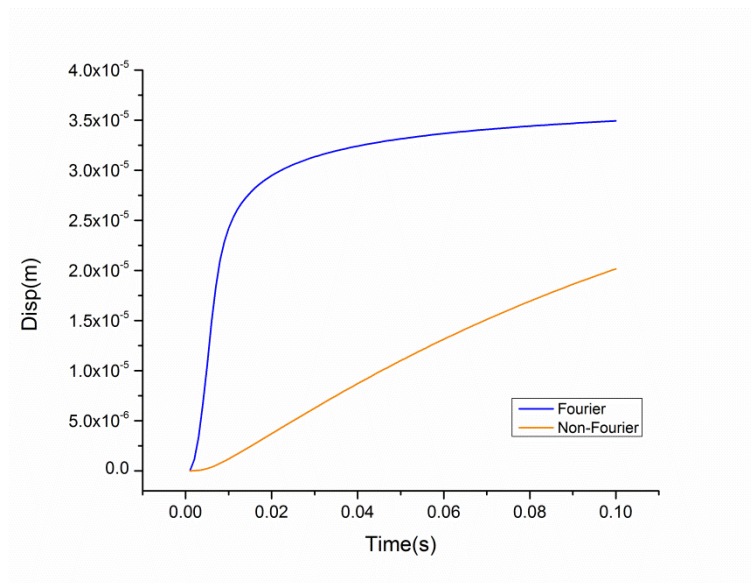
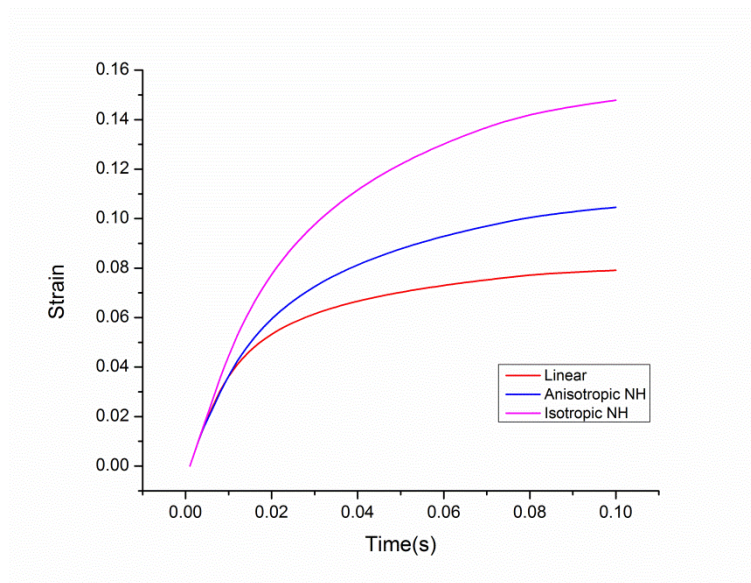Figure 75: Displacement vs. time at the observation point under thermal loads only
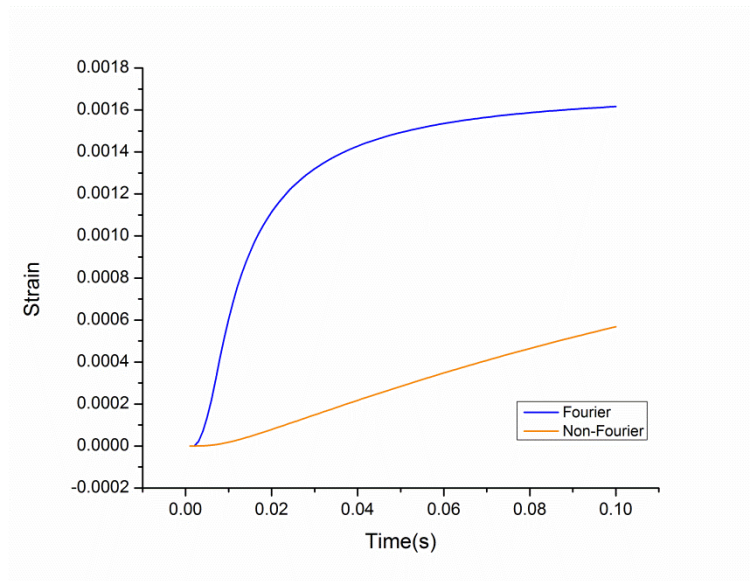
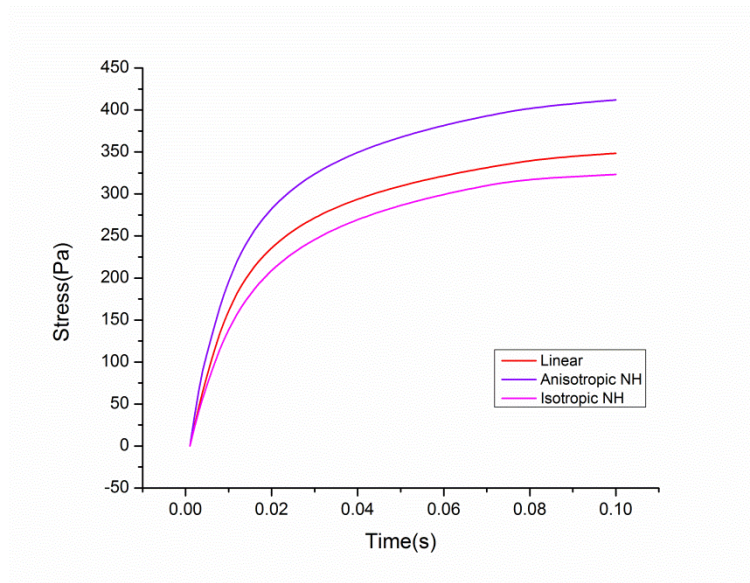Figure 76: Strain vs. time at the observation point under thermal loads only
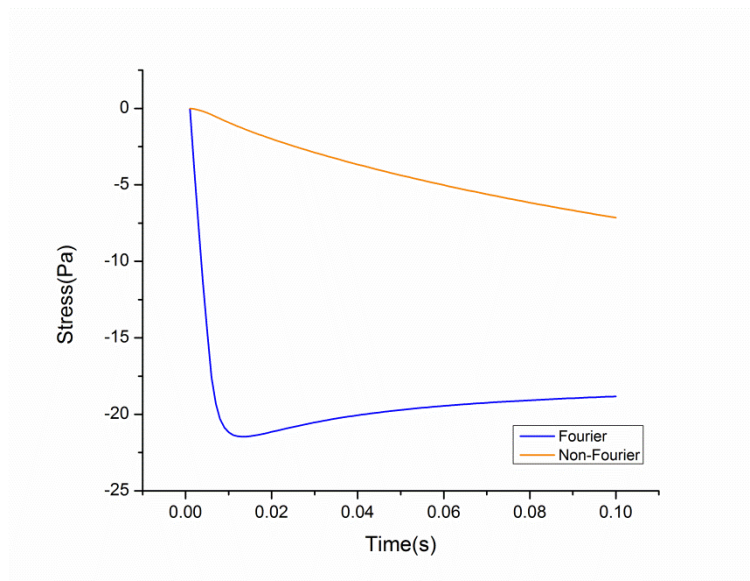
Figure 77: Stress vs. time at the observation point under thermal loads only

7.5.6 Combined thermal and mechanical loading problem

We performed another simulation test under combined thermal and mechanical loads condition using our proposed model based on both Fourier and non-Fourier bioheat

138

transfer theories. For simulation condition: a point heating source targets at the centre of the top plane in Figure 64 would heat up the tissue model at power of $1.7X10^4$ W for a duration of 0.005s, and the total simulation time is set to be 0.1s. At the same time, a constant tensile force of 0.325N is also applied to this centre point for the entire simulation period. Still, the point with applied thermal and mechanical loads is treated as the observation point to study the displacement, strain and stress variations. The simulation results are also compared with only mechanical problem as performed before. As shown in Figure 78 to Figure 80, it demonstrates that the difference of thermal-induced displacement is relatively small, but there is an obvious strain and stress contribution from thermal load. In detail, the strain deviation between only mechanical loading case and full problem case with combined thermal and mechanical loading starts to increase after 0.04s, leading to the maximum deviation of 0.0065 (see Figure 78), while the stress deviation starts to increase after 0.015s and 0.03s for Fourier and non-Fourier based full problem models, respectively (see Figure 79 and Figure 80). Towards the end of simulation, the stress for only mechanical load problem, full problem based on non-Fourier theory and Fourier theory reach: 373.52 Pa, 385.69 Pa and 412.01 Pa, respectively. This means that with the additional thermal load, the soft tissue becomes softer comparing to the case with the mechanical load only. Further, it can also be treated as another explanation for tissue stress-strain relationship shift at rising temperature caused by thermal load. As illustrated in another plot Figure 81, such a shift is even more obvious for Fourier based model considering it predicts greater temperature increase than non-Fourier based model along the simulation period. Excepting temperature dependent material mechanical properties, it can be used as additional theoretical basis to understand tissue's mechanical response under combined thermal and mechanical loads.
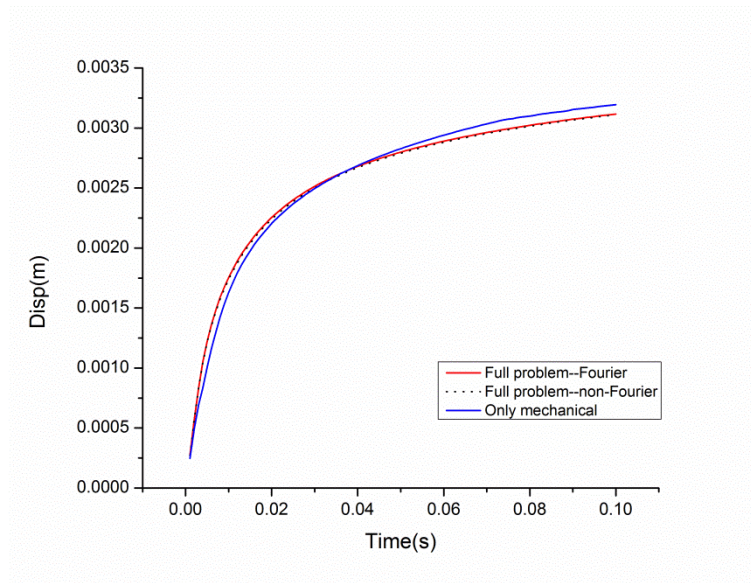
Figure 78: Comparison of displacement at the observation point
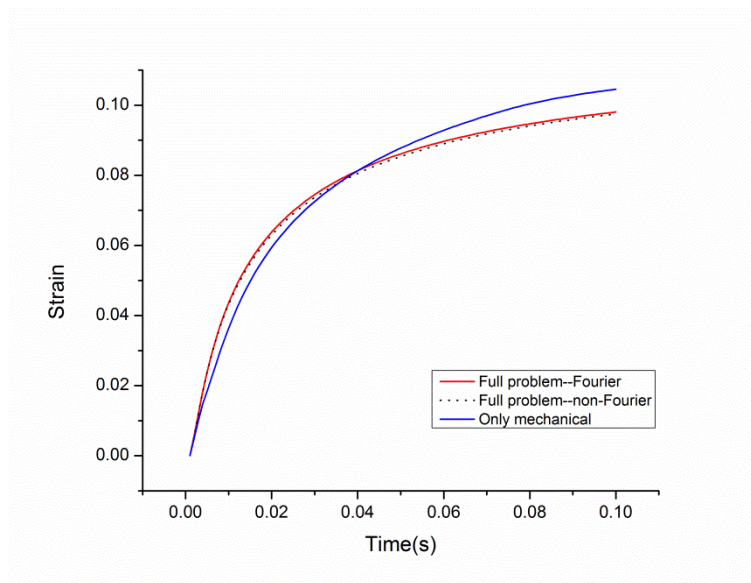
Figure 79: Comparison of strain at the observation point
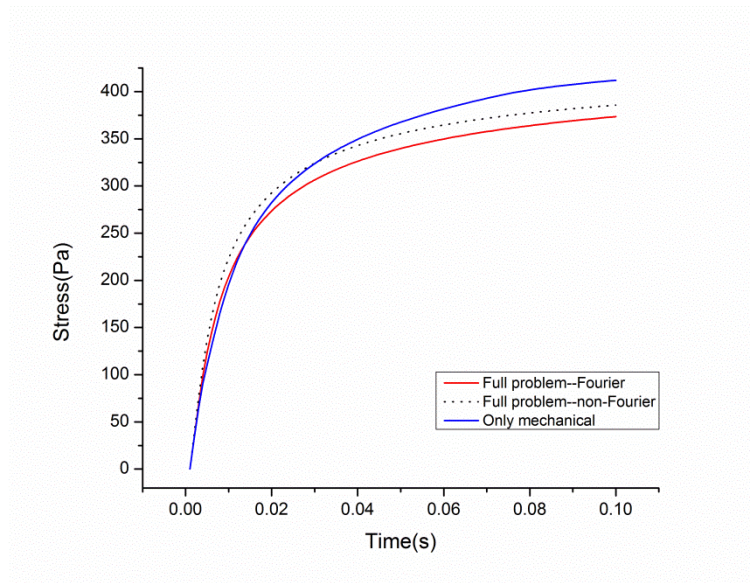
Figure 80: Comparison of stress at the observation point
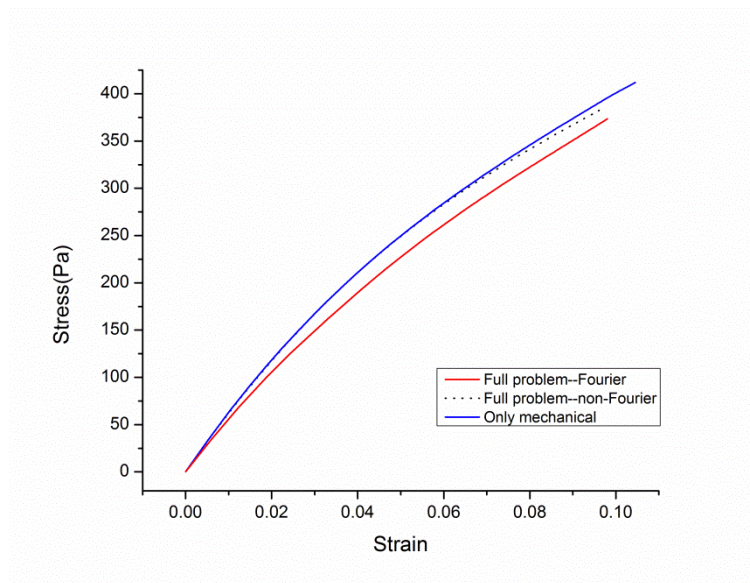
Figure 81: Stress strain relation at combined thermal mechanical loads

Further, the thermal mechanical damage profile at the top plane where thermal and mechanical loads applied on is also plotted. As illustrated in Figure 82 at the end of simulation time: 0.1s, using Fourier based nonlinear thermal mechanical model clearly

predicts a much larger value of damage than non-Fourier based model. Such a profile is also consistent with temperature distribution as illustrated in Figure 73. Meanwhile, the deviation of using traditional thermal damage prediction model and proposed thermal mechanical damage model at the observation point is also plotted against strain, considering strain or energy stored by corresponding tissue deformation is the only reason for deviation of predicted tissue damage. As illustrated in Figure 83 and Figure 84, it can be seen that under finite deformation, the influence of mechanical deformation on tissue damage prediction is becoming more obvious comparing to deformation limited to linear range of stress-strain relationship assumption. To further explain the different shapes of curves as shown in an enlarged view of Figure 83 and Figure 84, we can refer to the corresponding temperature at the same value of strain (see Figure 74 and Figure 76). Obviously, curve of Fourier based model has higher temperature prediction at the same value of caused strain, therefore, the influence of tissue deformation on thermal mechanical damage prediction is more strongly for Fourier based model than non-Fourier based model, just as shown in Figure 83 and Figure 84.
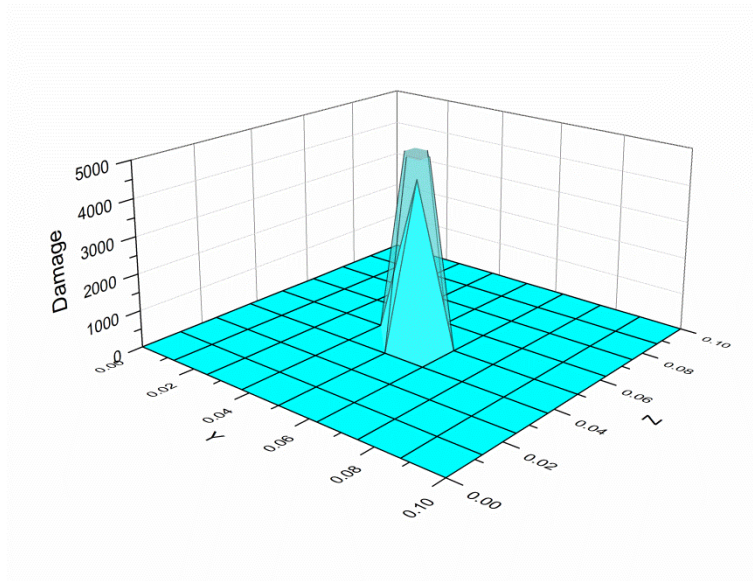
Figure 82: Damage distribution comparison for different thermal models
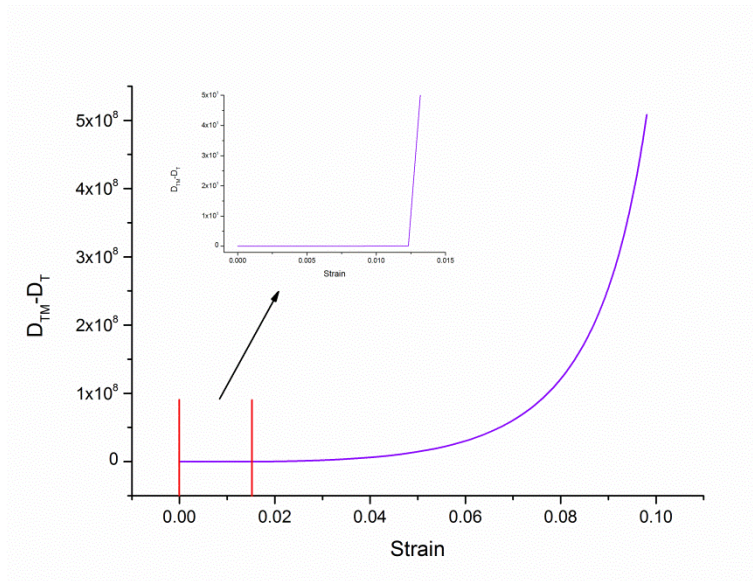
Figure 83: Damage prediction vs. time for Fourier based model
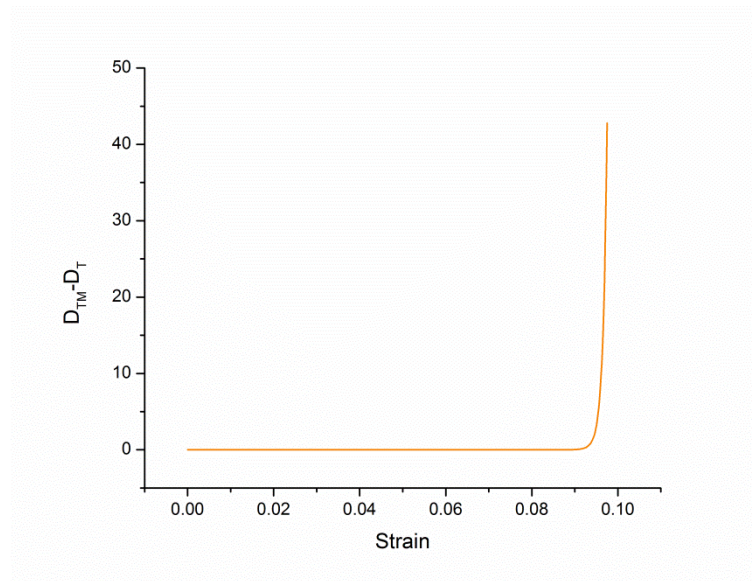
Figure 84: Damage prediction vs. time for non-Fourier based model

7.6 Conclusion

In practical application of thermal therapy, even small movement of operation tool/device for delivering heat can generate strain out of linear limit. To account for such influence, our research moved on to nonlinear range characterization of tissue response under combined thermal and mechanical loads. The established method combines both Fourier and non-Fourier bioheat transfer theories with Neo-Hookean free energy function to characterize the nonlinear thermomechanical behaviours of soft tissues. Further, the traditional Neo-Hookean free energy function is modified with an anisotropic term that defines the stored energy of embedded collagen fibre bundles in considered tissue materials. The necessary ingredients for the finite element implementation including: weak form and total Lagrangian formulations are also included in this chapter. In the implementation part, firstly the basic comparison between proposed model with traditional linear elastic model and isotropic Neo-

Hookean model is performed to identify its behaviours under purely mechanical load. And then in a purely thermal loading simulation test, it is observed that a suddenly temperature rise is possible for Fourier based model, but for non-Fourier based model, a delayed and gradually rising temperature is predicted inside treated tissue. Under combined thermal and mechanical loads, simulation results based upon our established model demonstrate that in spite of relatively small thermally induced displacement, there is an obvious strain and stress contribution due to additional thermal load, which makes soft tissues softer than the case with mechanical load only. Moving to tissue damage prediction under finite deformation, the influence of mechanical deformation is becoming more obvious comparing with deformation within linear range of stress-strain relationship assumption. Meanwhile, such an influence of tissue deformation on tissue damage prediction is more strongly for Fourier based model than non-Fourier based model, if the amount of thermal energy delivered into target soft tissue is relatively large and is applied within a short period. Furthermore, all these findings can be used as the theoretical basis for understanding and measuring tissue pain during practical thermal ablation applications.

8 Conclusions and future work

8.1 Conclusions

Based on the formulation of constitutive theory in the thermodynamic framework using multiplicative decomposition of thermal mechanical deformation gradient, our established thermal mechanical models are capable of being incorporated with temperature independent or temperature dependent material properties that obtained from physical experiments. In summary, this thesis has made the following contributions:

- Both Fourier and non-Fourier nature of soft tissues have been considered in our established thermal mechanical models. Depending the heating pattern that is applied or the simulation duration that is analysed, the Fourier and non-Fourier based thermal mechanical models have remarkable prediction deviation for both temperature and deformation fields.

- In order to account for both regular and irregular geometry soft tissue models, both FDM and FEM numerical methods have been used to build our computation programs, including a condensation method being applied to improve computation speed. Comparison between these two methods has also been conducted from the prospective of simulation accuracy and computing efficiency.

- Simulations have been performed based on an extended Arrhenius damage prediction model that takes consideration of temperature variation, both thermally and mechanically induced deformation influences during thermal ablation. It demonstrates that the presented prediction method can account for

146

tissue thermal damage more efficiently. Depending on the tissue parameters used, such a deviation against traditional thermal damage model can be remarkable, which may provide more reliable guidelines for controlling of the damage zone during thermal ablation procedure.

- By applying finite strain framework to anisotropic Neo-Hookean energy function and extending it to the heating process of soft tissue, another possible situation during thermal ablation is also considered. Under this circumstance, simulation results based upon our established model demonstrate that in spite of relatively small thermally induced displacement, there is an obvious strain and stress contribution due to additional thermal load, which makes soft tissues softer comparing to the case with mechanical load only.

- For validations, simulation results of Fourier based thermal mechanical models using numerical methods FDM and FEM have been compared. FEM based model is also validated against commercialised software tool LISA in temperature and deformation field, and validated against experimental data in temperature field. Furthermore, the nonlinear thermal mechanical model has also been validated against experimental data in deformation field.

8.2 Future work

The following gives some possible directions of improving our established thermal mechanical models based on our current research:

- Temperature dependent material properties can be considered into established thermal mechanical models to further analyse tissue's responses under thermal and mechanical loads during thermal ablation, as discussed in Chapter 2.

147

Specifically, plenty of research efforts have been dedicated in the area of temperature dependent thermal parameters [42, 96, 142, 143]. On the contrary, relatively few works are attempted in the area of temperature dependent mechanical parameters, considering the additional influence of temperature on thermal mechanical behaviour of soft tissues. Several scholars [89, 144, 145] have experimentally found a stress softening behaviour of soft tissues with rising temperature. However, they did not discuss the effect of temperature variation, and never revealed the micromechanisms related to the test results. Since the change in temperature may possibly cause denaturation and/or degradation of collagen molecules [90], it is essential to make further studies to incorporate thermal denaturation kinetics to capture the temperature dependent soft tissue responses.

- In order to speed up simulation process and realize real time simulation, the introduction of the Graphics Processing Unit (GPU) provided a means for massive data-parallel computation on the PC. Among these studies, Comas et al. [146] demonstrate a degree of simulation speeding of over 50 times in favour of GPU over a similar CPU (Central Processing Unit) implementation. Hills [97] has accelerated the simulation of bioheat transfer during radiofrequency ablation to a real time manner by GPU. Liu et al. [147] have developed a very general solution based on GPU with CUDA and demonstrated some excellent performance gains. But the implementation has not yet been used for simulation of thermal ablation process under combined thermal and mechanical loads for real-time visual feedback. Giving the improved performance speed mentioned above, it may allow an increase in maximum

possible mesh resolution for real-time thermal ablation simulation under thermal and mechanical loads as illustrated in our research.

References

[1] Y.-C. Fung, *Biomechanics Mechanical Properties of Living Tissues*, 1993.

[2] G. A. Holzapfel, "Biomechanics of soft tissue," *The handbook of materials behavior models,* vol. 3, pp. 1049-1063, 2001.

[3] F. Xu and T. Lu, *Introduction to skin biothermomechanics and thermal pain*: Springer, 2011.

[4] B. Zhou, F. Xu, C. Q. Chen, and T. J. Lu, "Strain rate sensitivity of skin tissue under thermomechanical loading," *Philosophical Transactions of the Royal Society a-Mathematical Physical and Engineering Sciences,* vol. 368, pp. 679-690, Feb 13 2010.

[5] F. Xu, T. Lu, K. Seffen, and E. Ng, "Mathematical modeling of skin bioheat transfer," *Applied Mechanics Reviews,* vol. 62, p. 050801, 2009.

[6] W. S. Shen and J. Zhang, "Modeling and numerical simulation of bioheat transfer and biomechanics in soft tissue," *Mathematical and Computer Modelling,* vol. 41, pp. 1251-1265, May 2005.

[7] W. S. Shen, J. Zhang, and F. Q. Yang, "Skin thermal injury prediction with strain energy," *International Journal of Nonlinear Sciences and Numerical Simulation,* vol. 6, pp. 317-328, 2005.

[8] J. Jimenez-Lozano, P. Vacas-Jacques, and W. Franco, "Thermo-elastic response of cutaneous and subcutaneous tissues to noninvasive radiofrequency heating," in *Proceedings of the 2012 COMSOL Conference in Boston (ISBN: 978-0-9839688-9-4)*, 2012.

[9] R. Stojanovic, S. Djuric, and L. Vujoševic, "On finite thermal deformations," *Arch. Mech. Stosow,* vol. 16, pp. 103-108, 1964.

[10] G. Holzapfel, "Nonlinear solid mechanics: a continuum approach for engineering, 2nd edn Chichester," *UK: John Wiley & Sons,* 2001.

[11] I. S. Sokolnikoff, *Mathematical theory of elasticity*: McGraw-Hill Book Company, 1956.

[12] X. Li, Y. Zhong, R. Jazar, and A. Subic, "Thermal-mechanical deformation modelling of soft tissues for thermal ablation," *Bio-medical materials and engineering,* vol. 24, pp. 2299-2310, 2014.

[13]   W. Dai, "Skin Burn Injury Prediction," in *Encyclopedia of Thermal Stresses*, ed: Springer, 2014, pp. 4421-4427.

[14]   J. C. BISCHOF and X. HE, "Thermal stability of proteins," *Annals of the New York Academy of Sciences,* vol. 1066, pp. 12-33, 2006.

[15]   R. Rounsevell, J. R. Forman, and J. Clarke, "Atomic force microscopy: mechanical unfolding of proteins," *Methods,* vol. 34, pp. 100-111, 2004.

[16]   J. A. Palero, M. Jurna, B. Varghese, and M. R. Horton, "Skin treatment device providing optical coupling to skin tissue," ed: Google Patents, 2014.

[17]   A. McBride, S. Bargmann, D. Pond, and G. Limbert, "Thermoelastic modelling of the skin at finite deformations," *Journal of Thermal Biology,* 2016.

[18]   T. C. Gasser, R. W. Ogden, and G. A. Holzapfel, "Hyperelastic modelling of arterial layers with distributed collagen fibre orientations," *Journal of the royal society interface,* vol. 3, pp. 15-35, 2006.

[19]   P. Prakash, "Theoretical modeling for hepatic microwave ablation," *The open Biomedical engineering journal,* vol. 4, p. 27, 2010.

[20]   I. A. Chang and U. D. Nguyen, "Thermal modeling of lesion growth with radiofrequency ablation devices," *Biomedical engineering online,* vol. 3, p. 27, 2004.

[21]   J. A. López-Molina, M. J. Rivera, M. Trujillo, F. Burdío, J. L. Lequerica, F. Hornero*, et al.*, "Assessment of hyperbolic heat transfer equation in theoretical modeling for radiofrequency heating techniques," *The open Biomedical engineering journal,* vol. 2, p. 22, 2008.

[22]   K.-C. Liu and C.-N. Lin, "Temperature prediction for tumor hyperthermia with the behavior of thermal wave," *Numerical Heat Transfer, Part A: Applications,* vol. 58, pp. 819-833, 2010.

[23]   A. Banerjee, A. A. Ogale, C. Das, K. Mitra, and C. Subramanian, "Temperature distribution in different materials due to short pulse laser irradiation," *Heat Transfer Engineering,* vol. 26, pp. 41-49, 2005.

[24]   F. Xu, K. Seffen, and T. Lu, "Non-Fourier analysis of skin biothermomechanics," *International Journal of Heat and Mass Transfer,* vol. 51, pp. 2237-2259, 2008.

[25]   H. Herwig and K. Beckert, "Experimental evidence about the controversy concerning Fourier or non-Fourier heat conduction in materials with a nonhomogeneous inner structureExperimentelle Befunde zur Kontroverse um das

Fouriersche oder nicht-Fouriersche Wärmeleitungsverhalten von Material mit inhomogener Struktur," *Heat and Mass Transfer,* vol. 36, pp. 387-392, 2000.

[26]   B. Zhang, M. Moser, E. Zhang, and W. J. Zhang, "Radiofrequency ablation technique in the treatment of liver tumours: review and future issues," *J Med Eng Technol,* vol. 37, pp. 150-9, Feb 2013.

[27]   G. S. Edwards, "Mechanisms for soft-tissue ablation and the development of alternative medical lasers based on investigations with mid-infrared free-electron lasers," *Laser & Photonics Reviews,* vol. 3, pp. 545-555, 2009.

[28]   P. Prakash, "Theoretical modeling for hepatic microwave ablation," *Open Biomed Eng J,* vol. 4, pp. 27-38, 2010.

[29]   B. J. O'Daly, E. Morris, G. P. Gavin, J. M. O'Byrne, and G. B. McGuinness, "High-power low-frequency ultrasound: A review of tissue dissection and ablation in medicine and surgery," *Journal of materials processing technology,* vol. 200, pp. 38-58, 2008.

[30]   J. Ding, X. Jing, J. Liu, Y. Wang, F. Wang, Y. Wang*, et al.*, "Complications of thermal ablation of hepatic tumours: comparison of radiofrequency and microwave ablative techniques," *Clinical radiology,* vol. 68, pp. 608-615, 2013.

[31]   K. F. Chu and D. E. Dupuy, "Thermal ablation of tumours: biological mechanisms and advances in therapy," *Nature Reviews Cancer,* vol. 14, pp. 199-208, 2014.

[32]   R. W. Habash, R. Bansal, D. Krewski, and H. T. Alhafid, "Thermal therapy, part 1: an introduction to thermal therapy," *Critical Reviews™ in Biomedical Engineering,* vol. 34, 2006.

[33]   M. G. Lubner, C. L. Brace, J. L. Hinshaw, and F. T. Lee Jr, "Microwave tumor ablation: mechanism of action, clinical results, and devices," *Journal of Vascular and Interventional Radiology,* vol. 21, pp. S192-S203, 2010.

[34]   C. L. Brace, "Radiofrequency and microwave ablation of the liver, lung, kidney, and bone: what are the differences?," *Current problems in diagnostic radiology,* vol. 38, pp. 135-143, 2009.

[35]   B. Zhang, M. Moser, E. Zhang, and W. Zhang, "Radiofrequency ablation technique in the treatment of liver tumours: review and future issues," *Journal of medical engineering & technology,* vol. 37, pp. 150-159, 2013.

[36]   J. P. McGahan, J. M. Brock, H. Tesluk, W.-Z. Gu, P. Schneider, and P. D. Browning, "Hepatic ablation with use of radio-frequency electrocautery in the animal model," *Journal of Vascular and Interventional Radiology,* vol. 3, pp. 291-297, 1992.

[37]   J. Ophir, I. Cespedes, B. Garra, H. Ponnekanti, Y. Huang, and N. Maklad, "Elastography: ultrasonic imaging of tissue strain and elastic modulus in vivo," *European journal of ultrasound,* vol. 3, pp. 49-70, 1996.

[38]   C. Pellot-Barakat, M. Sridhar, K. K. Lindfors, and M. F. Insana, "Ultrasonic elasticity imaging as a tool for breast cancer diagnosis and research," *Current Medical Imaging Reviews,* vol. 2, pp. 157-164, 2006.

[39]   H. Eskandari, S. E. Salcudean, R. Rohling, and J. Ohayon, "Viscoelastic characterization of soft tissue from dynamic finite element models," *Physics in medicine and biology,* vol. 53, p. 6569, 2008.

[40]   R. Sinkus, M. Tanter, S. Catheline, J. Lorenzen, C. Kuhl, E. Sondermann*, et al.*, "Imaging anisotropic and viscous properties of breast tissue by magnetic resonance-elastography," *Magnetic resonance in medicine,* vol. 53, pp. 372-387, 2005.

[41]   R. Sinkus, M. Tanter, T. Xydeas, S. Catheline, J. Bercoff, and M. Fink, "Viscoelastic shear properties of in vivo breast lesions measured by MR elastography," *Magnetic resonance imaging,* vol. 23, pp. 159-165, 2005.

[42]   S. R. Guntur, K. Il Lee, D.-G. Paeng, A. J. Coleman, and M. J. Choi, "TEMPERATURE-DEPENDENT THERMAL PROPERTIES OF EX VIVO LIVER UNDERGOING THERMAL ABLATION," *Ultrasound in Medicine and Biology,* vol. 39, pp. 1771-1784, Oct 2013.

[43]   H. Watanabe, Y. Kobayashi, M. Hashizume, and M. G. Fujie, "Modeling the temperature dependence of thermophysical properties: Study on the effect of temperature dependence for RFA," in *Engineering in Medicine and Biology Society, 2009. EMBC 2009. Annual International Conference of the IEEE*, 2009, pp. 5100-5105.

[44]   H. H. Pennes, "Analysis of tissue and arterial blood temperatures in the resting human forearm (Reprinted from Journal of Applied Physiology, vol 1, pg 93-122, 1948)," *Journal of Applied Physiology,* vol. 85, pp. 5-34, Jul 1998.

[45] W. Wulff, "The energy conservation equation for living tissue," *IEEE transactions on biomedical engineering,* pp. 494-495, 1974.

[46] M. M. Chen and K. R. Holmes, "Microvascular contributions in tissue heat transfer," *Annals of the New York Academy of Sciences,* vol. 335, pp. 137-150, 1980.

[47] J. W. Mitchell and G. E. Myers, "An analytical model of the counter-current heat exchange phenomena," *Biophysical journal,* vol. 8, pp. 897-911, 1968.

[48] S. Weinbaum, L. Jiji, and D. Lemons, "Theory and experiment for the effect of vascular microstructure on surface tissue heat transfer—Part I: Anatomical foundation and model conceptualization," *Journal of biomechanical engineering,* vol. 106, pp. 321-330, 1984.

[49] D. Lemons, "Theory and Experiment for the Effect of Vascular iicrostructure on Surface Tissue Heat Transfer—Part II: Model Formulation and Solution," *Journal of biomechanical engineering,* vol. 106, p. 331, 1984.

[50] K. Mitra, S. Kumar, A. Vedevarz, and M. Moallemi, "Experimental evidence of hyperbolic heat conduction in processed meat," *Journal of Heat Transfer,* vol. 117, pp. 568-573, 1995.

[51] M. F. Wakeni, "Stable algorithms for generalized thermoelasticity based on operator-splitting and time-discontinuous Galerkin finite element methods," University of Cape Town, 2016.

[52] G. Chen, "Ballistic-diffusive heat-conduction equations," *Physical Review Letters,* vol. 86, p. 2297, 2001.

[53] C. V. D. R. Anderson, *Thermal heat transport characterization for macroscale, microscale, and nanoscale heat conduction*: University of Minnesota, 2008.

[54] I. Dos Santos, D. Haemmerich, D. Schutt, A. F. da Rocha, and L. R. Menezes, "Probabilistic finite element analysis of radiofrequency liver ablation using the unscented transform," *Physics in medicine and biology,* vol. 54, p. 627, 2009.

[55] D. Haemmerich and D. J. Schutt, "RF ablation at low frequencies for targeted tumor heating: In vitro and computational modeling results," *Biomedical Engineering, IEEE Transactions on,* vol. 58, pp. 404-410, 2011.

[56] G. Zorbas and T. Samaras, "Parametric study of radiofrequency ablation in the clinical practice with the use of two-compartment numerical models," *Electromagnetic biology and medicine,* vol. 32, pp. 236-243, 2013.

[57]   F. Henriques Jr and A. Moritz, "Studies of thermal injury: I. The conduction of heat to and through skin and the temperatures attained therein. A theoretical and an experimental investigation*," *The American journal of pathology,* vol. 23, p. 530, 1947.

[58]   R. Agah, J. A. Pearce, A. J. Welch, and M. Motamedi, "Rate process model for arterial tissue thermal damage: Implications on vessel photocoagulation," *Lasers in surgery and medicine,* vol. 15, pp. 176-184, 1994.

[59]   W. Weinberg, R. Birngruber, and B. Lorenz, "The change in light reflection of the retina during therapeutic laser photocoagulation," *IEEE journal of quantum electronics,* vol. 20, pp. 1481-1489, 1984.

[60]   F. Henriques Jr, "Studies of thermal injury; the predictability and the significance of thermally induced rate processes leading to irreversible epidermal injury," *Archives of pathology,* vol. 43, pp. 489-502, 1947.

[61]   A. Roggan and G. Müller, "Computer simulations for the irradiation planning of LITT," *Med. Tech,* vol. 4, pp. 18-24, 1993.

[62]   R. Rivlin and D. Saunders, "Large elastic deformations of isotropic materials," in *Collected Papers of RS Rivlin*, ed: Springer, 1997, pp. 157-194.

[63]   M. Mooney, "A theory of large elastic deformation," *Journal of applied physics,* vol. 11, pp. 582-592, 1940.

[64]   R. Ogden, "Large deformation isotropic elasticity-on the correlation of theory and experiment for incompressible rubberlike solids," in *Proceedings of the Royal Society of London A: Mathematical, Physical and Engineering Sciences*, 1972, pp. 565-584.

[65]   O. Yeoh, "Some forms of the strain energy function for rubber," *Rubber Chemistry and technology,* vol. 66, pp. 754-771, 1993.

[66]   A. Gent, "A new constitutive relation for rubber," *Rubber chemistry and technology,* vol. 69, pp. 59-61, 1996.

[67]   L. Treloar, "The elasticity of a network of long-chain molecules. I," *Transactions of the Faraday Society,* vol. 39, pp. 36-41, 1943.

[68]   L. Treloar, "The elasticity of a network of long-chain molecules—II," *Transactions of the Faraday Society,* vol. 39, pp. 241-246, 1943.

[69]   L. Treloar, "The elasticity of a network of long-chain molecules.—III," *Transactions of the Faraday Society,* vol. 42, pp. 83-94, 1946.

[70] E. M. Arruda and M. C. Boyce, "A three-dimensional constitutive model for the large stretch behavior of rubber elastic materials," *Journal of the Mechanics and Physics of Solids,* vol. 41, pp. 389-412, 1993.

[71] J. Bergström and M. Boyce, "Constitutive modeling of the large strain time-dependent behavior of elastomers," *Journal of the Mechanics and Physics of Solids,* vol. 46, pp. 931-954, 1998.

[72] K. Garikipati, S. Göktepe, and C. Miehe, "Elastica-based strain energy functions for soft biological tissue," *Journal of the Mechanics and Physics of Solids,* vol. 56, pp. 1693-1713, 2008.

[73] P. H. Kao, S. R. Lammers, K. Hunter, K. R. Stenmark, R. Shandas, and H. J. Qi, "Constitutive modeling of anisotropic finite-deformation hyperelastic behaviors of soft materials reinforced by tortuous fibers," *The international journal of structural changes in solids: mechanics and applications,* vol. 2, p. 19, 2010.

[74] J. A. Weiss, B. N. Maker, and S. Govindjee, "Finite element implementation of incompressible, transversely isotropic hyperelasticity," *Computer methods in applied mechanics and engineering,* vol. 135, pp. 107-128, 1996.

[75] D. Balzani, P. Neff, J. Schröder, and G. A. Holzapfel, "A polyconvex framework for soft biological tissues. Adjustment to experimental data," *International journal of solids and structures,* vol. 43, pp. 6052-6070, 2006.

[76] J. Valvano, J. Cochran, and K. Diller, "Thermal conductivity and diffusivity of biomaterials measured with self-heated thermistors," *International Journal of Thermophysics,* vol. 6, pp. 301-311, 1985.

[77] G. Trezek and T. Cooper, "A probe technique for determining the thermal conductivity of tissue," *Journal of Heat Transfer,* vol. 94, pp. 133-140, 1972.

[78] H. Bowman, "Heat transfer and thermal dosimetry," *Journal of Microwave Power,* vol. 16, pp. 121-133, 1981.

[79] Z. Bu-Lin, H. Bing, K. Sheng-Li, Y. Huang, W. Rong, and L. Jia, "A polyacrylamide gel phantom for radiofrequency ablation," *International Journal of Hyperthermia,* vol. 24, pp. 568-576, 2008.

[80] A. Bhattacharya and R. Mahajan, "Temperature dependence of thermal conductivity of biological tissues," *Physiological measurement,* vol. 24, p. 769, 2003.

[81] D. Haemmerich, I. dos Santos, D. J. Schutt, J. G. Webster, and D. M. Mahvi, "In vitro measurements of temperature-dependent specific heat of liver tissue," *Medical engineering & physics,* vol. 28, pp. 194-197, 2006.

[82] J. F. M. Manschot, "The mechanical properties of human skin in vivo," [Sl: sn], 1985.

[83] W. Maurel, Y. Wu, D. Thalmann, and N. M. Thalmann, *Biomechanical models for soft tissue simulation* vol. 215: Springer, 1998.

[84] F. Xu, T. Wen, T. Lu, and K. Seffen, "Skin biothermomechanics for medical treatments," *Journal of the mechanical behavior of biomedical materials,* vol. 1, pp. 172-187, 2008.

[85] P. Keangin, T. Wessapan, and P. Rattanadecho, "Analysis of heat transfer in deformed liver cancer modeling treated using a microwave coaxial antenna," *Applied Thermal Engineering,* vol. 31, pp. 3243-3254, 2011.

[86] M. Hollenstein, A. Nava, D. Valtorta, J. Snedeker, and E. Mazza, "Mechanical characterization of the liver capsule and parenchyma," *Biomedical Simulation,* pp. 150-158, 2006.

[87] K. Miller, G. Joldes, D. Lance, and A. Wittek, "Total Lagrangian explicit dynamics finite element algorithm for computing soft tissue deformation," *Communications in numerical methods in engineering,* vol. 23, pp. 121-134, 2007.

[88] A. Choi and Y. Zheng, "Estimation of Young's modulus and Poisson's ratio of soft tissue from indentation using two different-sized indentors: finite element analysis of the finite deformation effect," *Medical and Biological Engineering and Computing,* vol. 43, pp. 258-264, 2005.

[89] M. Lin, X. Zhai, S. Wang, Z. Wang, F. Xu, and T. J. Lu, "Influences of supra-physiological temperatures on microstructure and mechanical properties of skin tissue," *Medical engineering & physics,* vol. 34, pp. 1149-1156, 2012.

[90] A. Mlyniec, K. Tomaszewski, E. Spiesz, and T. Uhl, "Molecular-based nonlinear viscoelastic chemomechanical model incorporating thermal denaturation kinetics of collagen fibrous biomaterials," *Polymer Degradation and Stability,* vol. 119, pp. 87-95, 2015.

[91] G. San-Vicente, I. Aguinaga, and J. T. Celigueta, "Cubical mass-spring model design based on a tensile deformation test and nonlinear material model,"

Visualization and Computer Graphics, IEEE Transactions on, vol. 18, pp. 228-241, 2012.

[92]   S. Natsupakpong and M. Cenk Çavuşoğlu, "Determination of elasticity parameters in lumped element (mass-spring) models of deformable objects," Graphical Models, vol. 72, pp. 61-73, 2010.

[93]   F. Chen, L. Gu, P. Huang, J. Zhang, and J. Xu, "Soft tissue modeling using nonlinear mass spring and simplified medial representation," IEEE engineering in medicine and biology magazine, vol. 1, p. 5083, 2007.

[94]   P. Prakash, V. A. Salgaonkar, S. J. Scott, P. Jones, D. Hensley, A. Holbrook, et al., "MR guided thermal therapy of pancreatic tumors with endoluminal, intraluminal and interstitial catheter-based ultrasound devices: preliminary theoretical and experimental investigations," in SPIE BiOS, 2013, pp. 85840V-85840V-10.

[95]   H. Watanabe, N. Yamazaki, Y. Kobayashi, T. Miyashita, T. Ohdaira, M. Hashizume, et al., "Estimation of Intraoperative Blood Flow during Liver RF Ablation Using a Finite Element Method-based Biomechanical Simulation," 2011 Annual International Conference of the Ieee Engineering in Medicine and Biology Society (Embc), pp. 7441-7445, 2011.

[96]   H. Watanabe, N. Yamazaki, Y. Isobe, X. W. Lu, Y. Kobayashi, T. Miyashita, et al., "Validation of Accuracy of Liver Model with Temperature-Dependent Thermal Conductivity by Comparing the Simulation and in vitro RF Ablation Experiment," 2012 Annual International Conference of the Ieee Engineering in Medicine and Biology Society (Embc), pp. 5712-5717, 2012.

[97]   J. Hills, "Real-time modelling and visualization of soft tissue thermomechanical behaviour for radiofrequency thermal ablation," 2015.

[98]   P. Rattanadecho and P. Keangin, "Numerical study of heat transfer and blood flow in two-layered porous liver tissue during microwave ablation process using single and double slot antenna," International Journal of Heat and Mass Transfer, vol. 58, pp. 457-470, 2013.

[99]   T. Wu, P. Li, Q. Shao, J. Hong, L. Yang, and S. Wu, "A Simulation-Experiment Method to Characterize the Heat Transfer in Ex-Vivo Porcine Hepatic Tissue with a Realistic Microwave Ablation System," Numerical Heat Transfer, Part A: Applications, vol. 64, pp. 729-743, 2013.

[100]   K. K. Tamma, "Nonclassical Thermomechanical Models: Numerical Formulations," *Encyclopedia of Thermal Stresses,* pp. 3307-3317, 2014.

[101]   X. Zhou, K. K. Tamma, and C. V. Anderson, "On a new C-and F-processes heat conduction constitutive model and the associated generalized theory of dynamic thermoelasticity," *Journal of Thermal Stresses,* vol. 24, pp. 531-564, 2001.

[102]   P. Majumdar, *Computational methods for heat and mass transfer*: CRC press, 2005.

[103]   M. Bro-Nielsen and S. Cotin, "Real-time Volumetric Deformable Models for Surgery Simulation using Finite Elements and Condensation," in *Computer graphics forum*, 1996, pp. 57-66.

[104]   N. Jamil, "A comparison of direct and indirect solvers for linear systems of equations," *International Journal of Emerging Sciences,* vol. 2, pp. 310-321, 2012.

[105]   Y. Saad, *Iterative methods for sparse linear systems*: SIAM, 2003.

[106]   C. Dick, J. Georgii, and R. Westermann, "A real-time multigrid finite hexahedra method for elasticity simulation using CUDA," *Simulation Modelling Practice and Theory,* vol. 19, pp. 801-816, 2011.

[107]   E. H. Lee, "Elastic-plastic deformation at finite strains," 1969.

[108]   V. Lubarda, "An analysis of large-strain damage elastoplasticity," *International journal of solids and structures,* vol. 31, pp. 2951-2964, 1994.

[109]   J. Clayton and D. McDowell, "A multiscale multiplicative decomposition for elastoplasticity of polycrystals," *International Journal of Plasticity,* vol. 19, pp. 1401-1444, 2003.

[110]   C. Truesdell and W. Noll, "The non-linear field theories of mechanics," in *The non-linear field theories of mechanics*, ed: Springer, 2004, pp. 1-579.

[111]   V. A. Lubarda, "Constitutive theories based on the multiplicative decomposition of deformation gradient: Thermoelasticity, elastoplasticity, and biomechanics," *Appl. Mech. Rev,* vol. 57, pp. 95-108, 2004.

[112]   L. Vujošević and V. Lubarda, "Finite-strain thermoelasticity based on multiplicative decomposition of deformation gradient," *Theoretical and applied mechanics,* pp. 379-399, 2002.

[113]   H. B. Callen, "Thermodynamics and an Introduction to Thermostatistics," ed: AAPT, 1998.

[114]   H. Delingette and N. Ayache, "Soft tissue modeling for surgery simulation," *Computational models for the human body,* pp. 453-550, 2004.

[115]   Z. Liu and L. Bilston, "On the viscoelastic character of liver tissue: experiments and modelling of the linear behaviour," *Biorheology,* vol. 37, pp. 191-201, 2000.

[116]   J. W. Mitchell, T. L. Galvez, J. Hengle, G. E. Myers, and K. L. Siebecker, "Thermal response of human legs during cooling," *Journal of Applied Physiology,* vol. 29, pp. 859-865, 1970.

[117]   P. K. Gupta, J. Singh, and K. Rai, "Numerical simulation for heat transfer in tissues during thermal therapy," *Journal of Thermal Biology,* vol. 35, pp. 295-301, 2010.

[118]   S. Karaa, J. Zhang, and F. Yang, "A numerical study of a 3D bioheat transfer problem with different spatial heating," *Mathematics and Computers in Simulation,* vol. 68, pp. 375-388, 2005.

[119]   C. P. LAU, Y. T. TAI, and P. W. Lee, "The Effects of Radiofrequency Ablation Versus Medical Therapy on the Quality-of-Life and Exercise Capacity in Patients with Accessory Pathway-Mediated Supraventricular Tachycardia: A Treatment Comparison Study," *Pacing and Clinical Electrophysiology,* vol. 18, pp. 424-432, 1995.

[120]   J. A. Pearce, "Comparative analysis of mathematical models of cell death and thermal damage processes," *International Journal of Hyperthermia,* vol. 29, pp. 262-280, 2013.

[121]   T. Stylianopoulos, A. Aksan, and V. H. Barocas, "A structural, kinetic model of soft tissue thermomechanics," *Biophysical journal,* vol. 94, pp. 717-725, 2008.

[122]   H. Arkin, L. X. Xu, and K. R. Holmes, "RECENT DEVELOPMENTS IN MODELING HEAT-TRANSFER IN BLOOD-PERFUSED TISSUES," *Ieee Transactions on Biomedical Engineering,* vol. 41, pp. 97-107, Feb 1994.

[123]   H. D. Weymann, "Finite speed of propagation in heat conduction, diffusion, and viscous shear motion," *American Journal of Physics,* vol. 35, pp. 488-496, 1967.

[124]   D. E. Hurtado, S. Castro, and A. Gizzi, "Computational modeling of non-linear diffusion in cardiac electrophysiology: A novel porous-medium approach," *Computer Methods in Applied Mechanics and Engineering,* vol. 300, pp. 70-83, 2016.

[125]   C. Cattaneo, "SUR UNE FORME DE LEQUATION DE LA CHALEUR ELIMINANT LE PARADOXE DUNE PROPAGATION INSTANTANEE," *Comptes Rendus Hebdomadaires Des Seances De L Academie Des Sciences,* vol. 247, pp. 431-433, 1958 1958.

[126]   P. Vernotte, "LES PARADOXES DE LA THEORIE CONTINUE DE LEQUATION DE LA CHALEUR," *Comptes Rendus Hebdomadaires Des Seances De L Academie Des Sciences,* vol. 246, pp. 3154-3155, 1958 1958.

[127]   J. Liu, Z. Ren, and C. Wang, "Thermal wave theory about temperature oscillations effect in living tissues," *Chin J Med Phys,* vol. 12, pp. 215-218, 1995.

[128]   W. Roetzel, N. Putra, and S. K. Das, "Experiment and analysis for non-Fourier conduction in materials with non-homogeneous inner structure," *International Journal of Thermal Sciences,* vol. 42, pp. 541-552, 2003.

[129]   R. B. Hetnarski and M. R. Eslami, *Thermal stresses: advanced theory and applications* vol. 41: Springer, 2009.

[130]   D. P. O'Neill, T. Peng, P. Stiegler, U. Mayrhauser, S. Koestenbauer, K. Tscheliessnigg*, et al.*, "A three-state mathematical model of hyperthermic cell death," *Annals of biomedical engineering,* vol. 39, pp. 570-579, 2011.

[131]   A. Andreano and C. L. Brace, "A comparison of direct heating during radiofrequency and microwave ablation in ex vivo liver," *Cardiovascular and interventional radiology,* vol. 36, pp. 505-511, 2013.

[132]   D. Yang, M. C. Converse, D. M. Mahvi, and J. G. Webster, "Measurement and analysis of tissue temperature during microwave liver ablation," *Biomedical Engineering, IEEE Transactions on,* vol. 54, pp. 150-155, 2007.

[133]   L. Zhu, L. X. Xu, and N. Chencinski, "Quantification of the 3-D electromagnetic power absorption rate in tissue during transurethral prostatic microwave thermotherapy using heat transfer model," *Biomedical Engineering, IEEE Transactions on,* vol. 45, pp. 1163-1172, 1998.

[134]   J. Xu, Z. z. Jia, Z. j. Song, X. d. Yang, K. Chen, and P. Liang, "Three-dimensional ultrasound image‑guided robotic system for accurate microwave coagulation of malignant liver tumours," *The International Journal of Medical Robotics and Computer Assisted Surgery,* vol. 6, pp. 256-268, 2010.

[135]   A. E. Ehret and M. Itskov, "A polyconvex hyperelastic model for fiber-reinforced materials in application to soft tissues," *Journal of Materials Science,* vol. 42, pp. 8853-8863, 2007.

[136]   G. Chagnon, M. Rebouah, and D. Favier, "Hyperelastic energy densities for soft biological tissues: a review," *Journal of Elasticity,* vol. 120, pp. 129-160, 2015.

[137]   D. Nolan, A. Gower, M. Destrade, R. Ogden, and J. McGarry, "A robust anisotropic hyperelastic formulation for the modelling of soft tissue," *Journal of the mechanical behavior of biomedical materials,* vol. 39, pp. 48-60, 2014.

[138]   C. Chui, E. Kobayashi, X. Chen, T. Hisada, and I. Sakuma, "Transversely isotropic properties of porcine liver tissue: experiments and constitutive modelling," *Medical & biological engineering & computing,* vol. 45, pp. 99-106, 2007.

[139]   B. Ghali, "Algorithms for nonlinear finite element-based modeling of soft-tissue deformation and cutting," 2008.

[140]   D. Nolan and J. McGarry, "On the compressibility of arterial tissue," *Annals of biomedical engineering,* vol. 44, pp. 993-1007, 2016.

[141]   R. W. Lewis, P. Nithiarasu, and K. N. Seetharamu, *Fundamentals of the finite element method for heat and fluid flow*: John Wiley & Sons, 2004.

[142]   H. Watanabe, Y. Kobayashi, M. Hashizume, and M. G. Fujie, "Modeling the temperature dependence of thermophysical properties: study on the effect of temperature dependence for RFA," in *31st Annual International Conference of the IEEE Engineering in Medicine and Biology Society: Engineering the Future of Biomedicine, EMBC 2009, September 2, 2009 - September 6, 2009,* Minneapolis, MN, United states, 2009, pp. 5100-5105.

[143]   Z. Ji and C. L. Brace, "Expanded modeling of temperature-dependent dielectric properties for microwave thermal ablation," *Physics in medicine and biology,* vol. 56, p. 5249, 2011.

[144]   L. Tao, P. B. Wells, J. D. Humphrey, and K. R. Rajagopal, "A model for the kinetics of thermal damage of biological membranes," *Note di Matematica,* vol. 27, pp. 229-247, 2007.

[145]   F. Xu and T. Lu, "Skin biothermomechanics: modeling and experimental characterization," *Advances in applied mechanics,* vol. 43, pp. 147-248, 2009.

[146]   O. Comas, Z. A. Taylor, J. Allard, S. Ourselin, S. Cotin, and J. Passenger, "Efficient nonlinear FEM for soft tissue modelling and its GPU implementation within the open source framework SOFA," in *International Symposium on Biomedical Simulation*, 2008, pp. 28-39.

[147]   Y. Liu, S. Jiao, W. Wu, and S. De, "GPU accelerated fast FEM deformation simulation," in *Circuits and Systems, 2008. APCCAS 2008. IEEE Asia Pacific Conference on*, 2008, pp. 606-609.